

Appendix-1

断層の動的破壊シミュレーションと
物理に基づく地震動シミュレーション

“Surface Rupture Simulations and Physics-based Ground Motion Simulations”

Summary

We have started to work with stochastic dynamic models. For this purpose, in this project we have compiled and evaluated the work done since 2012 by the research group of Dr. Dalguer of earthquake rupture and near-source ground motion generated from a database of stochastic dynamic rupture simulations for three classes of faulting (thrust, normal and strike slip) and for buried and surface-rupturing faults. This database of synthetic earthquake models has been developed since 2011 to date by Dr. Dalguer. The main database consists of 360 generic source models in which initial stress along the fault is characterized by stochastic field realizations based on von Karman distribution. Stress and frictional strength consider two extreme cases of normal stress, 1) depth-dependent, and 2) depth-independent. The simulations assemble a set of earthquakes with moment magnitudes in the range of 5.6–7. In addition, we have included in this database couple of stochastic rupture models with $M_w \sim 7.8$ parameterized on a fault with geometrical characteristics of the 1999 Chi-Chi Taiwan earthquake, as well as ruptures in strike slip faults exhibiting complexities of slip reactivation and super-shear rupture. This diversity of rupture models generates a broad range of scenarios for evaluating surface fault displacement and near-source ground motion variability. The peak ground displacement (PGD), peak ground velocity (PGV) and spectral accelerations (SA) are compared with empirical ground motion prediction equation (GMPEs). Overall, the synthetic ground motion are compatible with the empirical model data up to 1Hz, which means that the residuals (defined as the differences between observed and predicted ground motions) fall in the range of standard deviation of the empirical GMPE. This database reveals features of variability of super-shear rupture speed that depend on earthquake size; ground motion super-saturation near the source, which is different from the saturation features predicted by empirical GMPEs; prediction of acceleration exceeding $1g$ that are evaluated with appropriate recent near-field observations. We find that the effect of source parameters (such as stress drop, peak slip velocity, and rupture speed), surface and buried rupture, directivity as well as hanging wall and footwall are sensitive to ground motion, suggesting that these effects contribute to the variability of ground motion near the source. These findings provide insights on source dominated ground motion features that is not possible to evaluate from real data because of lack of observations. This work is expected to complement the investigation on asperity models developed during the last fiscal year and to generalize fault rupture models characteristics of future earthquakes for ground motion prediction. It is the initiation of a long-term research project. We want to continue building a database of suites of synthetic earthquakes compatible with past earthquakes (in statistical sense) for hazard and risk assessment of future earthquakes in areas where there are not enough observed data. We target to develop hybrid physics-based GMPEs using synthetic and observed data for engineering application of ground motion prediction. This is particularly of relevant importance near the source where recorded data are sparse and ground motions (displacement, velocity and acceleration) are dominated by the source effects, such as large permanent displacement, strong velocity pulses that impose extreme demands in structures.

In addition to the work described above, we have completed the work done the last fiscal year (2013), in which we have simulated the 1999 Chi-Chi earthquake with asperity models, by comparing with observations the velocity and displacement ground motion at stations near the Chelongpu fault of the 1999 Chi-Chi earthquake. These comparisons are presented in Appendix.

1) Introduction

Earthquake numerical models based on physics of the causative rupture and wave propagation, that incorporate conservation laws of continuum mechanics, frictional sliding, and the state of stress in the crust, have expanded our understanding of both source- and propagation-dominated ground motion phenomena (e.g., Dunham and Archuleta, 2005; Dalguer et al., 2008; Dunham and Bhat, 2008; Olsen et al., 2009). In these models the fault kinematics (slip and slip rate) and rupture propagation are determined dynamically as part of the solution of the problem, by solving, the elastodynamic equation coupled to frictional sliding. They usually idealize the earthquake rupture as a propagating shear crack on a frictional interface embedded in a linearly elastic continuum. This idealization has proven to be a useful foundation for analyzing and simulating natural earthquakes (e.g., Andrews, 1976; Das and Aki, 1977; Day, 1982a,b; Olsen et al., 1997; Oglesby et al., 1998; Dalguer et al., 2001; Day et al., 2008), and we adopt it here.

The use of these dynamic rupture models to simulate earthquakes is gaining increasing importance in the seismology and earthquake engineering community, because these models allow us to deal more closely with the physical processes that determine an earthquake and have greater potential to capture details of the physical rupture process and near-source ground motion variability. Understanding these aspects improve our capability to predict near-source ground motion, and therefore allows a more accurate assessment of the seismic hazard and risk.

It is well known that current empirical ground motion prediction equations (GMPE) are insufficient for the prediction of near-source ground motion for use in seismic hazard and risk assessment. That is because these GMPE are based solely on recorded data which are sparse in the near field, and which do not adequately represent the source effects and the geologic amplification mechanisms that have been identified in numerical simulations. Therefore physics-based numerical models are required if we are to adequately assess the level and variability of near-source ground motion, for events consistent with the maximum expected earthquake in the zone of study. For this purpose, in this project we use generic stochastic dynamic rupture models to examine ground motion characteristics for three classes of faulting (thrust, normal and strike slip) for buried and surface earthquakes. Stress and frictional strength consider two extreme cases of normal stress, 1) depth-dependent, and 2) depth-independent. The main database of synthetic ground motion assemble a set of 30 scenario earthquakes (in the range of M_w 5.5-7, see Figure 1) for each faulting style and each case (buried and surface faulting with depth and non-depth normal stress dependent) with a total of 360 simulations (Dalguer and Mai, 2012). In addition we generate couple of earthquake in dipping faults with $M_w \sim 7.8$ parameterized on a fault with geometrical characteristics of the 1999 Chi-Chi Taiwan earthquake, as well as on strike-slip faults exhibiting complexities of slip reactivation and super-shear rupture (Song and Dalguer, 2015). The resulting ground motions are compared with empirical GMPEs, we evaluate ground motion variability dominated by the source and propose a preliminary synthetic GMPE oriented to develop in the near future a hybrid GMPE, that is, using synthetic and observed ground motion.

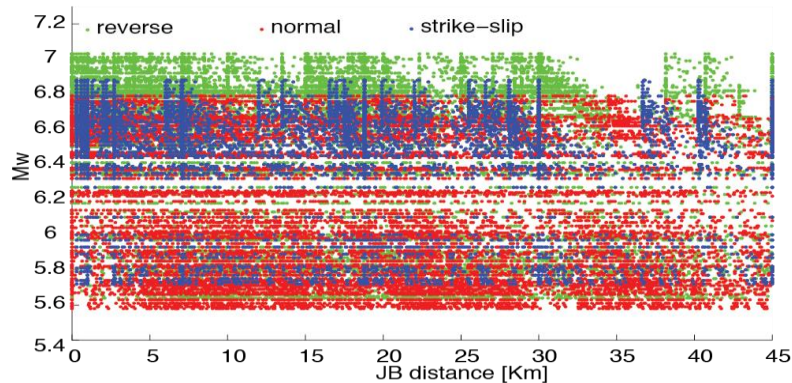


Figure 1. Magnitude vs Joyner-Boore (JB) distance of the 360 dynamic rupture models

2) General methodology for stochastic stress parameterization

2.1 Style of faulting and loading characteristic

The assumption of initial stress and frictional strength prior to earthquake are fundamental for realistic simulation of earthquakes in nature. Assuming that shear failure on pre-existing faults of shallow earthquakes is governed by Coulomb friction, the mode of faulting (Figure 2) and the loading history in compressional and extensional tectonic regimes (Figure 3) play an important role in determining the initial stress and the absolute value of frictional strength (e.g. Sibson, 1991) on the fault. Considering for example a fault system under confining pressure equivalent to the gravitational load, the tectonic loading in a compressional regime accumulates shear stress on the fault while simultaneously frictional strength is expected to increase due to increasing normal stress. In contrast, tectonic loading in an extensional regime results in a reduction of the shear strength due to decreasing normal stress (Figure 3)

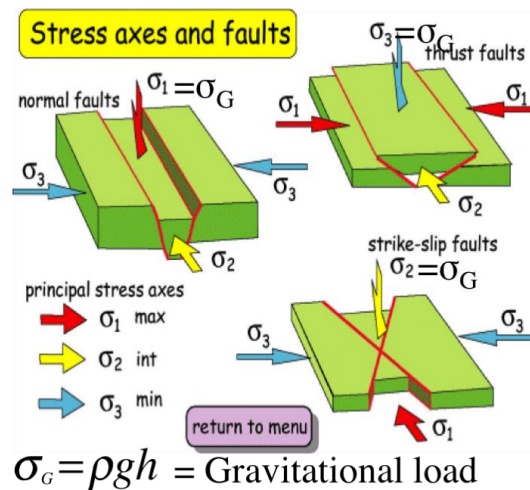


Figure 2. Idealized principal stress characteristics and mode of faulting for normal fault, thrust fault and strike slip faults

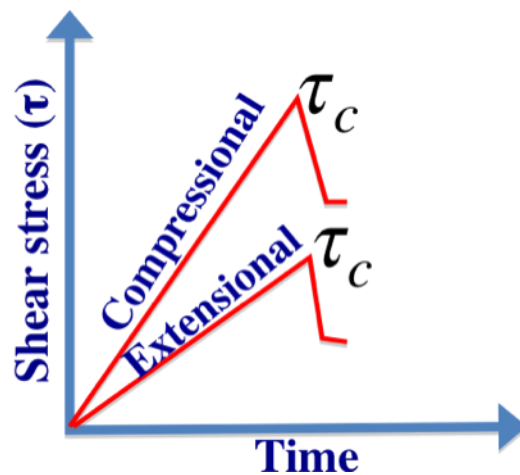


Figure 3. Loading characteristic and failure for compressional and extensional regime. For compressional regime (thrust fault) the principal stress σ_1 increase, then the normal stress σ_n and frictional strength τ_c increase as shear stress τ accumulate. For extensional regime (normal fault), the principal stress σ_3 decrease, then the normal stress σ_n and frictional strength τ_c decrease as shear stress τ accumulate

2.2 Normal Stress Depth Dependent Model.

We follow the methodology proposed by Dalguer and Mai (2008) to estimate the strength and initial stress on the fault prior to rupture. Basically this methodology combine stochastic initial stress fields with a realistic fault-loading environment as described in section 2.1, in which the tectonic loading regime (compressional or extensional) and the gravitational loading determine the absolute value of fault frictional resistance and initial stress. The procedure is as follows:

1) Assume that far-field stress is initially equal to the confining pressure, which is equivalent to the gravitational load

$$\sigma_1 = \sigma_2 = \sigma_3 = \rho gh \quad (1)$$

where σ_1 , σ_2 and σ_3 , are respectively the principal stresses, ρ the density, g the acceleration of gravity and h the depth

2) Fault loading: Adjust principal stresses according to faulting regime, i.e. increase σ_1 for thrust or strike-slip faulting, decrease σ_3 for normal faulting events. This represents a “loading” or stress-increasing mechanism for thrust/strike-slip events, and an “unloading” or stress-reduction mechanism for normal faults.

$$\begin{aligned} \sigma_1 &= \rho gh + \Delta\sigma_{load} && \text{loading} \\ \sigma_3 &= \rho gh - \Delta\sigma_{load} && \text{unloading} \end{aligned} \quad (2)$$

where $\Delta\sigma_{load}$ is the stress increment/decrement to load/unload the system

3) Estimate the normal stress acting on a specific fault plane

$$\sigma_n = \frac{1}{2}(\sigma_1 + \sigma_3) + \frac{1}{2}(\sigma_1 - \sigma_3) \cos(\theta) \quad (3)$$

where θ is the fault plane angle measured with the σ_3 axes

4) Estimate the frictional strength (assuming coulomb friction)

$$\tau_c = c + \mu_f (\sigma_n - p) \quad (4)$$

where c is cohesion stress, p is pore pressure (here: hydrostatic pressure), then $(\sigma_n - p)$ is the effective normal stress, and μ_f is the friction coefficient that depends on slip (slip weakening model) in the form given by Andrews (1976) as follow

$$\mu_f = \begin{cases} \mu_s - (\mu_s - \mu_d)u / d_0 & u < d_0 \\ \mu_d & u \geq d_0 \end{cases} \quad (5)$$

where μ_s and μ_d are respectively the static and dynamic friction coefficient, u the slip and d_0 the critical slip distance

5) Estimating initial shear stress on the fault

$$\tau_0 = \tau_{st} + \Delta\tau_{ld} \quad (6)$$

where τ_{st} is a heterogeneous stress field (Ripperger et al., 2007) generated stochastically that represents the remaining stress from the history previous events on this fault. This stochastic stress is first tapered in an arbitrary non-depth dependent frictional strength profile such that its maximum is close to the static failure stress (τ_d) and its minimum is the final stress from the last past earthquake characterized with the dynamic overshoot ($k_{osd} > 1$) or undershoot ($k_{osd} < 1$) coefficient.

$$\tau_{\max} = \tau_s ; \quad \tau_{\min} = \tau_s - (\tau_s - \tau_d) k_{osd} \quad (7)$$

Finally, the τ_{st} is again tapered to the depth dependent frictional strength profile calculated in Step 4, but keeping the same ratio $(\tau_0 - \tau_d)/(\tau_s - \tau_d)$, where τ_s and τ_d are respectively the static and dynamic frictional strength. $\Delta\tau_d$ in Equation 6 is a small stress increment for additional loading in the nucleation zone in order to initiate rupture instability (Ripperger et al 2007).

6) Nucleation zone: Determine the size of the nucleation zone, a circular patch with radius L_c , half of the critical length of an equivalent uniform fault with initial stress and frictional strength corresponding to the average over the fault. L_c has the form (e.g, Day et al, 2005):

$$L_c = \frac{\mu d_0 (\tau_{bav})}{\pi (\Delta\tau_{av})^2} \quad (8)$$

where μ is the shear modulus and τ_{bav} and $\Delta\tau_{av}$ are respectively the average breakdown strength drop and average stress drop. Depending on the stress parameterization, L_c may take on large values. Because large nucleation regions would influence the dynamic rupture properties over a large fault area, it is necessary to choose L_c as small as possible. Our numerical experiment shows that with $L_c = 2.0$ km is often enough to trigger rupture, so we assumed a maximum L_c of 2.0 km. The center of the nucleation zone is given stochastically, defined as the point in which the initial stress is equal to the yielding stress, as defined in step 4.

7) Depth-dependent crustal strength: As shown in Figure 4, our parameterization considers a stable zone (shallow part), a brittle crust (seismogenic zone) and a ductile zone (deepest layer). The parameterization with depth-dependent normal stress produces a weak zone at shallow depth incapable of maintaining large shear stress. If this shallow depth is parameterized inappropriately, early and unrealistic rupture process may take place in this zone. In addition, previous works (e.g. Brune and Anooshehpour, 1998; Day and Ely, 2002) suggest that rupture within this weak shallow zone should operate in a distinctively different fashion than the rest of the fault, i.e. showing strength hardening due to the formation of incompetent fault gouge, micro cracking (e.g. Marone, 1998; Marone and Scholz, 1988), or fissuring of rocks and other forms of off-fault zone damage due to the presence of sedimentary surface deposits. The main feature of this shallow depth zone is that it operates during rupture with an enhanced energy absorption mechanism. We therefore define the first 2 km depth as a weak shallow zone that follows strength hardening during frictional sliding. To model this frictional behavior, we assume negative stress drop and large critical slip distance in the stable uppermost layer (Figure 4). The seismogenic zone, below the stable zone, represents the brittle crust of the earth. We model it as an 18 km thick layer. Below this seismogenic layer, we consider a ductile zone, characterized by large critical slip distance (Figure 4). Rupture may propagate dynamically into the weak shallow layer or into the deep ductile zone, but cannot nucleate in this region. Once the dynamic rupture has entered this zone, it quickly terminates as the energy-absorption at the crack tip exceeds the energy supplied by the propagating crack.

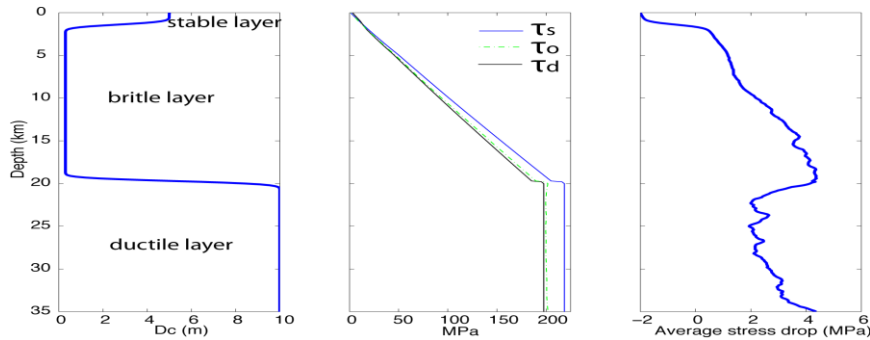


Figure 4. An example of depth variation of frictional parameters averaged along the strike of the fault, adopted in the dynamic rupture models. Left figure shows critical slip distance. Center shows the static frictional strength (τ_s), initial stress (τ_0) and dynamic frictional strength (τ_d). Right figure shows the stress drop.

2.3 Normal Stress Non-depth Dependent Model.

The stress parameterization for this case follows the same procedure as described above, with the difference that the normal stress acting on the fault is constant over the fault.

3) Fault Model Parameterization

The 360 dynamic rupture models are parameterized as follow:

- Strike-slip faulting: dip=90°, fault length = 30km, fault width=12km
- Thrust faulting: dip=45°, fault length = 24km, fault width=15km
- Normal faulting: dip=60°, fault length = 24km, fault width=15km
- For ruptures that are not allowed to break the surface, the faults are buried at 5km depth
- Static friction coefficient = 0.6, dynamic friction coefficient = 0.56, cohesion force = 1.0×10^6 Pa;
- dynamic overshoot coefficient = 1.5 critical slip distance = 0.2
- critical slip distance smoothly increases from 0.3 m to 5 m at fault boundaries in a 3 km-wide buffer zone that surrounds the above defined fault areas; this approach ensures that rupture propagation stops smoothly at the borders of the fault
- loading under compression (trust/ strike slip fault), unloading under extension (normal fault) = 50×10^6 Pa. The loading is applied at 15km depth.
- strike-slip faults have the principal stress σ_2 equal to the average between σ_1 and σ_3 , and the angle θ of equation 2 is 45° (fault plane angle measured with the σ_3 axes)
- initial stress stochastic field realizations based on von Karman distribution with correlation length of 8.0 km in along-strike and along-dip direction, Hurst number $H = [0, 0.25, 0.5]$; resulting stress distribution are hence compatible to seismological observations (Mai and Beroza, 2002).
- normal stress = 120 MPa, for model with non-depth dependent stress
- numerical setup uses 8 grid element per wavelength; a conservative estimate yields that we accurately resolve a maximum frequency of ~3 Hz, given the chosen velocity structure and grid size of 100 m; domain-size 100 km x 100 km x 30 km
- simulations were carried out on a Cray XT5 at the Swiss National Supercomputing Center (CSCS) on 4096 CPUs; a typical run requires about 1hr, i.e. we used ~4000 CPU-hrs per simulation.

4) Numerical technique used for dynamic rupture simulation

The dynamic rupture models and near-source ground motion simulations have been developed using the Support Operator Rupture Dynamics code (SORD). The SORD code developed by Ely et al., (2008, 2009) uses a generalized Finite Difference (FD) scheme that can utilize structured

hexahedral grids to mesh irregular geometry following a second-order accurate support operator scheme (e.g., Shashkov, 1996) with the capability to model general fault geometry and topography. SORD solves the three-dimensional visco-elastodynamic equations of motion; its scheme is explicit in time. The fault is represented by the split-node technique (Day et al, 2005; Dalguer and Day, 2006, 2007). The dynamic rupture occurs as dictated by the local stress conditions following a linear slip-weakening frictional failure law (equation 5). The code is parallelized, using Message Passing Interface (MPI), for multiprocessor execution, and is highly scalable, enabling large-scale earthquake simulations. The dynamic rupture model has been validated through the Southern California Earthquake Centre (SCEC) dynamic rupture code validation exercise, showing good agreement with semi-analytical boundary integral methods (Harris et al., 2009). The spatial resolution of the models is $dx=dy=dz=0.1\text{km}$ for our case study. The calculation was performed on Rosa supercomputer, a Cray XT5 computer at the Swiss National Supercomputing Center (CSCS), using 8192 processors for one simulation. The calculations of the rupture models of dipping faults with geometrical characteristics of the 1999 Chi-chi earthquake were performed in the Kei super computer resources of the Foundation for Computational Science of Japan using 1042 processors for one simulation.

5) Numerical Results of the 360 dynamic rupture models

Part of the results presented here has been published in Dalguer and Mai (2012) and Baumann and Dalguer (2014).

Dynamic Rupture Solutions. From the total of 360 models, a diversity of rupture scenarios has been simulated in a range of M_w 5.5 – 7.0. Figures 5, 6 and 7 show respectively for strike, reverse and normal-slip fault, representative models with the same stochastic stress parameterization for each type of rupture. The rupture propagation, slip, peak slip velocity and stress drop distribution evolve in a diverse manner within the three class of faulting. For each case of rupture (buried and surface-rupturing) models with non-depth dependent stress parameterization results in solutions with larger stress drop, but earthquake size is larger for depth dependent stress models. Surface rupturing model with depth dependent stress predict the largest size earthquake, but the non-dependent stress model results in the largest peak slip rate values.

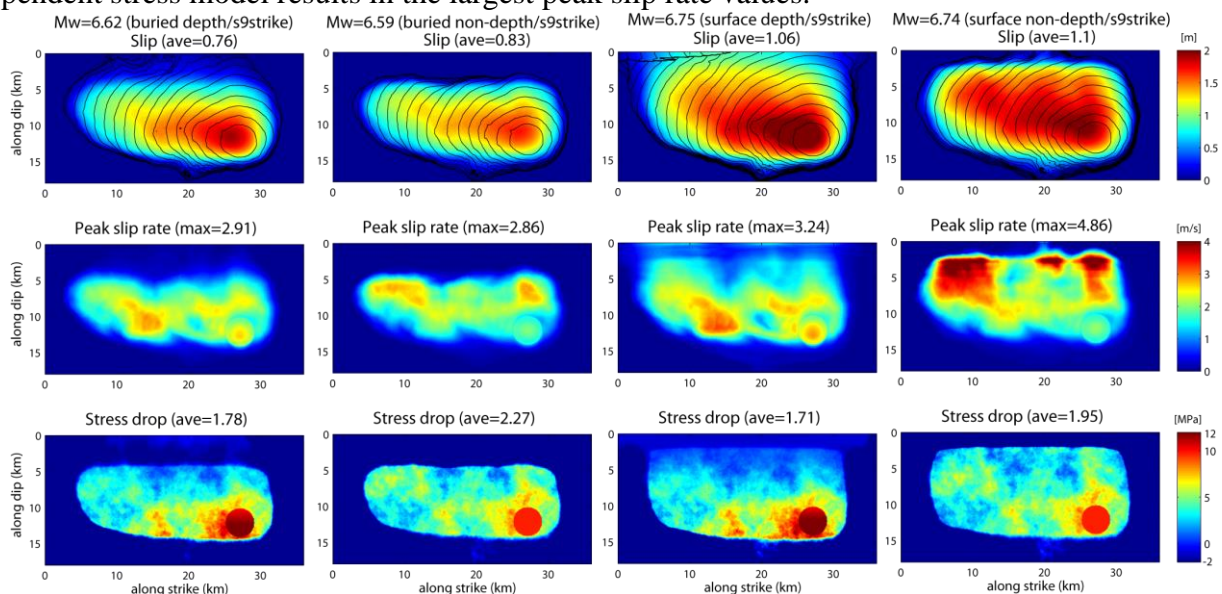


Figure 5. Dynamic rupture solutions for a strike-slip rupture with the identical stochastic stress parameterization, for depth and non-depth dependent stress and for buried and surface-rupturing models. Top shows slip distribution, contour line is the rupture time each 0.5 sec. Center shows peak-slip distribution, and bottom is stress drop distribution.

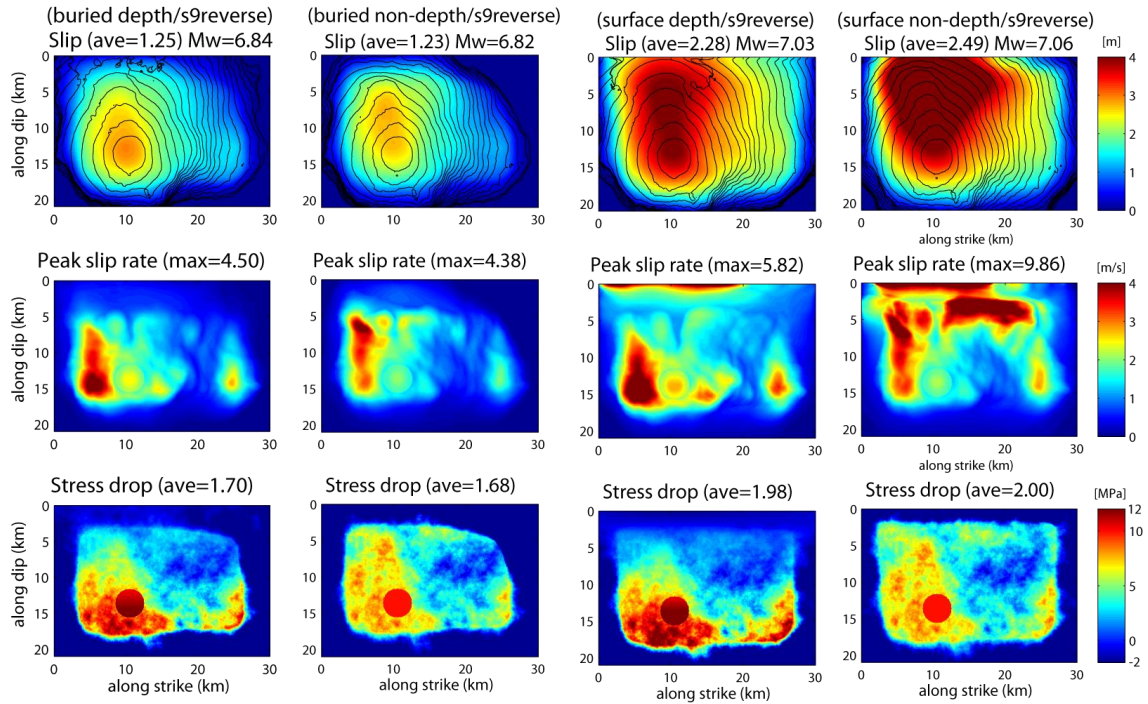


Figure 6. Dynamic rupture solutions for reverse-slip rupture with the identical stochastic stress parameterization, for depth and non-depth dependent stress and for buried and surface-rupturing models. See Figure 3 for details.

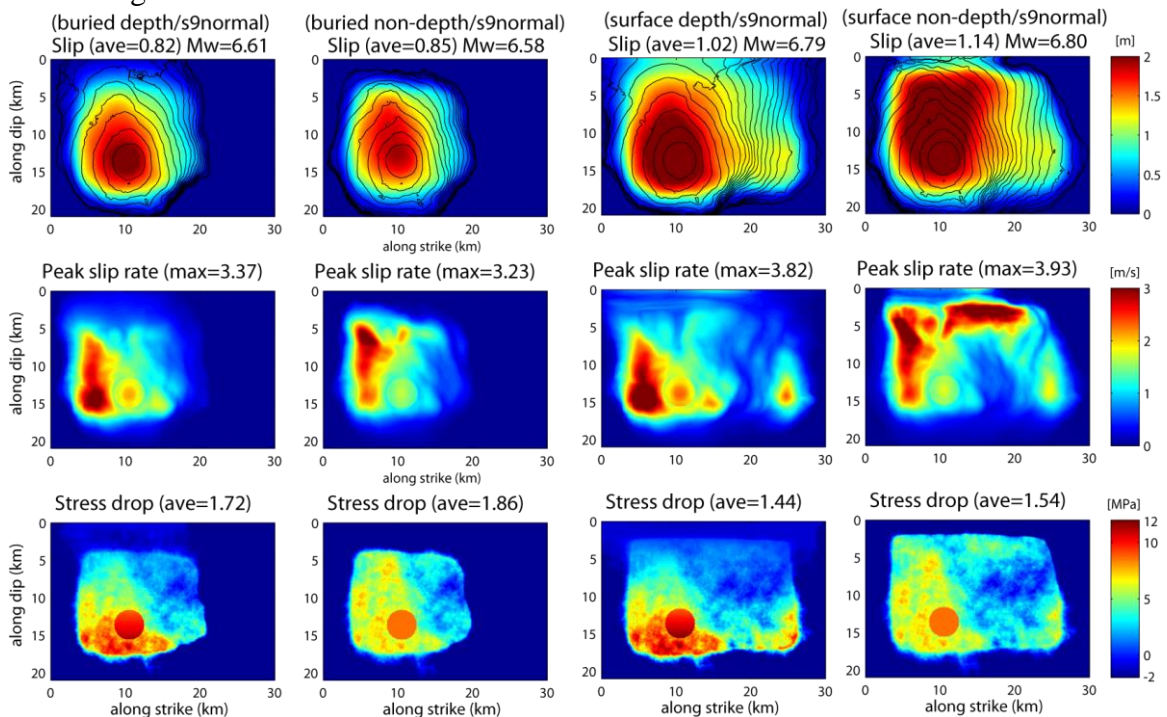


Figure 7. Dynamic rupture solutions for a normal-slip rupture with the identical stochastic stress parameterization, for depth and non-depth dependent stress and for buried and surface-rupturing models. See Figure 3 for details.

Ground Motion Solutions.

We compare the resulting ground motions of all 360 models to common ground-motion prediction equations (GMPE) and observations, focusing on the maximum ground motion generated by these models. Site-amplification corrections using the period-dependent amplification coefficient of Borchardt (1994, 2002) are applied to scale computed ground motions to $V_{s30}=1500\text{m/s}$ from the

minimum shear-wave velocity in our simulations ($V_{s30}=2500\text{m/s}$). This correction is needed to facilitate the comparison with the GMPE's that are based on V_{s30} -values less than 1500 m/s . Synthetic ground motions are filtered using a band pass Butterworth filter from 0.01 to 3.0 Hz . Figure 8 displays PGV and PGA (for wave forms up to $f_{\text{max}} = 3\text{ Hz}$) for all models. We find that surface rupturing models predict stronger ground motion than buried rupture, with the strongest corresponding to non-depth dependent stress models, acceleration exceeding in some case gravity. Strike slip models predict the strongest ground motion, followed by reverse-slip rupture models. Maximum ground motion levels is constant up to $M_w\sim 6.3$ for strike slip fault, and up to $M_w\sim 6.7$ for reverse and normal faults. Differences in ground-motions between buried ruptures with depth and non-depth dependent stress are indistinguishable.

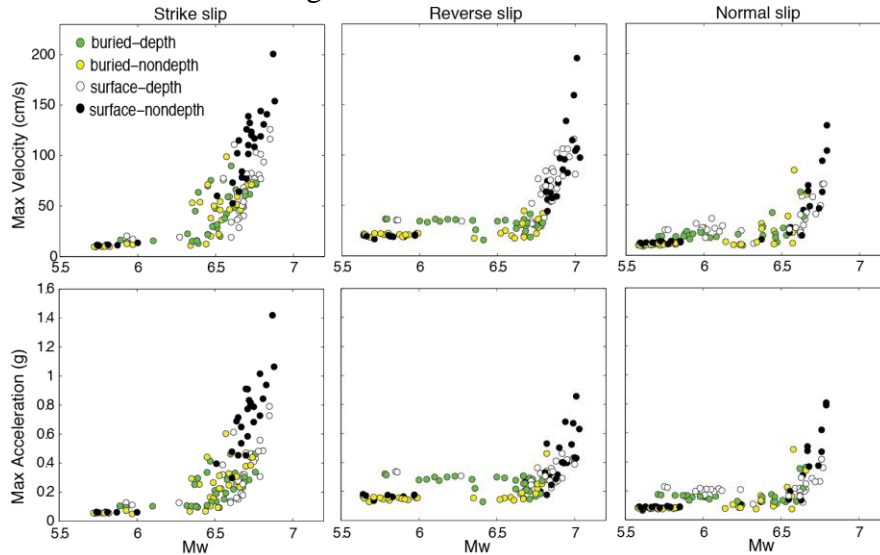


Figure 8. Maximum horizontal ground motion of velocity (top) and acceleration (bottom) for strike, reverse and normal faults of buried and surface rupturing with depth and non-depth dependent stress for a total of 360 models.

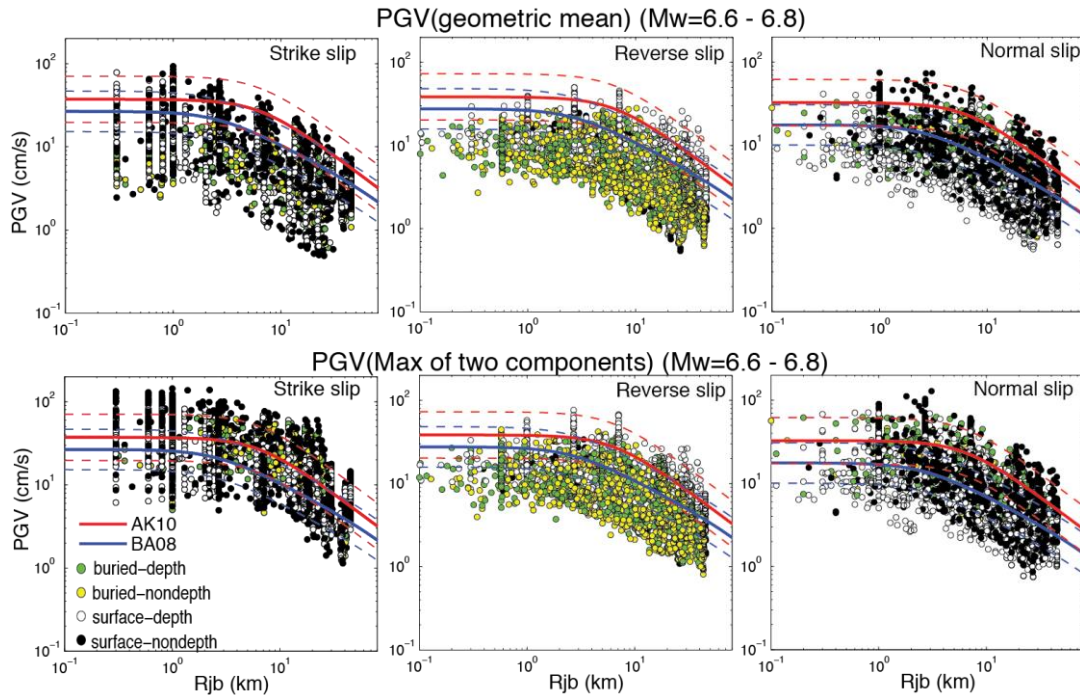


Figure 9. Horizontal PGV comparisons with GMPE from AK10 (Akkar and Bommer, 2010) and BA08 (Boore and Atkinson, 2008) and for strike, reverse and normal faults of buried and surface rupturing with depth and non-depth dependent stress, for models in the magnitude range M_w 6.6 –

6.8. Top shows comparison using the classic geometric and bottom correspond to the maximum of the two horizontal components.

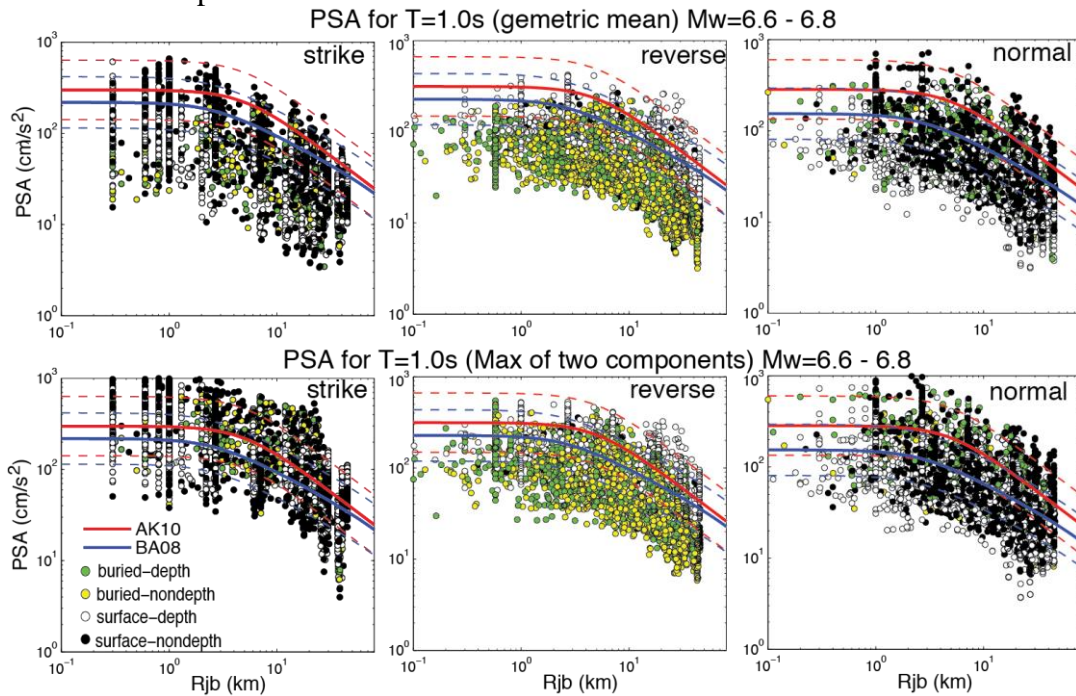


Figure 10. Horizontal Pseudo Spectral Acceleration (PSA) at period $T=1.0s$ compared with GMPE of AK10 (Akkar and Bommer, 2010) and BA08 (Boore and Atkinson, 2008) for strike, reverse and normal faults of buried and surface rupturing with depth and non-depth dependent stress, for models in the magnitude range M_w 6.6 – 6.8. Top shows comparison using the classic geometric and bottom correspond to the maximum of the two horizontal components.

Figures 9 and 10 compare, respectively, PGV and PSA (at period $T=1.0s$) with GMPE from Akkar and Bommer (2010) hereafter AK10 and Boore and Atkinson (2008) here after BA08, for a range of magnitude of M_w 6.6 – 6.8. We use Joyner-Boore Distance (R_{jb}). The PGV and PSA estimate from our simulations are calculated assuming two criteria, the geometric mean of the two maximum horizontal components (top of Figure 9,10) and the maximum value of the two maximum horizontal components (bottom of Figure 9, 10). In general PGV and PSA are consistent with GMPE, with better fitting at distance R_{jb} larger than about 3-7 km than at very close distances to the fault. Estimates using the maximum criterion provide better comparison than the geometric mean criterion. We find an increased variability in the near-field of the rupture. The consistent saturation of these quantities as predicted by GMPE is not obvious in our calculations. Rather, there are significant ground-motion reductions near the source for buried faults and for dip-slip ruptures, but considerable increase for strike slip surface rupturing earthquakes.

Quantitative comparison with empirical GMPE

We compare the synthetic data with the GMPE of AK10. The deviation of the synthetics from the empirical model is measured by applying the concept of residuals (Strasser et al., 2009). The ground-motion residuals are defined as the difference between the observed (obs) and the predicted (pre) ground motions from GMPE. Figure 11 shows the SA residuals of the 360 models at periods 0.1, 0.2, 0.3, 0.4, 0.5, 0.6, 1.0, 2.0, and 3.0 s for JB distances of 10 km interval length. Overall, this figure reveals that the mean residuals fall in the range of σ , for periods greater than or equal to 1.0 s. For short periods, the residuals dramatically drop to lower values. It suggests that, in general, stable ground-motion solutions consistent with the empirical model are expected for frequencies lower

than or equal to 1.0 Hz, which leads us to conclude that the upper-bound frequency of the synthetic ground motion generated by our 360 models is 1.0 Hz.

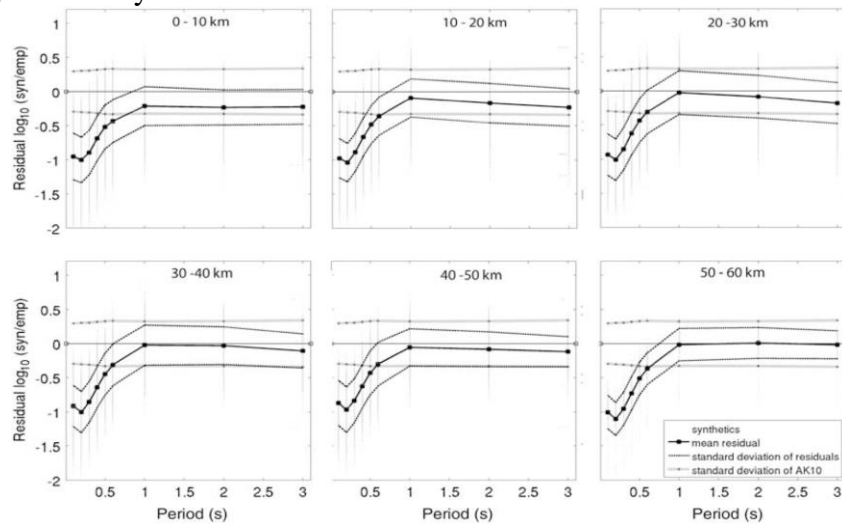


Figure 11. Spectral acceleration residuals at periods of 0.1, 0.2, 0.3, 0.4, 0.5, 0.6, 1, 2, and 3 s for as a function of JB distances of 10 km intervals.

Effect of source parameters on ground motion residuals

We examine the residual of SA at $T=1:0$ s (Fig. 12) of the 360 synthetic models as a function of average stress drop, peak slip rate, and rupture speed. As shown in these figures the residuals show clear trends of dependence on stress drop and peak slip rate. In this case, the mean residuals serve as an indicator of the variability of the ground motion with respect to the mentioned source parameters. The effects of stress drop, peak slip velocity appear to be sensitive to the peak ground motions. Therefore, our calculations suggest that the introduction of these source parameters in the source term of GMPEs may contribute to reduce the standard deviation.

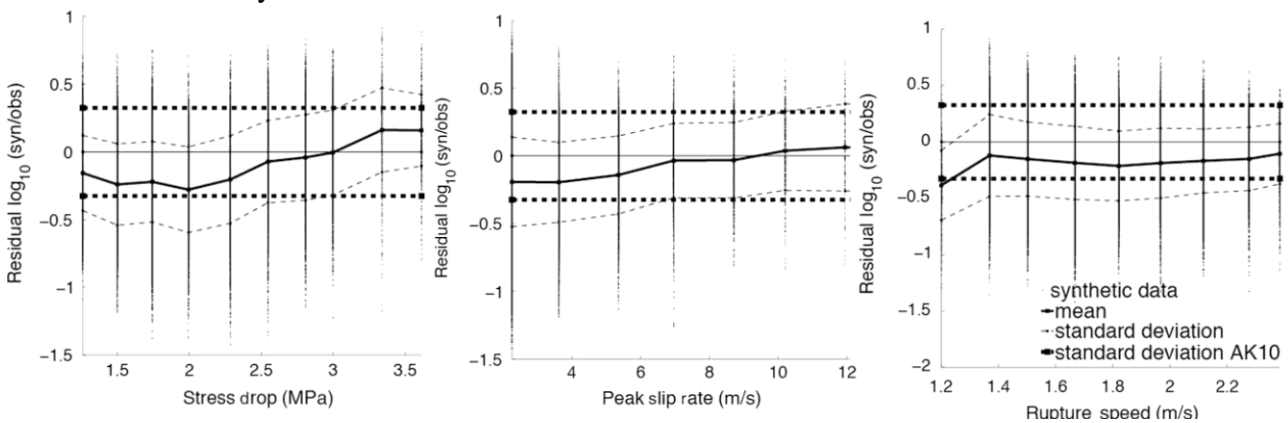


Figure 12. Spectral acceleration residuals at period 1.0 s of all 360 models as a function of average stress drop (left), peak slip rate (center) and rupture speed (right).

Extreme ground motion. The synthetic earthquakes of some models generate very strong ground motion that appears to be correlated with faulting that breaks the free-surface. The strongest motion is for strike-slip rupture, predicting acceleration ground motion exceeding the gravity. Figure 13a shows a representative of PSA exceeding the gravity predicted by surface rupturing of strike, reverse and normal-faulting models with non-depth dependent normal stress. As seen in this figure, gravity is exceeded at frequencies in the range of 1.0 – 2.5 Hz ($T = 0.4 - 1.0$ s). For reference, Figure 13b displays PSA at several stations exceeding gravity during the 2011 M_w 6.3 Christchurch, New Zealand earthquake, in which extreme ground motion were observed in the same frequency range.

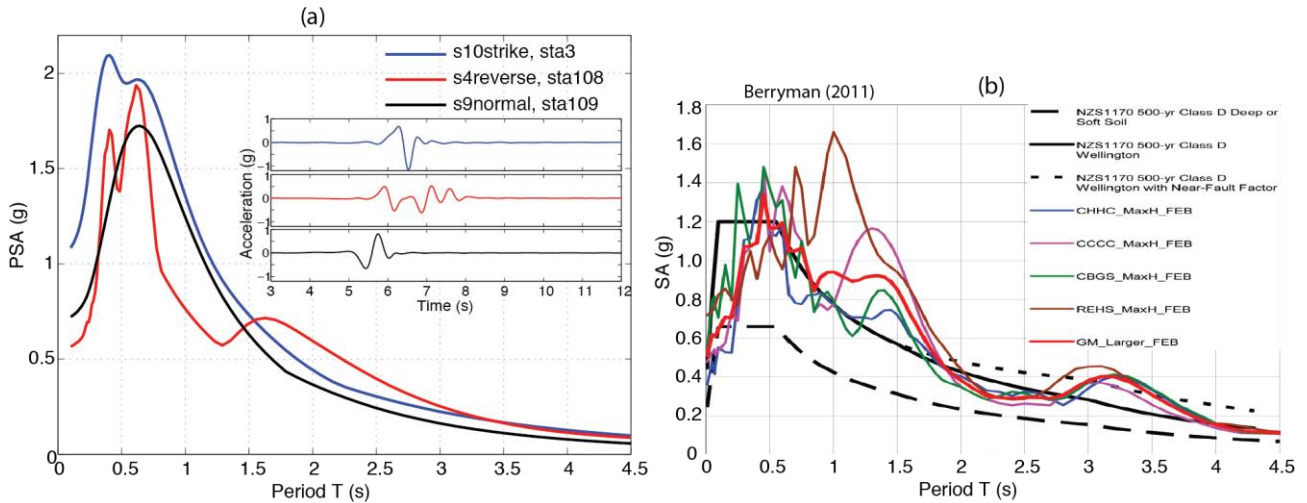


Figure 13. Left (a) PSA at selected station very near the source for strike, reverse and normal faulting with surface rupturing and non-depth dependent stress; the inset figure displays the corresponding acceleration time histories. Right (b), Spectral Acceleration at several stations exceeding gravity during the 2011 M_w 6.3 Christchurch, New Zealand earthquake (After Berryman, 2011). Solid and dashed black line are design spectral motions.

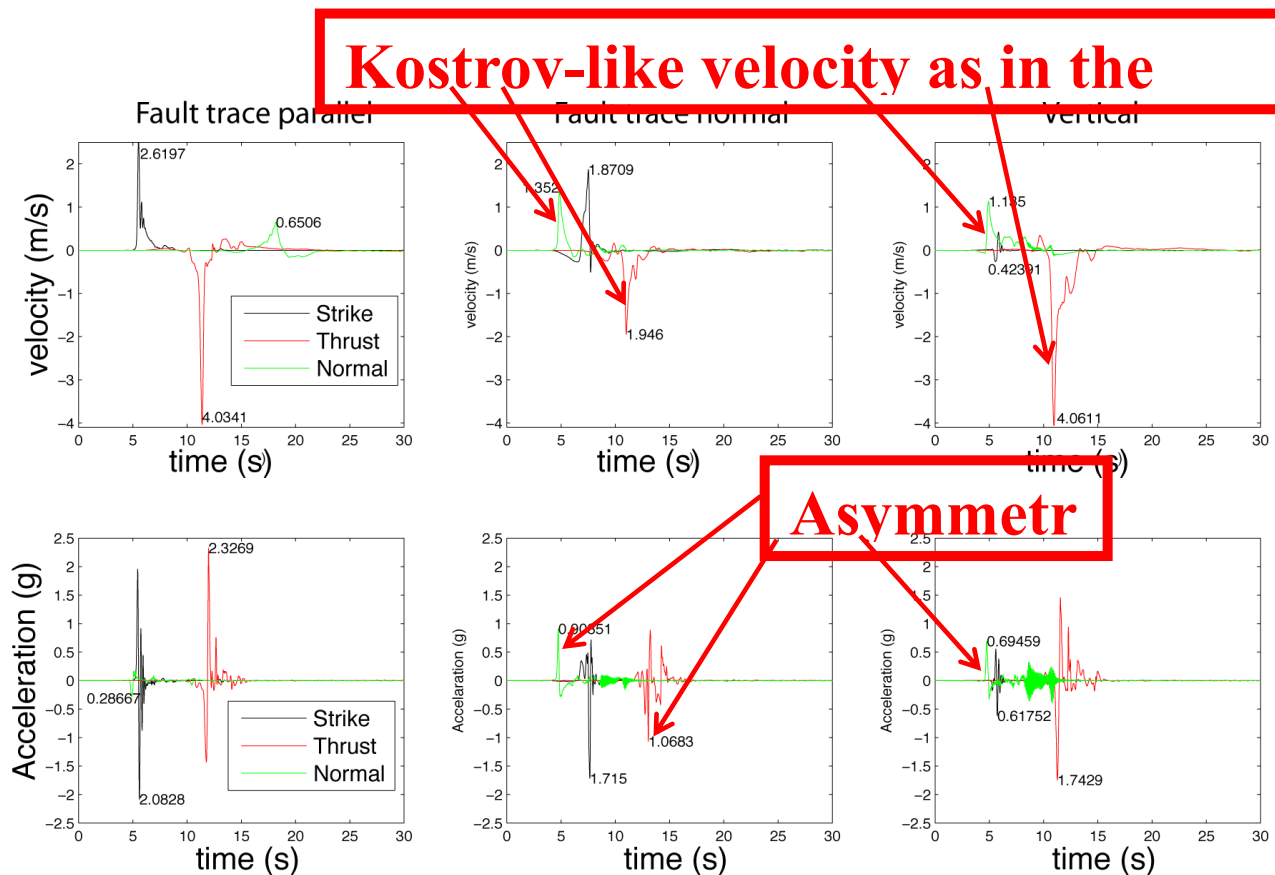


Figure 14. Near-field velocity (top) and acceleration (bottom) waveforms for surface-breaking strike-slip, thrust and normal faulting. Red arrows point Kostrov-like velocity ground motion (top) and asymmetric acceleration ground motion (bottom).

Figure 14 displays near-source velocity and acceleration waveforms, showing asymmetry in the acceleration time history as expected for dipping faults. The asymmetry seen in our numerical simulation is also pronounced in the vertical and normal components, and can be attributed to source effect due to the Kostrov-like slip velocity characteristics that dominates the near source ground motion. Notice that the normal component for strike slip fault also generate asymmetric ground motion acceleration. For accelerations above 1g this asymmetry is more noticeable in observed natural earthquakes (e.g. Aoi et al, 2008; Yamada et al, 2009).

Supersaturation of ground motion near the source

The consistent saturation of ground motion very near the source as predicted by empirical GMPE is not obvious in these synthetic earthquakes, rather there is a tendency of ground-motion reduction near the source, indicating oversaturation, as shown in Figure 15. This supersaturation feature has been suggested by some observations (Akkar and Bommer, 2007b; Graizer and Kalkan, 2007, 2011). In Figure 15 we plotted the PGV as a function of JB distance for earthquakes larger than M_w 6.5 in our database. Clear supersaturation of the average PGV values is observed for buried strike-slip earthquakes at distances less than 1.0–2.0 km. Similar features are observed for SA estimates (not shown here).

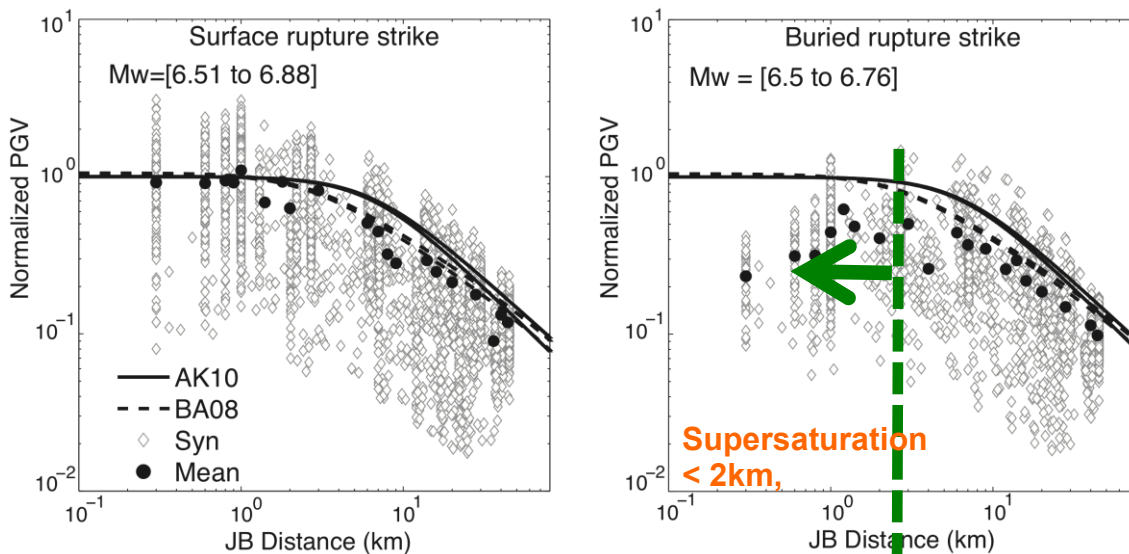


Figure 15. Synthetic PGV (open diamonds) as a function of Joyner–Boore (JB) distance, compared with the GMPE of AK10 (solid line) and Boore and Atkinson (2008; BA08) (dashed line) for strike-slip surface rupture (left) and buried rupture (right) data is normalized with the corresponding maximum value predicted by AK10. The two solid and two dashed lines, nearly overlapping, correspond to the minimum and maximum event shown in the M_w interval at the top of each figure. The black circles represent the average of the synthetic PGVs around the given distance. Notice the clear reduction (supersaturation) of the average PGV values for buried strike-slip earthquake at distances less than 1.0–2.0 km.

6) Implementation of physics-based GMPE

Source effects from hanging wall and directivity, as well as oversaturation of ground motion near the source observed in the 360 dynamic rupture models are parameterized here (Cauzzi and Dalguer, 2015, in preparation). The main findings of this effort are reported here:

The residual between the 360 dynamic rupture models and current empirical GMPEs (Akkar et al., 2014) are computed (Fig. 16). Trends are apparent in the data distribution as a function of magnitude and distance. That is, the functional forms typically adopted for empirical predictions of

peak ground-motions and response spectra cannot be directly used to fit synthetic near-field ground-motion data or, in other words, the particular features of near-field ground-motions are not captured by the relatively simple parameterisation of current empirical GMPEs.

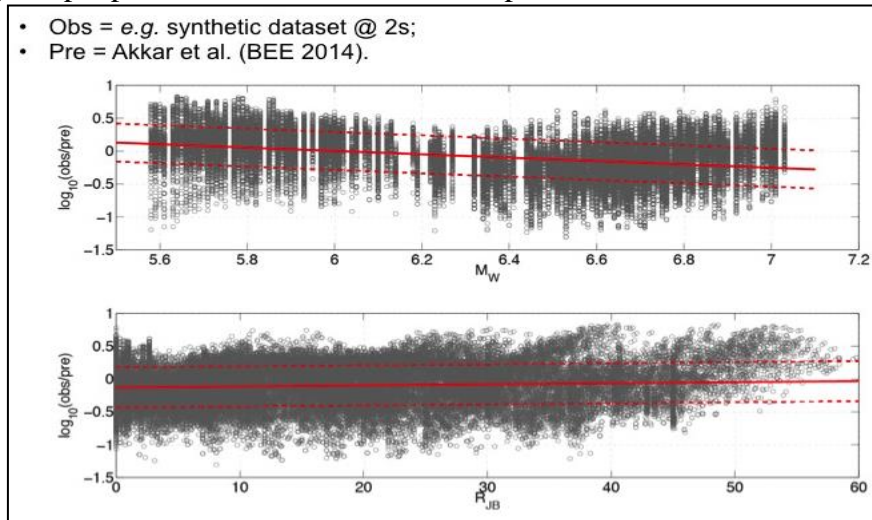


Figure 16. Residuals of the 360 synthetic dataset with respect to the empirical prediction model of Akkar et al. (2014).

We used the 360 rupture models to investigate the variation of near-field peak ground-motion and response spectra with

- Moment magnitude M_W ;
- finite-fault distance (both R_{RUP} and R_{JB});
- near-source characteristics like the hanging-wall / foot-wall location, directivity and radiation pattern effects.

We used synthetics: a) to overcome the difficulties posed by the paucity of near-field data in the calibration datasets of empirical ground-motion prediction equations (GMPEs); b) to expand our understanding of source-dominated ground-motion phenomena; c) to investigate the characteristics of “noise-free” long-period ground motions. The most interesting (*i.e.* different from the current GMPE approaches) results that we obtained are selectively summarized in the following paragraphs.

Linear scaling with magnitude for vibration periods larger than 2 s, where the numerical simulations contain enough energy to be considered technically reliable (Fig. 17). The prediction of magnitude scaling would then use one predictor (M_W) and two period-dependent coefficients. This is consistent with the functional form adopted by Cauzzi and Faccioli (2008), who used a worldwide databank – albeit dominated by Japanese data – to derive long-period spectral predictions for M_W 5-7+. Note that the same authors (Cauzzi et al., 2014) used recently a quadratic scaling with magnitude – as many other GMPE modelers do – as a result of enlarging their original dataset to the range 4-8.

Amplification factors due to style-of-faulting. We found that the faulting style can be reasonably modeled by means of amplifications factors for normal and reverse and strike-slip mechanism with respect to unspecified (Fig. 17). That is, using dummy variables for different faulting styles when performing regressions on the synthetic dataset. The prediction of style-of-faulting impact would then use three predictors (N , R , S) and three period-dependent coefficients.

Attenuation with finite-fault distance metrics R_{JB} and R_{RUP} . We found that classical functional forms based on the geometric attenuation of spectral amplitude with distance are valid for the synthetic dataset but (Fig. 18):

- a magnitude dependent geometric decay could be explicitly modeled only if R_{RUP} was used as predictor;
- a magnitude-dependent saturation with distance could be explicitly modeled only if R_{RUP} was used as predictor;
- the fictitious depth h to be used with R_{JB} could be modeled as a function of the depth to the top of rupture Z_{TOR} ;
- data showed larger dispersion if represented as a function of R_{JB} .

Therefore modeling the attenuation with distance required using two predictors and up to four period-dependent coefficients.

Near-source oversaturation of spectral amplitudes generated by strike-slip events. Similar to Graizer et al. (2013) we observed oversaturation of spectral values for distances shorter than the depth to the top of rupture (Z_{TOR}). This near-source oversaturation effect can be reasonably modeled as a cosine taper for distances shorter than (Z_{TOR}) as shown in Fig. 19, *i.e.* using two predictors and two period-dependent coefficients. Note that strike-slip events in the dataset occur on vertical faults only.

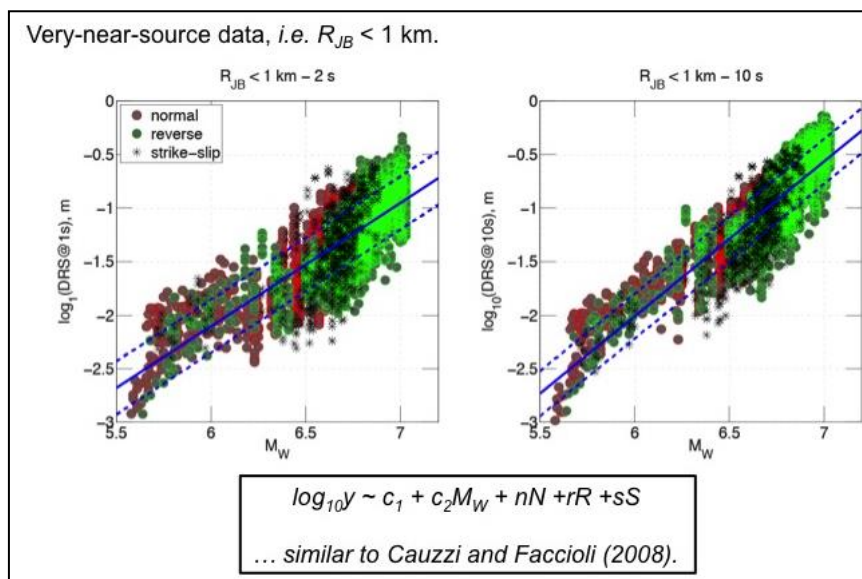


Figure 17. Magnitude scaling and style-of-faulting effect at a glance.

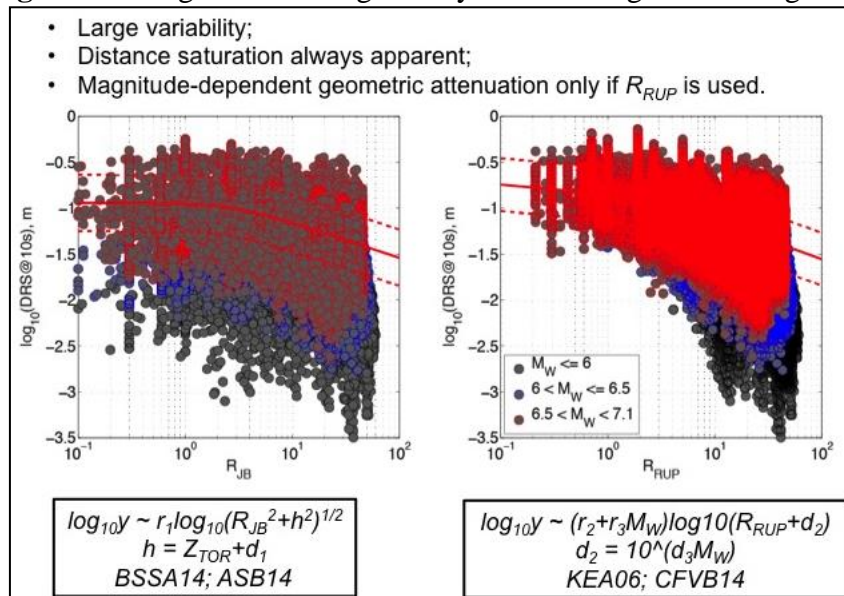


Figure 18. Geometric attenuation of long-period spectral ordinates with finite fault distance metrics R_{JB} and R_{RUP} .

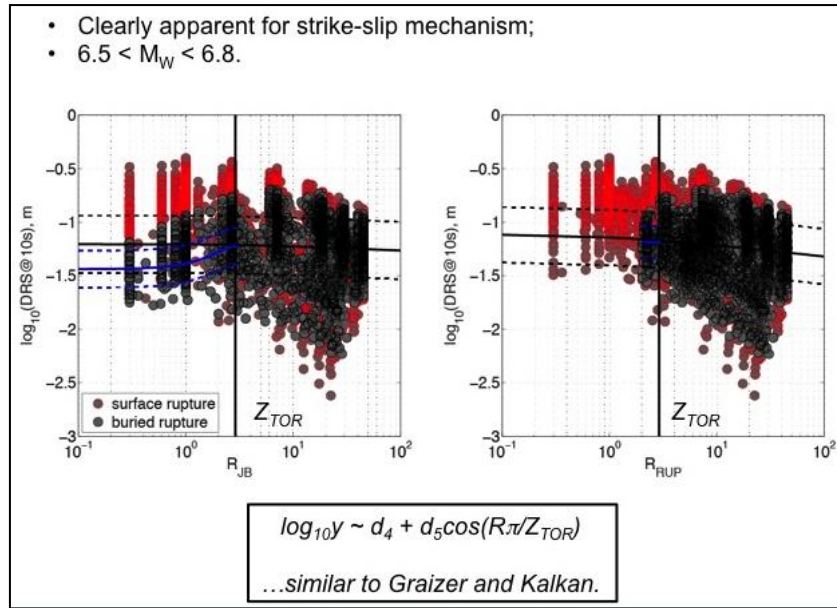


Figure 19. Near-source oversaturation of spectral amplitudes generate by strike-slip vertical fault events.

Hanging-wall amplification effect. Consistent with the latest approaches developed within the NGA project, we found a clear signature of increased spectral levels at stations located on the hanging-wall side of large-magnitude dipping-fault events. Our results show that the hanging-wall effect is a quadratic function of the distance from the fault strike (R_X) within the surface projection of the ruptured fault, and a cubic decreasing function of R_X otherwise. That is, the hanging-wall term parameterisation requires one predictor (R_X) and up to three period-dependent coefficients (Fig. 20).

Directivity. We could explain the lower and upper bounds of the synthetic spectral amplitudes based on directivity. We found that the approach developed by Bayless and Somerville within NGA West-2 (see Spudich et al., 2014) seems to apply also for the 360 synthetic dataset, as shown in Fig. 21.

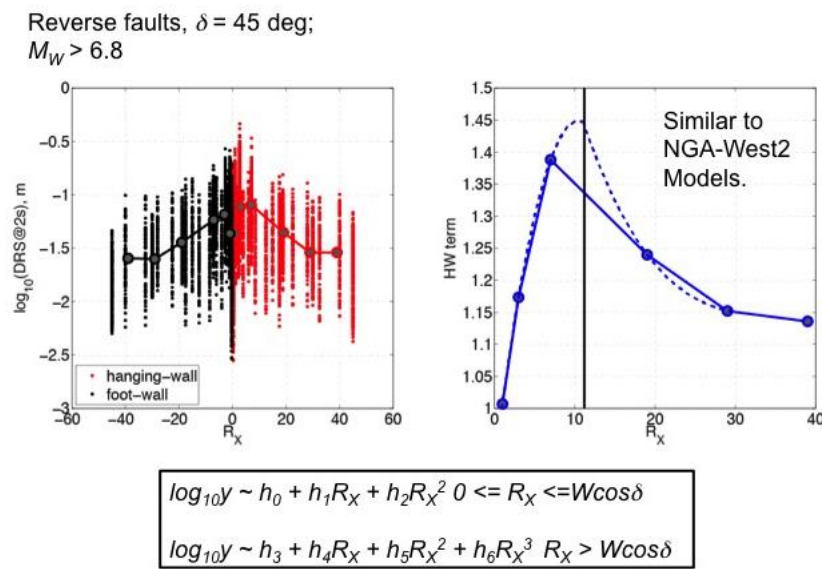


Figure 20. Hanging wall (HW) effect and HW term parameterisation that requires one predictor (R_X) and up to three period-dependent coefficients.

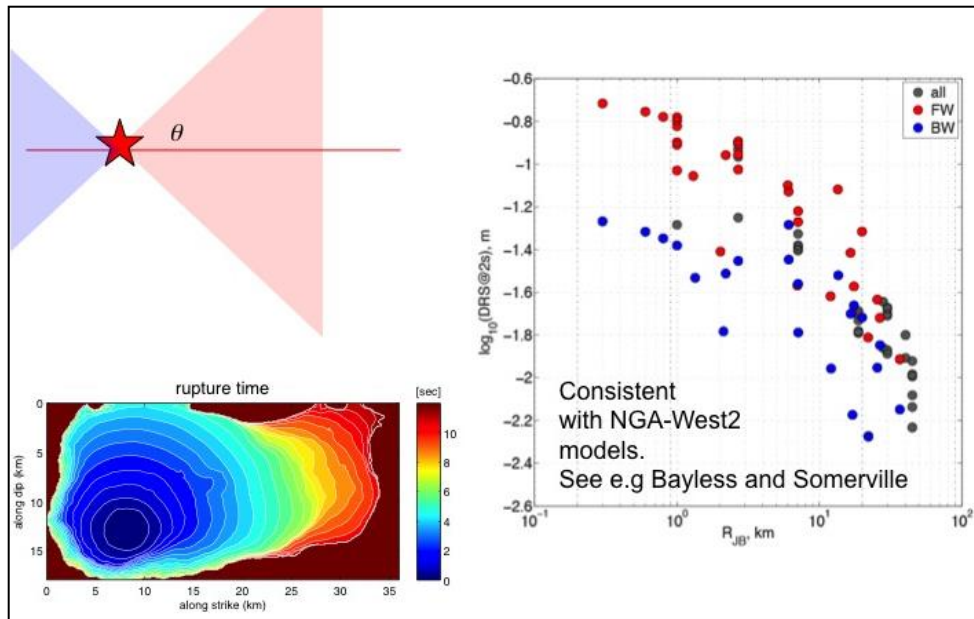


Figure 21. Effect of directivity on the simulated spectral amplitudes.

7) Rupture complexity of stochastic models (Supershear and slip reactivation)

Supershear rupture: Physics-based models (e.g., Andrews, 1976b) and observational evidence suggest that supershear ruptures are possible, especially for large strike-slip events. The first supershear rupture inferred from observations was reported for the 1979 Imperial Valley earthquake (Archuleta, 1984; Spudich and Cranswick, 1984). Subsequently, a number of large strike-slip earthquakes appeared to rupture with supershear velocity (Dunham, 2007; Bizzarri and Spudich, 2008). We calculate the rupture speed of our stochastic models and evaluate its variability on the fault. Figure 22 shows snapshots of slip velocity in representative rupture models of strike-slip fault in which local and full supershear rupture speed take place. Figure 23 shows histograms of rupture speed (V_r) normalized with the S wave velocity distributed over the fault plane for strike-slip models (these models are not part of the 360 database). The vertical axes of the histograms in Figure 23 show the number of points (subfaults) that experience the velocity ratios on the horizontal axis. Each entry shows the local value on the subfault. These histograms show that local supershear rupture velocities exist for events of all sizes, although the average rupture velocity of most of the events remains subshear. The effects of the local supershear rupture speed on ground motion is a topic of future investigation.

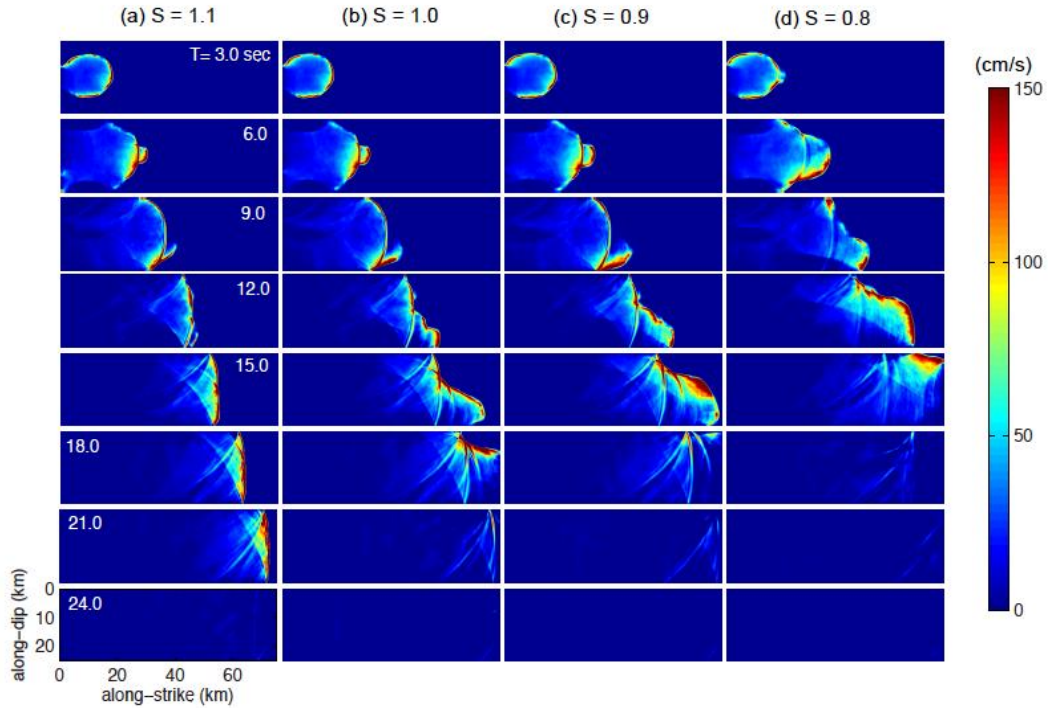


Figure 22. Snap shots every 3 seconds of slip velocity for models with different level of S parameter (ratio of strength excess divided by stress drop). Notice rupture front propagates with supershear speed at localized area (left figure), and as S decreases the supershear speed dominate all the fault (right figure).

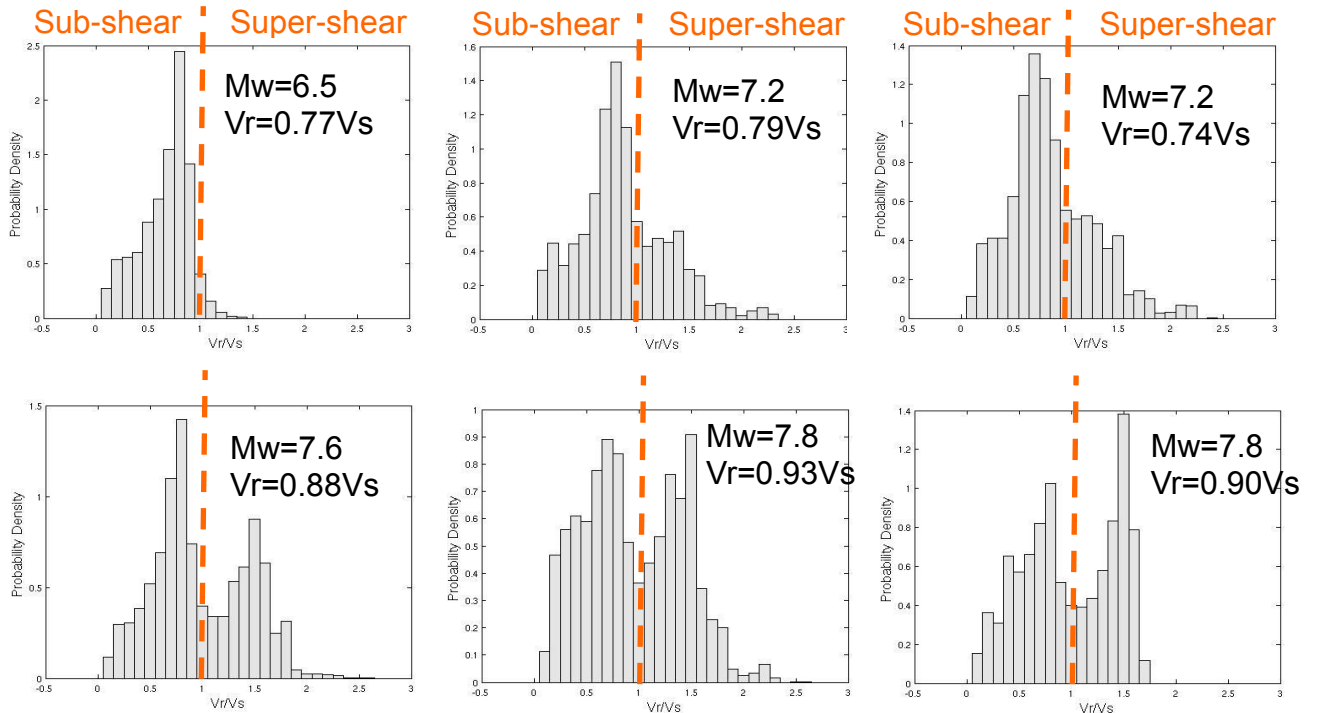


Figure 23. Histograms of the ratio of rupture speed and S wave velocity for models with M_w from 6.5 to 7.8. Dashed vertical lines are located at ratio of 1, in which divides the subshear and supershear rupture occurrence (Mena et al, 2012).

Slip reactivation. Complex rupture patterns such as slip reactivation and back rupture propagation has been identified by 2D dynamic rupture models (Gabriel et al., 2012). Observations of the 2011 Tohoku earthquake also suggest slip reactivation process of the rupture, as shown by kinematic source Inversions of Lee et al. (2011). Here we develop stochastic models with slip reactivation assuming double stress drop during rupture with slip weakening friction model. Figure 24 show snap shots of such models with different levels of slip reactivation. The effects of slip reactivation on ground motion is also a topic of future investigation.

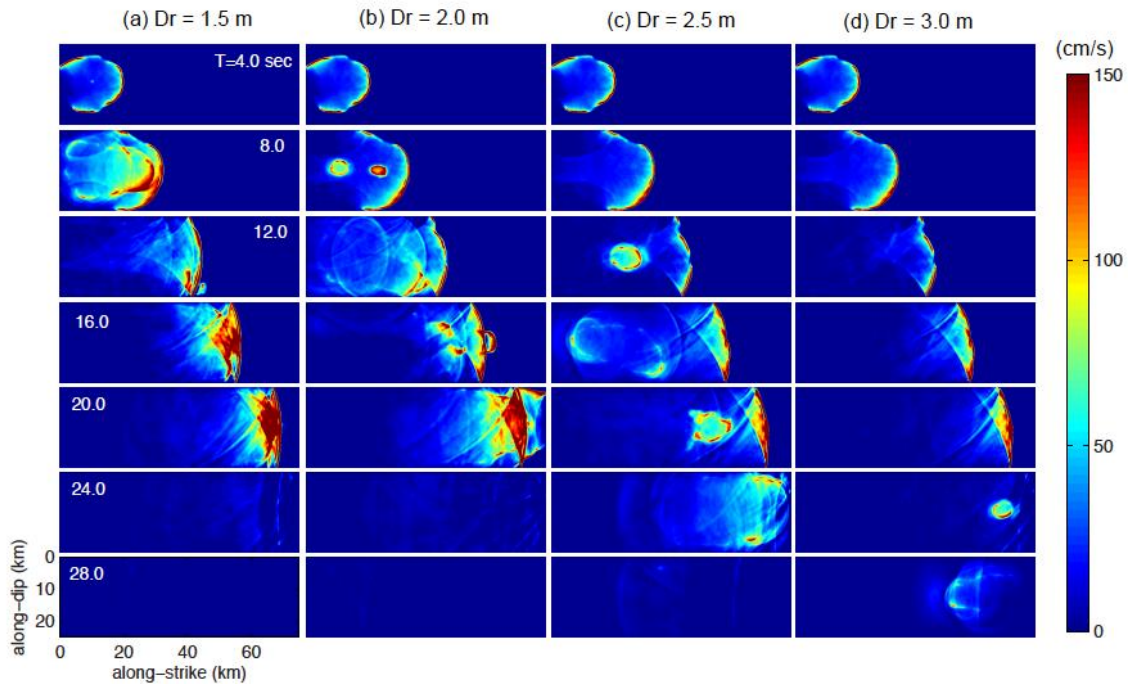


Figure 24. Snap shots every 3 seconds of slip velocity for models with different level of the D_r parameter (D_r is a slip parameter in which slip reactivation initiates). Notice that slip reactivation and back propagation rupture are more apparent from large values of D_r .

8) Preliminary stochastic models of dipping faults with geometrical features of the 1999 Chi-Chi, Taiwan, Earthquake

As continuation of the investigation on asperity models for the 1999 Chi-chi earthquake performed during the last fiscal year (2014), we have initiated the development of generic stochastic models for dipping fault with geometrical features of the 1999 Chi-Chi, Earthquake. Here we show only two samples of these preliminary simulations without further evaluation. Figure 25 and 27 show for two models (s1 and s2) the dynamic parameter distribution, stress drop, critical slip distance (D_c) and strength excess, as well as the rupture solutions represented by final slip, peak slip-velocity rupture time and rupture speed. Contour line on the slip and peak slip-rate are rupture time each 0.5 seconds. These two model, s1 and s2, generates respectively earthquake of magnitude $M_w=7.95$ and 7.93. Stress drop on the first 2km depth are negative, even that the rupture breaks the free-surface resulting in large slip at the shallow zone of about 25m. Peak slip velocity is very large at localized zone of the shallow zone. These high values are apparent because the data has not been filtered in the resolvable frequency range (3Hz). Notice the localized supershear rupture speed along the dip direction of the fault of the hypocentral area for both model, and very low speed along the strike at the shallow zone. Notice that model s1 resembles the slip distribution of the Chi-Chi earthquake, with the largest slip distribution at the northern side.

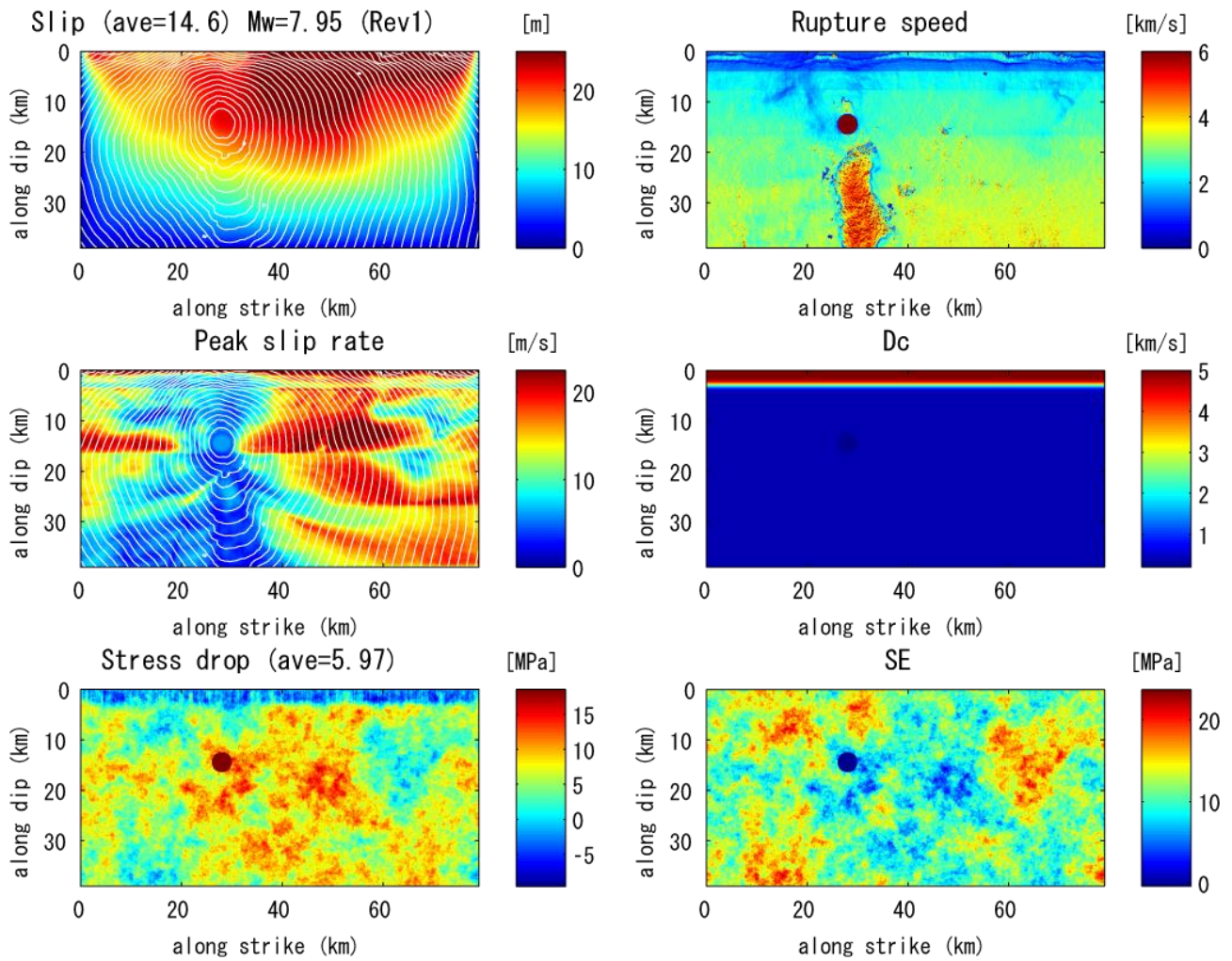


Figure 25. S1 model: dynamic (stress drop, critical slip distance D_c and strength excess SE) and kinematic (slip, peak slip velocity, rupture speed and rupture time) parameters distribution for a dipping fault model with geometrical features of the fault of the 1999 Chi-chi earthquake.

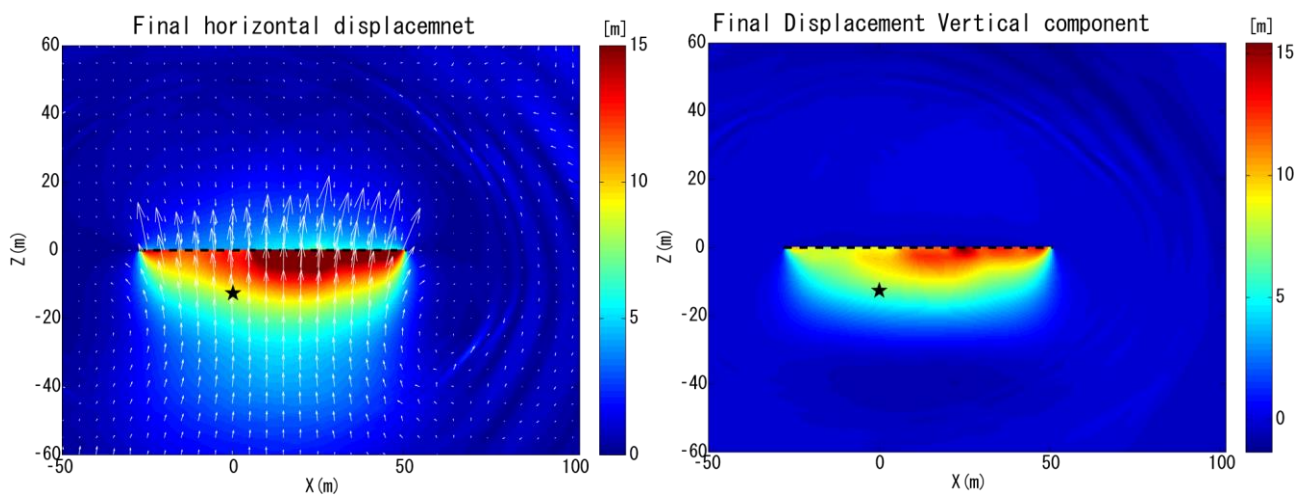


Figure 26. S1 model: Horizontal (left) and vertical (right) final displacement generated by a dipping fault model with geometrical features of the fault of the 1999 Chi-chi earthquake. Arrows indicate the direction of the horizontal slip.

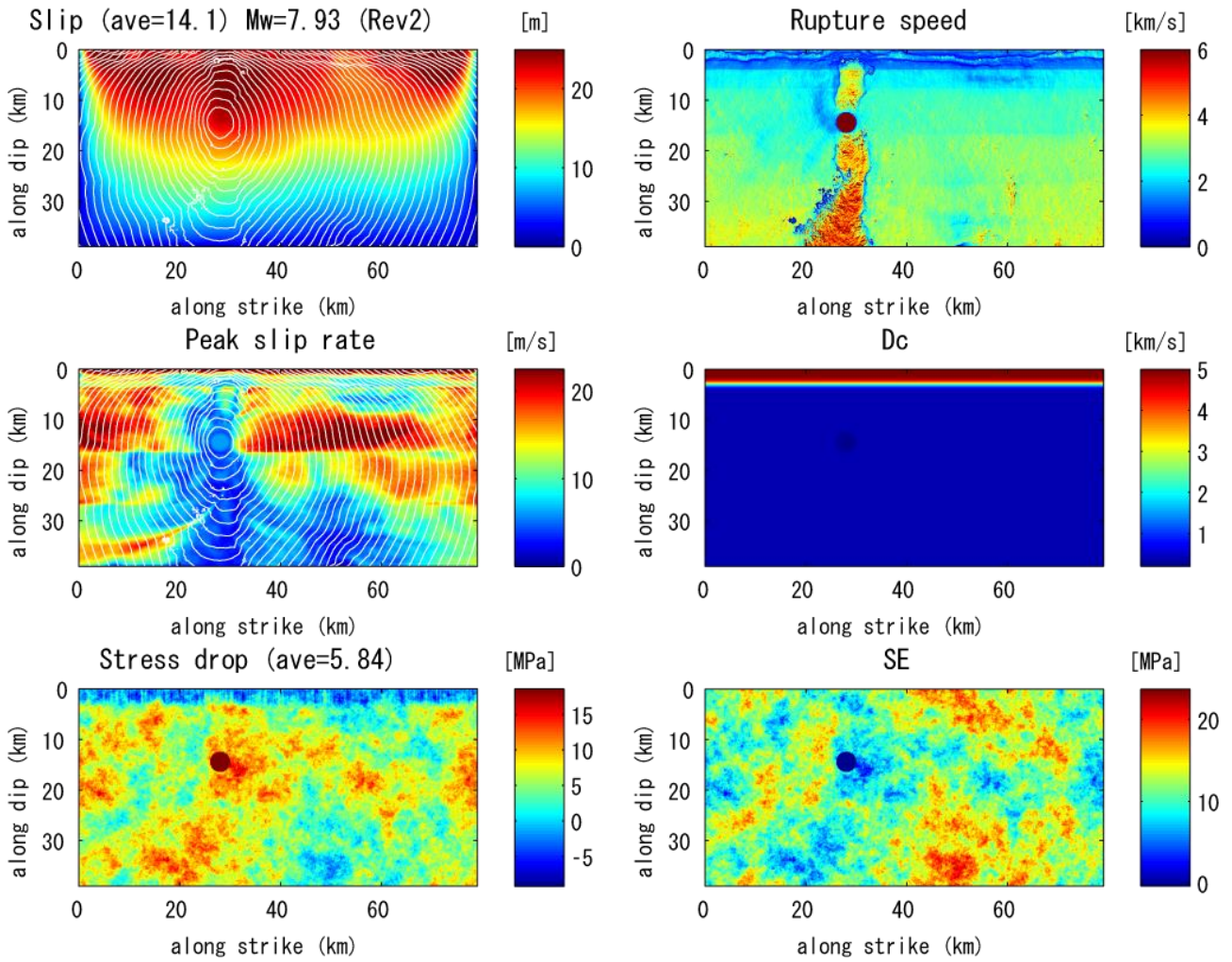


Figure 27, S2 model: dynamic (stress drop, critical slip distance Dc and strength excess SE) and kinematic (slip, peak slip velocity, rupture speed and rupture time) parameters distribution for a dipping fault model with geometrical features of the fault of the 1999 Chi-chi earthquake.

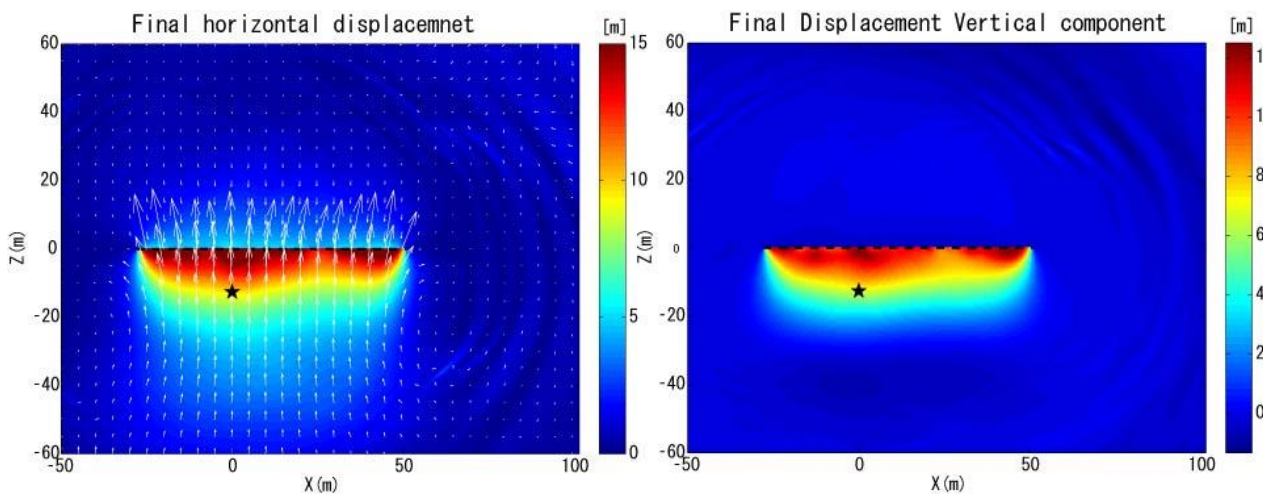


Figure 28. S2 model: Horizontal (left) and vertical (right) final displacement generated by a dipping fault model with geometrical features of the fault of the 1999 Chi-chi earthquake. Arrows indicate the direction of the horizontal slip.

As mentioned before, this simulation results are intended to be only a sample. No further evaluation has been carried out because of short time. We hope next fiscal year we continue with this investigation. In figures 26 and 28 we show the horizontal and vertical final displacement after the last time step of computation for the two models respectively. As seen in these figures there are still wave traveling far from the fault. But near the fault it is expected to be the final displacement. As expected, most of the final displacement (horizontal and vertical) are concentrated at the hanging wall side. Horizontal displacement exhibits rotation with propagation distance along strike, increasing the fault parallel component at the edges of the fault.

Conclusions

Referring to the result of fiscal year 2013, we evaluated permanent displacement from surface-rupturing earthquakes. The problem was tackled by using spontaneous dynamic rupture simulations of asperity models that breaks the free-surface. As a case study we modeled the reverse Mw 7.6 1999 Chi-Chi, Taiwan, earthquake. During this fiscal year (2014), we have planned use stochastic model. For that purpose we have used a database of synthetic earthquake models developed since 2011 by Dr. Dalguer and compile the investigation of this stochastic models developed by the research group of Dr. Dalguer. In addition, we have included in this database couple of preliminary stochastic rupture models with Mw \sim 7.8 parameterized on a fault with geometrical characteristics of the 1999 Chi-Chi Taiwan earthquake, as well as ruptures in strike slip faults exhibiting complexities of slip reactivation and super-shear rupture.

The synthetic data were compared with empirical ground motion prediction equation (GMPEs), in which we show consistency with empirical models up to 1Hz, which means that the residuals (defined as the differences between observed and predicted ground motions) fall in the range of standard deviation of the empirical GMPE. This database reveals features of variability of super-shear rupture speed that depend on earthquake size; ground motion super-saturation near the source, which is different from the saturation features predicted by empirical GMPEs; prediction of acceleration exciding 1g that are evaluated with appropriate recent near-field observations. We found that the effect of source parameters (such as stress drop, peak slip velocity, and rupture speed), surface and buried rupture, directivity as well as hanging wall and footwall are sensitive to ground motion, suggesting that these effects contribute to the variability of ground motion near the source. These findings provide insights on source dominated ground motion features that is not possible to evaluate from real data because of lack of observations.

The work presented in this report on stochastic initial stress distribution for future earthquakes is the initiation of a long-term research project of Dr. Dalguer. We want to build a database of suites of synthetic earthquakes compatible with past earthquakes (in statistical sense) for hazard and risk assessment of future earthquakes in areas where there are not enough observed data. This is particularly of relevant importance near the source where recorded data are sparse and ground motions (displacement, velocity and acceleration) are dominated by the source effects, such as large permanent displacement, strong velocity pulses that impose extreme demands in structures. These near-source ground motion pulses and permanent displacements observed in real earthquakes often contain low frequencies, and appear as coherent that can be simulated with deterministic numerical models. Physics-based dynamic rupture models are the best suitable models to tackle this problem, because they provide physically consistent results that can be used for meaningful prediction of future earthquake ground motion.

For site-specific evaluation for future earthquakes the current empirical GMPEs are insufficient for the prediction in the near-source because these GMPEs are based solely on recorded data which are sparse in the near field, and which do not adequately represent the source and wave propagation effects. Therefore, physics-based numerical models are required if we want to adequately assess the level and variability of near-source ground motion for detail evaluation of seismic hazard, risk

mitigation, earthquake-resistant structural design and seismic safety of future and existing structures, particularly of critical structures such as nuclear power plants.

This long term project is composed by four main phases:

1) Verification:

1.1) Develop suit of synthetic earthquakes, and select earthquakes that are compatible in statistical sense with empirical GMPEs at distance and magnitude in which GMPEs are robust.

1.2) Simulate past earthquakes and verify results with observations.

2) Evaluation of ground motion (permanent displacement, displacement, velocity and acceleration) variability using the synthetic data selected in phase 1.

3) Develop a “hybrid physics-based GMPE” that combines synthetic and observed data.

4) Develop a site-specific hazard assessment using results from phase 2 and 3.

Publications supported by the project for the fiscal year 2014

-Cauzzi C; L.A. Dalguer and C. Baumann (2015), Anatomy of Near-Field Ground-Shaking Generated by Dynamic Rupture Simulations. To be presented in the SSA 2015 meeting, Pasadena.

-Cauzzi C; L.A. and Dalguer (2015), An attempt of synthetic GMPEs from a database of generic stochastic dynamic Rupture models. In preparation.

-Song, S.G. and L.A. Dalguer (2015), Linear Source Inversion with Full Complexity of Earthquake Rupture, including both Supershear Rupture and Slip Reactivation. In preparation

Acknowledgment

We thanks to Dr. Hao WU for his great support and valuable help making some figures and running simulations corresponding to the dipping fault model with geometrical characteristics of the 1999 Chi-chi earthquake, as well for all his dedicated technical work testing the computing resources of the Foundation for Computational Science of Japan. We also thanks Prof. Susumu Kurahashi and Prof. Kojiro Irikura for advising Dr. Hao Wu and logistic support.

References:

- Akkar, S., and J. J. Bommer (2007a). Empirical prediction equations for peak ground velocity derived from strong-motion records from Europe and the Middle East, *Bull. Seismol. Soc. Am.* 97, no. 2, 511–530, doi: 10.1785/0120060141.
- Akkar, S., and J. J. Bommer (2007b). Prediction of elastic displacement response spectra in Europe and the Middle East, *Earthq. Eng. Struct. Dynam.* 36, 1275–1301.
- Akkar, S., and J. J. Bommer (2010). Empirical equations for the prediction of PGA, PGV, and spectral accelerations in Europe, the Mediterranean region, and the Middle East, *Seismol. Res. Lett.* 81, no. 2, 195–206.
- Akkar et al., 2014.
- Andrews, D.J (1976). Rupture velocity of plane-strain shear cracks, *J. Geophys. Res.*, 81, 5679-5687.
- Aoi, S.; T. Kunugi and H. Fujiwara (2008). Trampoline Effect in Extreme Ground Motion, *Science* 322, 727, DOI: 10.1126/science.1163113.
- Archuleta, R. J. (1984). A faulting model for the 1979 Imperial Valley earthquake, *J. Geophys. Res.* 89, no. B6, 4559–4585.

- Baumann C. and L.A. Dalguer (2014), Evaluating the Compatibility of Dynamic-Rupture-Based Synthetic Ground Motion with Empirical GMPE. *Bull. Seismol. Soc. Am.* 104(2), April 2014, doi: 10.1785/0120130077.
- Berryman, K. (2011), A tale of two earthquakes – the Christchurch sequence of 2010-2011, proc. G-Event Conference, Tsukuba, March 2011.
- Bizzarri, A., and P. Spudich (2008). Effects of super-shear rupture speed on the high frequency content of S-waves investigated using spontaneous dynamic rupture models and isochrone theory, *J. Geophys. Res.* 113, doi 10.1029/2007JB005146.
- Boore, D. M., and G. M. Atkinson (2008). Ground-motion prediction equations for the average horizontal component of PGA, PGV, and 5%-damped PSA at spectral periods between 0.01 s and 10.0 s, *Earthq. Spectra* 24, no. 1, 99–138.
- Borcherdt, R. D. (1994). Estimates of site-dependent response spectra for design (methodology and justification), *Earthq. Spectra* 10, no. 4, 617–653.
- Borcherdt, R. D. (2002). Empirical evidence for acceleration-dependent amplification factors, *Bull. Seismol. Soc. Am.* 92, no. 2, 761–782.
- Brune, J. N., and A. Anooshehpour (1998). A physical model of the effect of a shallow weak layer on strong ground motion for strike-slip ruptures, *Bull. Seismol. Soc. Am.* 88, 1070–1078.
- Cauzzi C, Faccioli E (2008) Broadband (0.05 to 20 s) prediction of displacement response spectra based on worldwide digital records. *J Seismol* 12:453–475. doi: 10.1007/s10950-008-9098-y
- Cauzzi C, Faccioli E, Vanini M, Bianchini A (2014) Updated predictive equations for broadband (0.01–10 s) horizontal response spectra and peak ground motions, based on a global dataset of digital acceleration records. *Bull Earthq Eng.* doi: 10.1007/s10518-014-9685-y.
- Dalguer L.A; Irikura K; Riera J. And Chiu H.C (2001). The Importance of the Dynamic Source Effects on Strong Ground Motion During the 1999 Chi-Chi (Taiwan) Earthquake: Brief Interpretation of the Damage Distribution on Buildings. *Bull. Seismol. Soc. Am.*, 95, 1112-1127.
- Dalguer, L. A. and Day, S. M. (2006), Comparison of Fault Representation Methods in Finite Difference Simulations of Dynamic Rupture. *Bull. Seismol. Soc. Am.*, 96, 1764 - 1778.
- Dalguer, L. A. and Day, S. M. (2007), Staggered-Grid Split-Nodes Method for Spontaneous Rupture Simulation. *J. Geophys. Res.*, 112, B02302, doi:10.1029/2006JB004467.
- Dalguer, L.A., H. Miyake, S.M. Day and K. Irikura (2008), Surface Rupturing and Buried Dynamic Rupture Models Calibrated with Statistical Observations of Past Earthquakes. *Bull. Seismol. Soc. Am.* 98, 1147-1161, doi: 10.1785/0120070134.
- Dalguer, L.A. and M. Mai (2008), Implications of Style-of-Faulting and Loading Characteristics on the Dynamic Rupture Process, *Eos Trans. AGU*, 89(53), Fall Meet. Suppl., Abstract S51D-1798.
- Dalguer, L.A. and P.M. Mai (2012), Prediction of near-source ground motion exceeding 1g at low frequencies (<2Hz) from Mw~6.5 deterministic physics-based dynamic rupture simulations, *Proceedings of the 15th World Conference on Earthquake Engineering (15WCEE)*, Lisbon, Portugal, September 24-28, 2012.
- Das, S., and K. Aki (1977). Fault planes with barriers: Aversatile earthquake model, *J. Geophys. Res.* 82, 5648–5670.
- Day, S. M. (1982a). Three-dimensional finite difference simulation of fault dynamics: rectangular faults with fixed rupture velocity, *Bull. Seismol. Soc. Am.*, 72, 705-727.
- Day, S. M. (1982b). Three-dimensional simulation of spontaneous rupture: the effect of nonuniform prestress, *Bull. Seismol. Soc. Am.*, 72, 1881-1902.
- Day, S. M., and G. P. Ely (2002). Effect of a shallow weak zone on fault rupture: Numerical simulation of scale-model experiments, *Bull. Seismol. Soc. Am.* 92, 3006–3021.
- Day, S. M., L.A. Dalguer, N. Lapusta, and Y. Liu (2005). Comparison of finite difference and boundary integral solutions to three-dimensional spontaneous rupture, *J. Geophys. Res.*, 110,

B12307, doi:10.1029/2005JB003813.

- Day, S. M., S. H. Gonzalez, R. Anoushehpour, and J. N. Brune (2008). Scale-model and numerical simulations of near-fault seismic directivity, *Bull. Seism. Soc. Am.*, Vol. 98, doi: 10.1785/0120070190, pp. 1186-1206
- Dunham, E. M., and R. J. Archuleta (2005). Near-source ground motion from steady state dynamic rupture pulses, *Geophys. Res. Lett.* 32, L03302, doi: 10.1029/2004GL021793.
- Dunham, E. M. (2007). Conditions governing the occurrence of supershear ruptures under slip-weakening friction, *J. Geophys. Res.* 112, (B07302), doi 10.1029/2006JB004717.
- Dunham, E. M., and H. S. Bhat (2008). Attenuation of radiated ground motion and stresses from three-dimensional supershear ruptures, *J. Geophys. Res.* 113, no. B08319, doi: 10.1029/2007JB005182.
- Ely, G. P., S. M. Day and J.-B. Minster (2008). A support-operator method for viscoelastic wave modelling in 3-D heterogeneous media, *Geophysical Journal International*, 172(1) 331-344.
- Ely, G., S. M. Day and J-B. Minster (2009). A support-operator method for 3D rupture dynamics, *Geophysical Journal International*, 177 1140-1150, DOI: 10.1111/j.1365 246X.2009.04117.x.
- Gabriel, A. A.; J. P. Ampuero; L. A. Dalguer and P. M. Mai (2012), The Transition of Dynamic Rupture Styles in Elastic Media Under Velocity-Weakening Friction. *J. Geophys. Res.*, 117, B09311, doi:10.1029/2012JB009468.
- Graizer, V., and E. Kalkan (2007). Ground motion attenuation model for peak horizontal acceleration from shallow crustal earthquakes, *Earthq. Spectra* 25, no. 3, 585–613.
- Graizer, V., and E. Kalkan (2011). Modular filter-based approach to ground motion attenuation modeling, *Seismol. Res. Lett.* 82, no. 1, 21–31, doi: 10.1785/gssrl.82.1.21.
- Graizer V, Kalkan E, Lin K-W (2013) “Global Ground Motion Prediction Equation for Shallow Crustal Regions”, *Earthquake Spectra*, 29(3), 777–791
- Harris, R. A., M. Barall, R. Archuleta, E. M. Dunham, B. Aagaard, J. P. Ampuero, H. Bhat, V. Cruz-Atienza, L. Dalguer, P. Dawson, S. Day, B. Duan, G. Ely, Y. Kaneko, Y. Kase, N. Lapusta, Y. Liu, S. Ma, D. Oglesby, K. Olsen, A. Pitarka, S. Song, and E. Templeton (2009), The SCEC/USGS dynamic earthquake-rupture code verification exercise, *Seismological Research Letters*, 80(1), 119-126, doi:10.1785/gssrl.80.1.119.
- Lee, S.-J., Huang, B.-S., Ando, M., Chiu, H.-C., & Wang, J.-H., 2011. Evidence of large scale repeating slip during the 2011 Tohoku-Oki earthquake, *Geophysical Research Letters*, 38(19), L19306.
- Mai, P. M., and G. C. Beroza (2002). A spatial random-field model to characterize complexity in earthquake slip, *J. Geophys. Res.* 107, no. B11, 2308, doi 10.1029/2001JB000588.
- Marone, C. (1998). Laboratory-derived friction laws and their application to seismic faulting, *Ann. Revs. Earth Plan. Sci.* 26, 643–696.
- Marone, C., and C. H. Scholz (1988). The depth of seismic faulting and the upper transition from stable to unstable slip regimes, *Geophys. Res. Lett.* 15, 621–624.
- Mena, B.; L.A. Dalguer and P.M. Mai (2012), Pseudodynamic Source Characterization For Strike-Slip Faulting, Including Stress Heterogeneity and Super-shear Ruptures, *Bull. Seismol. Soc. Am.*, 102(4), pp. 1654–1680, August 2012, doi: 10.1785/0120110111.
- Oglesby, D. D., R. J. Archuleta, and S. B. Nielsen (1998). Earthquakes on dipping faults: the effects of broken symmetry, *Science* 280, 1055–1059.
- Olsen, K., S.M. Day, L.A. Dalguer, J. Mayhew, Y. Cui, J. Zhu, V.M. Cruz-Atienza, D. Roten, P. Maechling, T.H. Jordan, D. Okaya and A. Chourasia (2009) ShakeOut-D: Ground motion estimates using an ensemble of large earthquakes on the southern San Andreas fault with spontaneous rupture propagation, *Geophys. Res. Lett.*, 36, L04303, doi:10.1029/2008GL036832.
- Olsen, K. B., R. Madariaga, and R. Archuleta (1997). Three dimensional dynamic simulation of the 1992 Landers earthquake, *Science* 278, 834–838.

- Ripperger, J., J. P. Ampuero, P. M. Mai, and D. Giardini (2007). Earthquake source characteristics from dynamic rupture with constrained stochastic fault stress, *J. Geophys. Res.* 112, B04311, doi 10.1029/2006JB004515.
- Shashkov, M. (1996). *Conservative Finite-Difference Methods on general grids*, CRC Press, Boca Raton, FL.
- Sibson, R.H. (1991). Loading of Faults to failure, *Bull. Seismol. Soc. Am.* 81, 2493–2497.
- Song, S.G. and L.A. Dalguer (2015), *Linear Source Inversion with Full Complexity of Earthquake Rupture, including both Supershear Rupture and Slip Reactivation*. In preparation.
- Spudich, P., and E. Cranswick (1984). Direct observation of rupture propagation during the 1979 Imperial Valley earthquake using a short baseline accelerometer array, *Bull. Seismol. Soc. Am.* 74, 2083–2114.
- Strasser, F. O., N. A. Abrahamson, and J. J. Bommer (2009). Sigma: Issues, insights, and challenges, *Seismol. Res. Lett.* 80, no. 1, 40–56.
- Yamada, M; J. Mori and T. Heaton (2009). The Slapdown Phase in High-acceleration Records of Large Earthquakes, *Seismol. Res. Lett.* 80, no. 4, doi: 10.1785/gssrl.80.4.559.

APPENDIX: Comparison between observation and synthetic of velocity and displacement ground motion at 39 stations near the Chelongpu fault of the 1999 Chi-Chi, Taiwan, earthquake.

The figures below are part of the last fiscal year (2013) project in which we have developed asperity dynamic rupture models for the 1999 Chi-Chi, Taiwan, Earthquake. Seismograms passed a low pass filter with frequency cut off of 0.5Hz. In all the figures, left column are velocity and right column displacement of three components (EW, NS and UD). In general synthetic follow the general pattern of observation. Observed velocity and displacement has been obtained respectively by integration and double integration from recorded acceleration. The recorded accelerations were corrected by this project using quadratic fit to velocity following Boore et al. (2002).

Some observed velocity and displacements follow rare patterns: TCU071 (Fig. A.15), TCU079 (Fig. A.21), TCU084 (Fig. A.22), CHY028 (Fig. A.35). The corrected accelerations in these stations need to be verified.

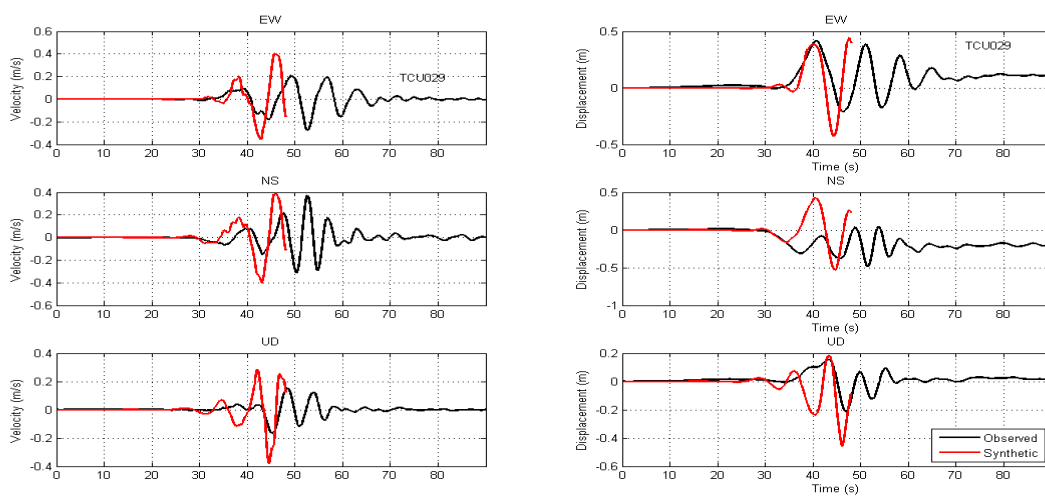


Figure A.1. Station TCU029

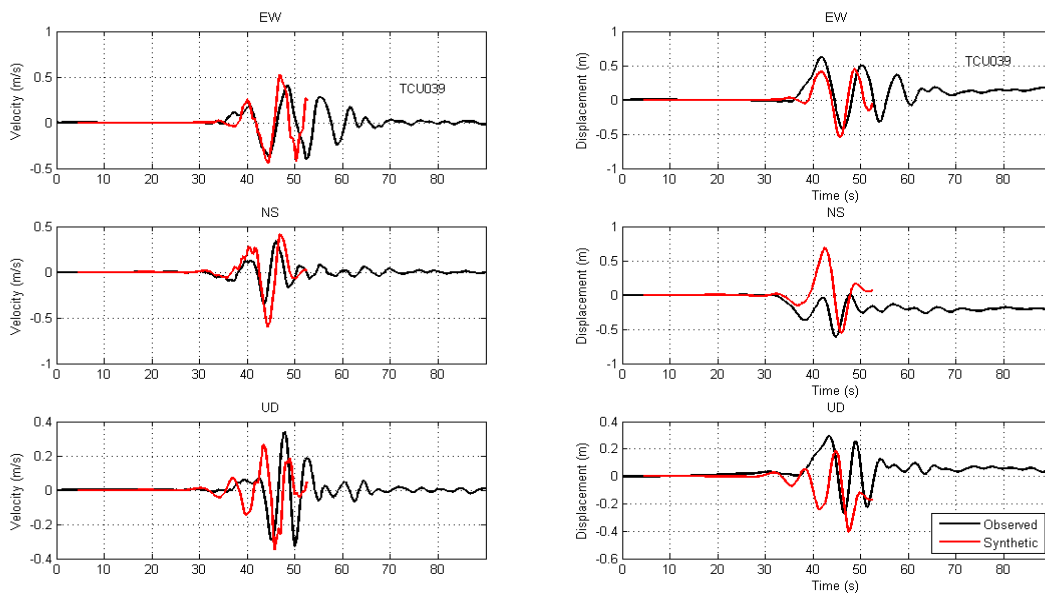


Figure A.2. Station TCU39

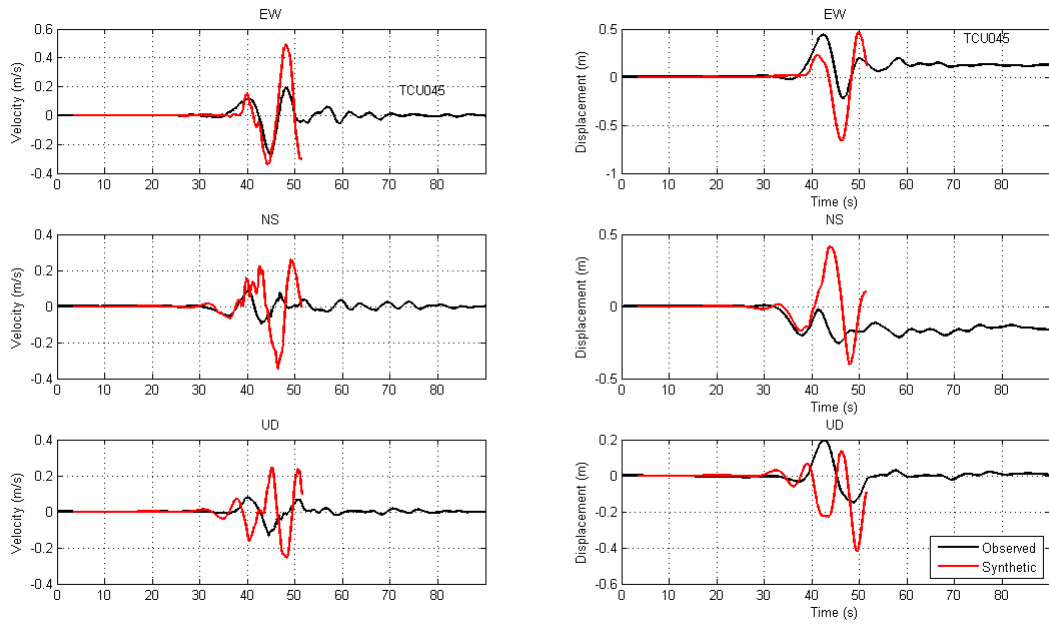


Figure A.3. Station TCU045

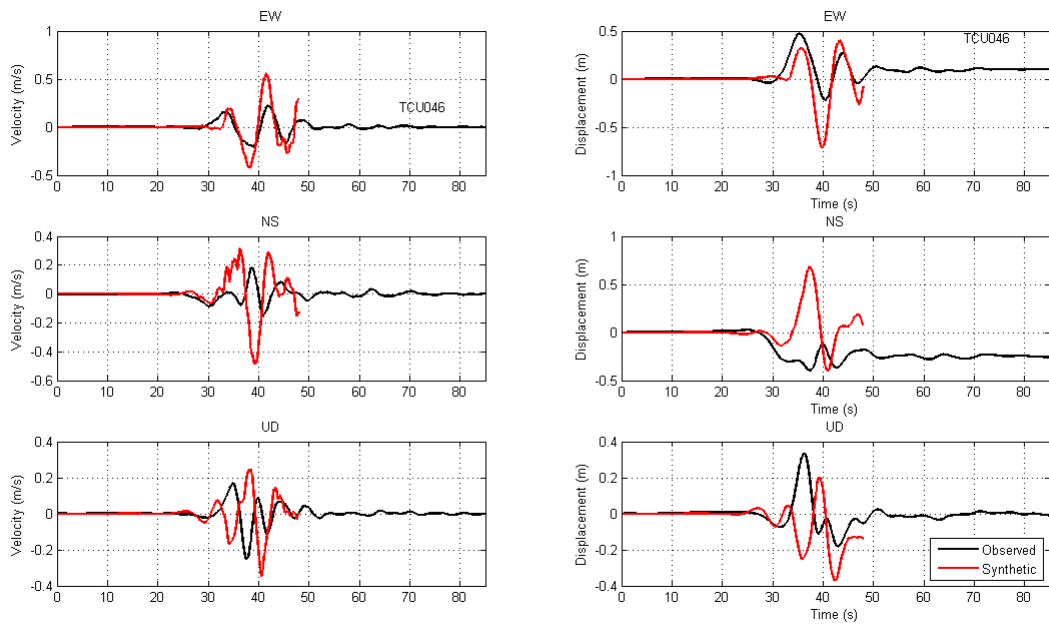


Figure A.4. Station TCU046

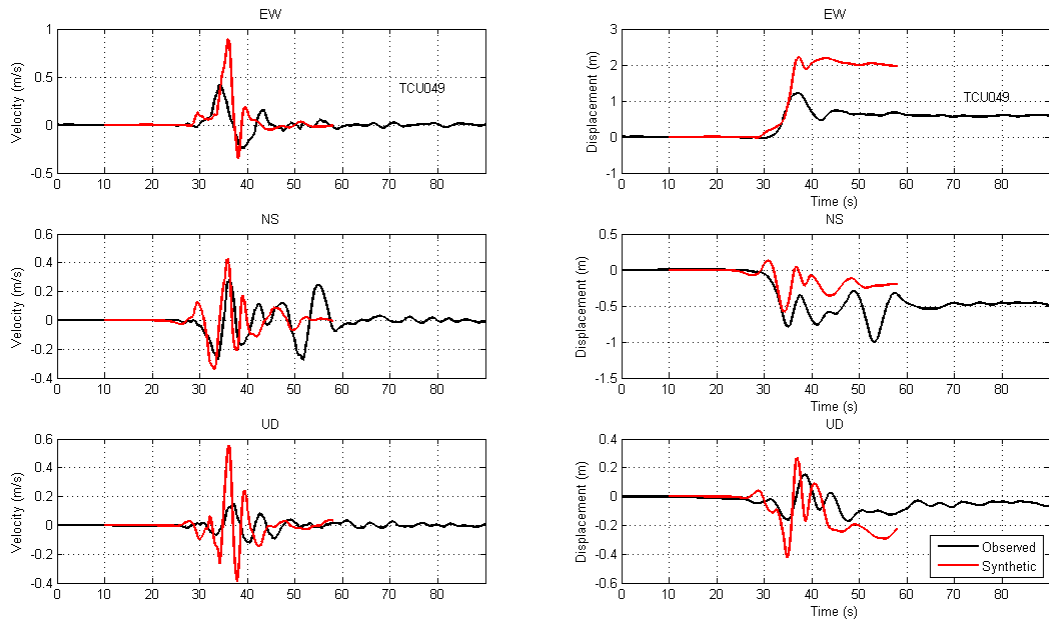


Figure A.5. Station TCU049

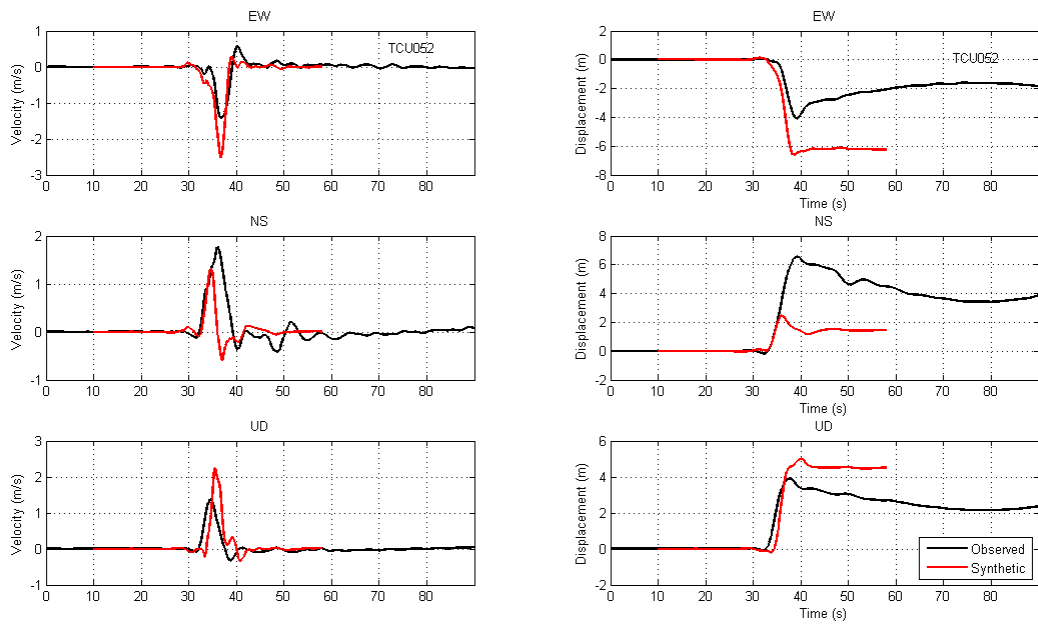


Figure A.6. Station TCU52

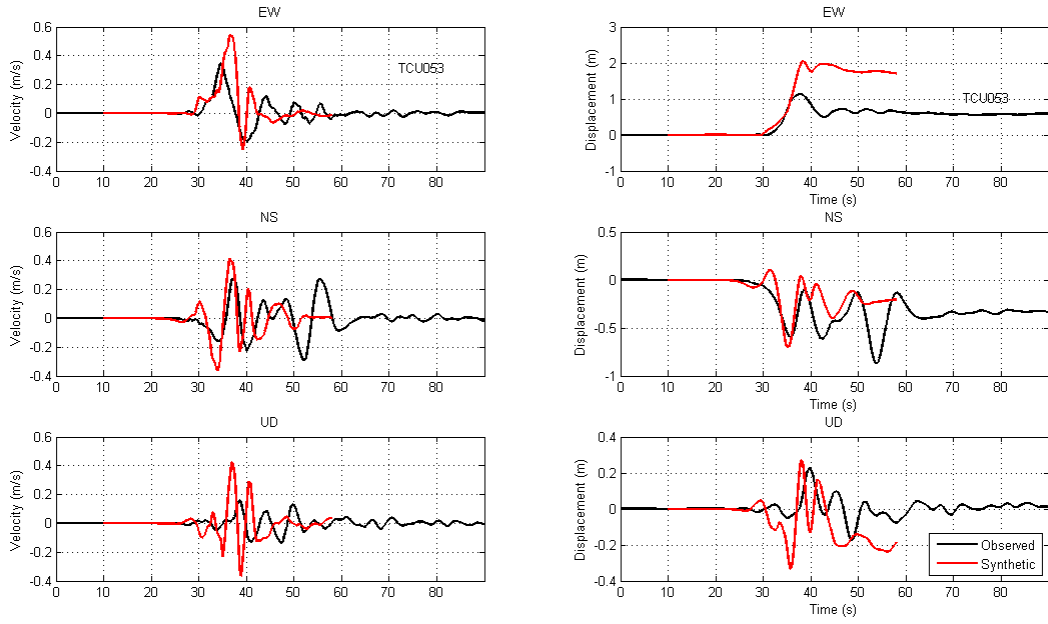


Figure A.7. Station TCU053

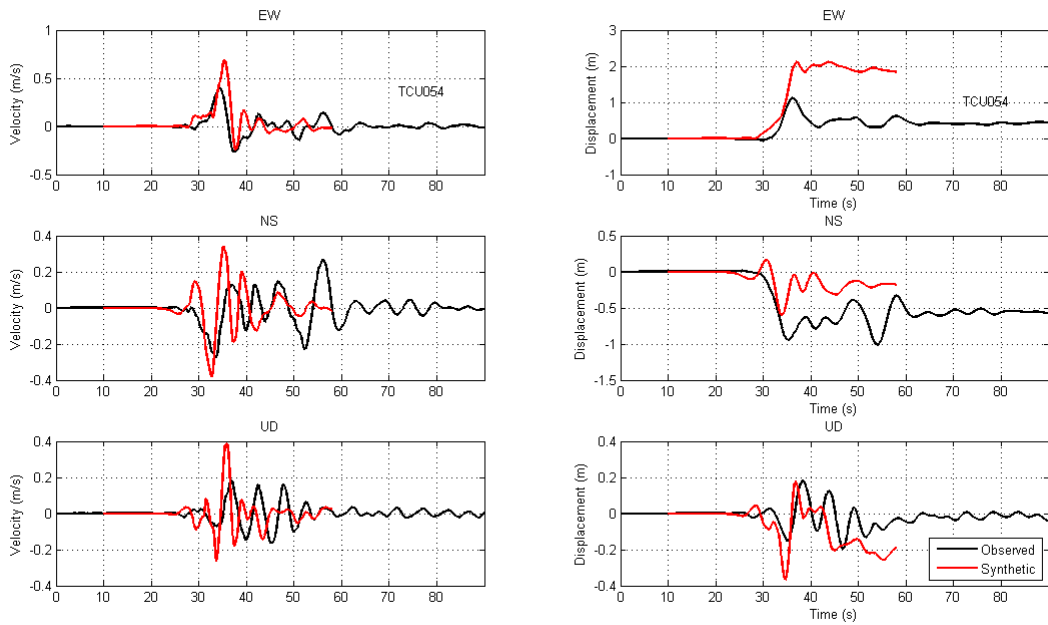


Figure A.8. Station TCU054

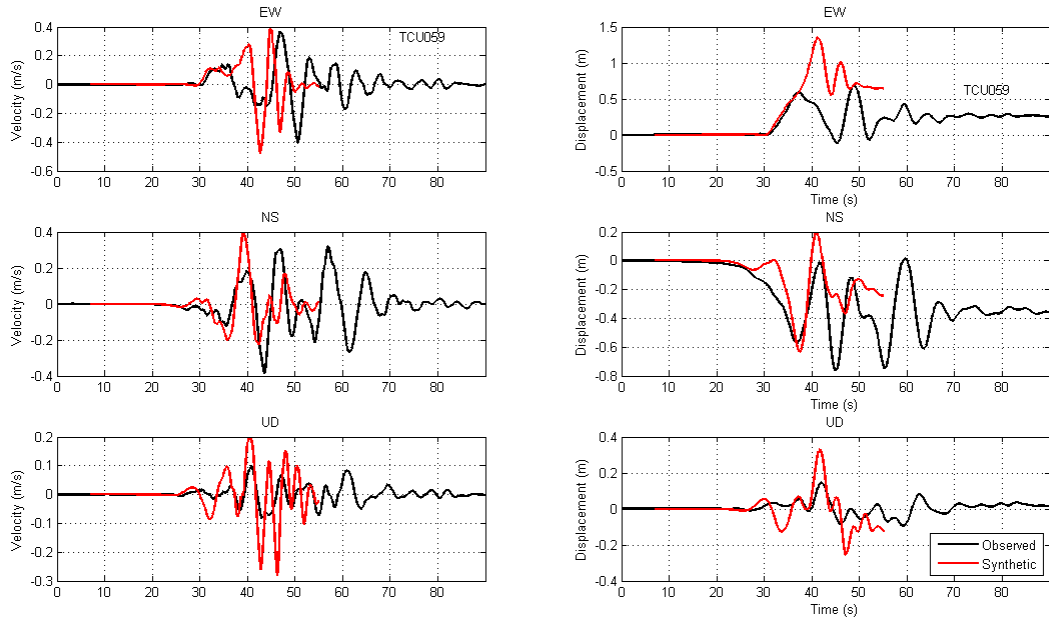


Figure A.9. Station TCU059

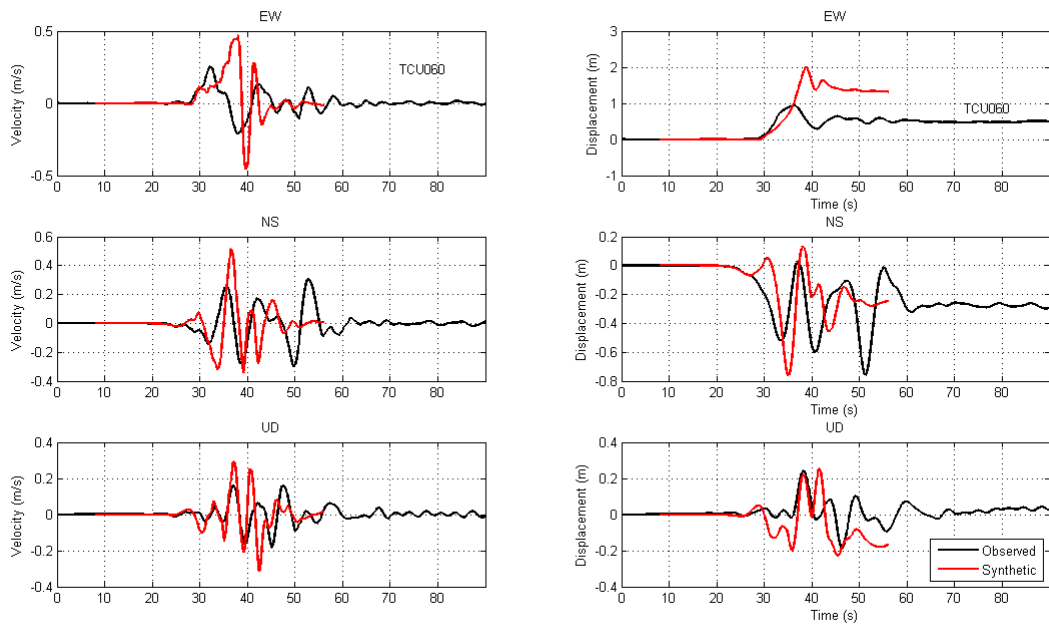


Figure A.10. Station TCU060

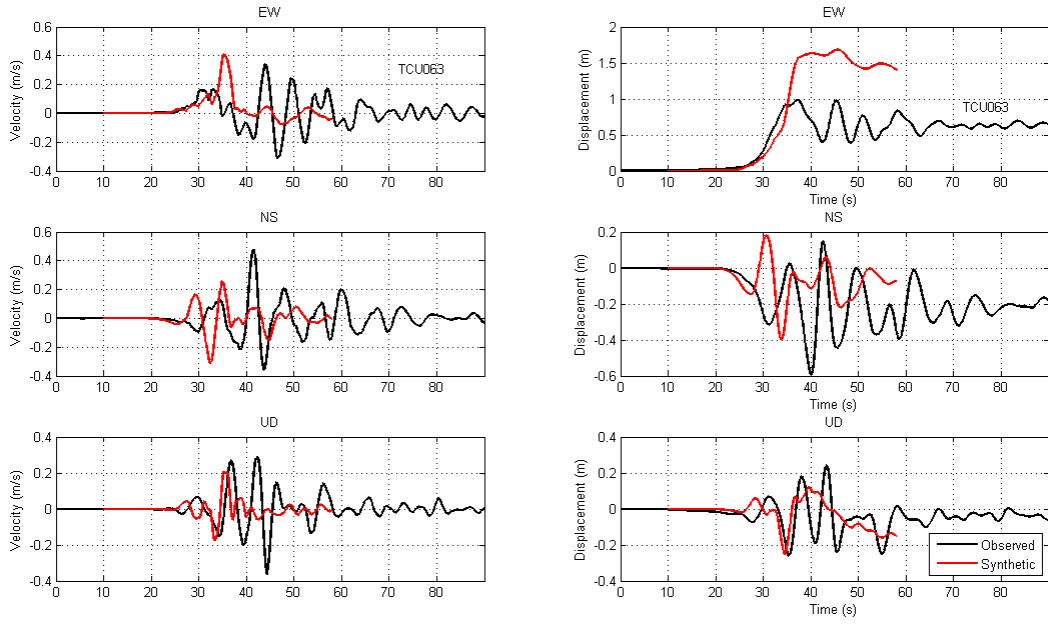


Figure A.11. Station TCU063

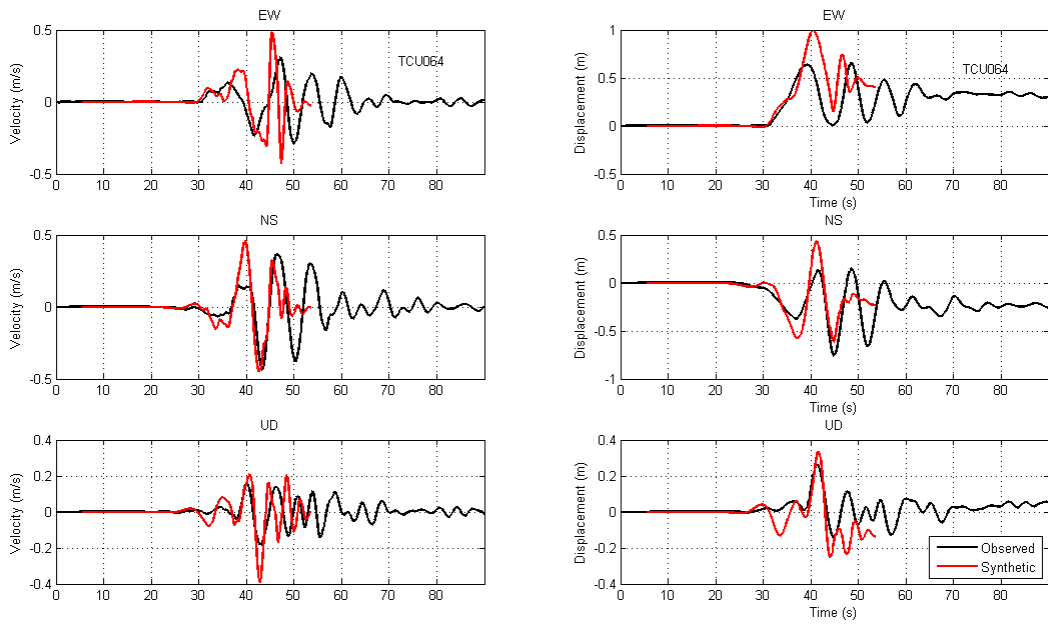


Figure A.12. Station TCU064

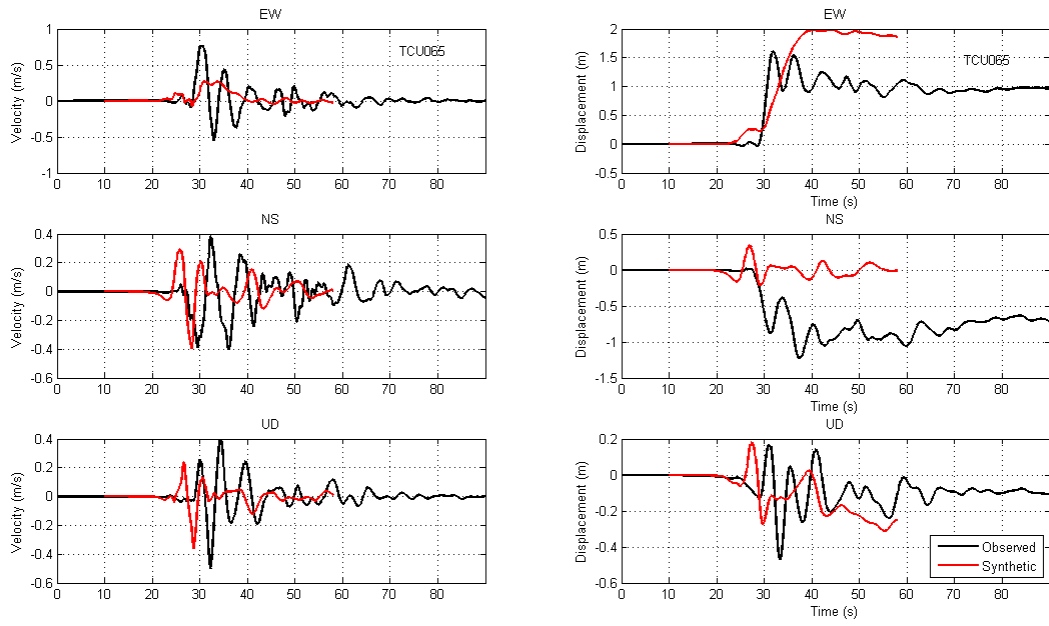


Figure A.13. Station TCU065

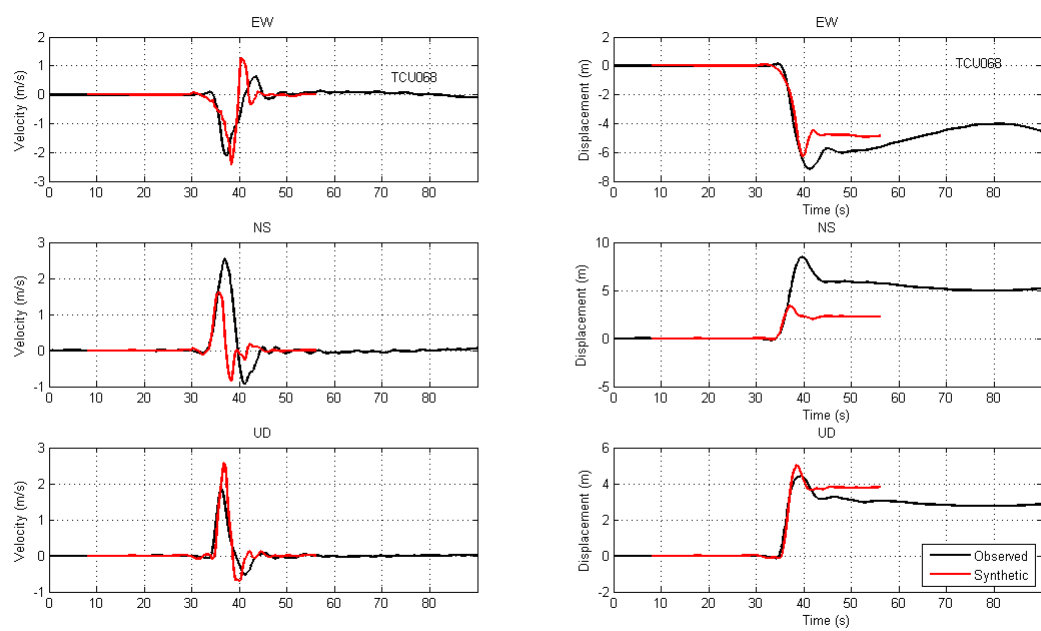


Figure A.14. Station TCU068

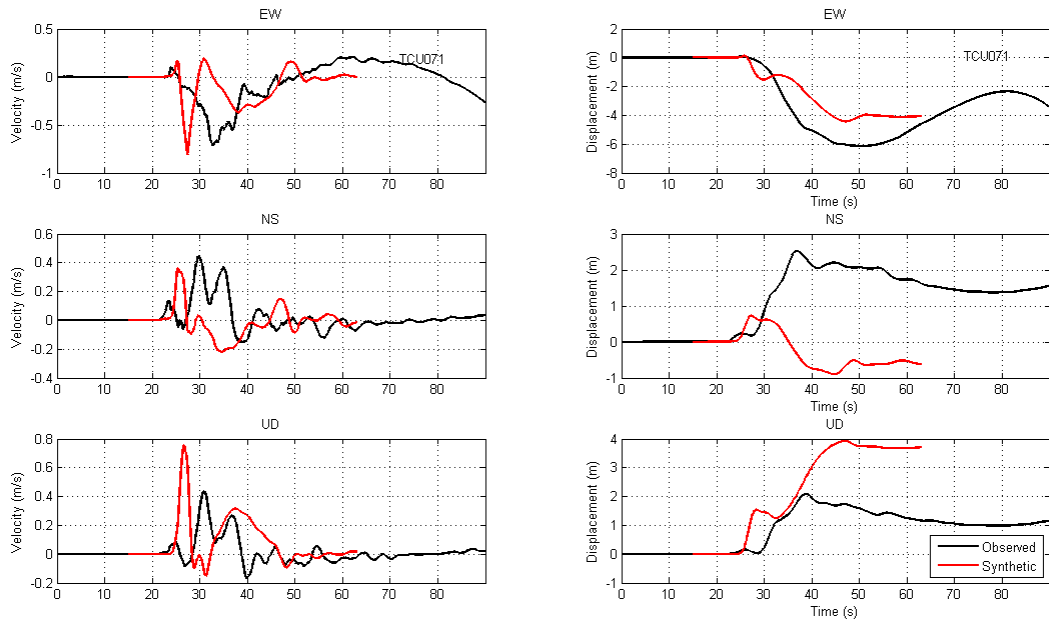


Figure A.15. Station TCU071

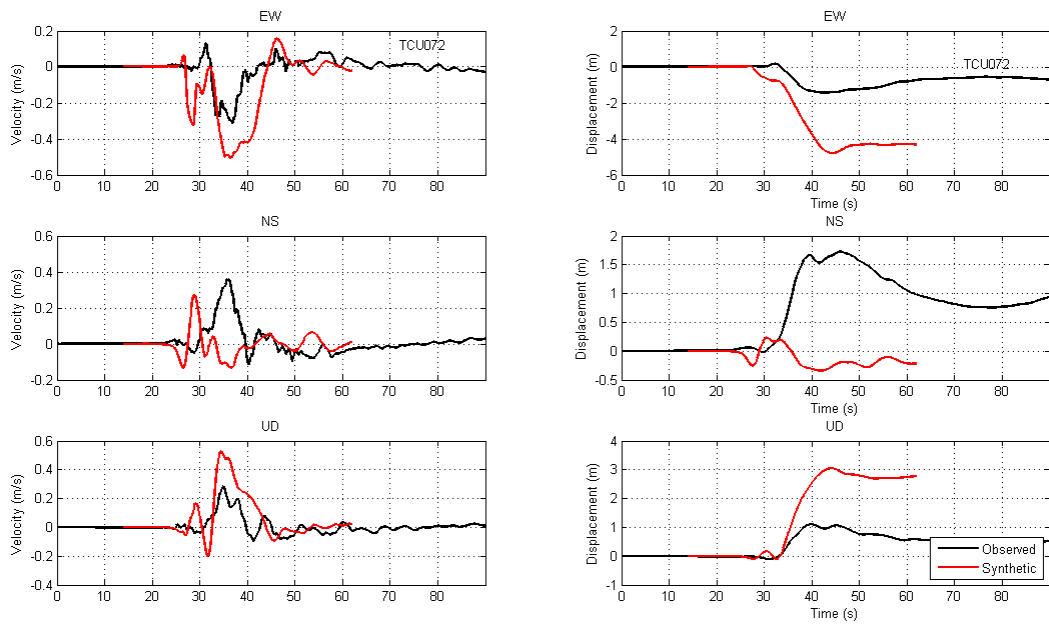


Figure A.16. Station TCU072

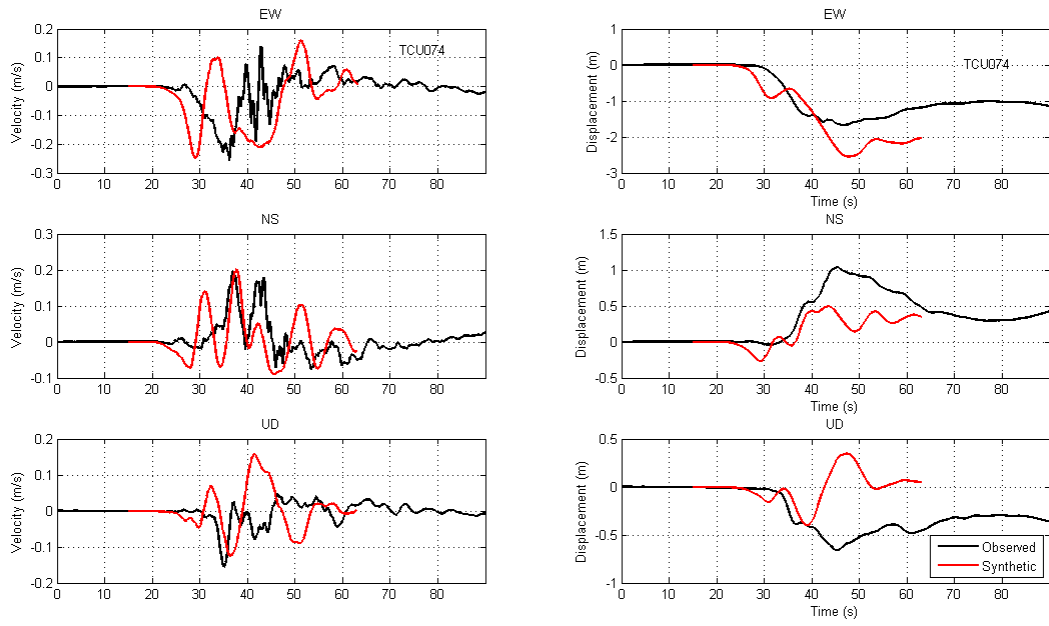


Figure A.17. Station TCU074

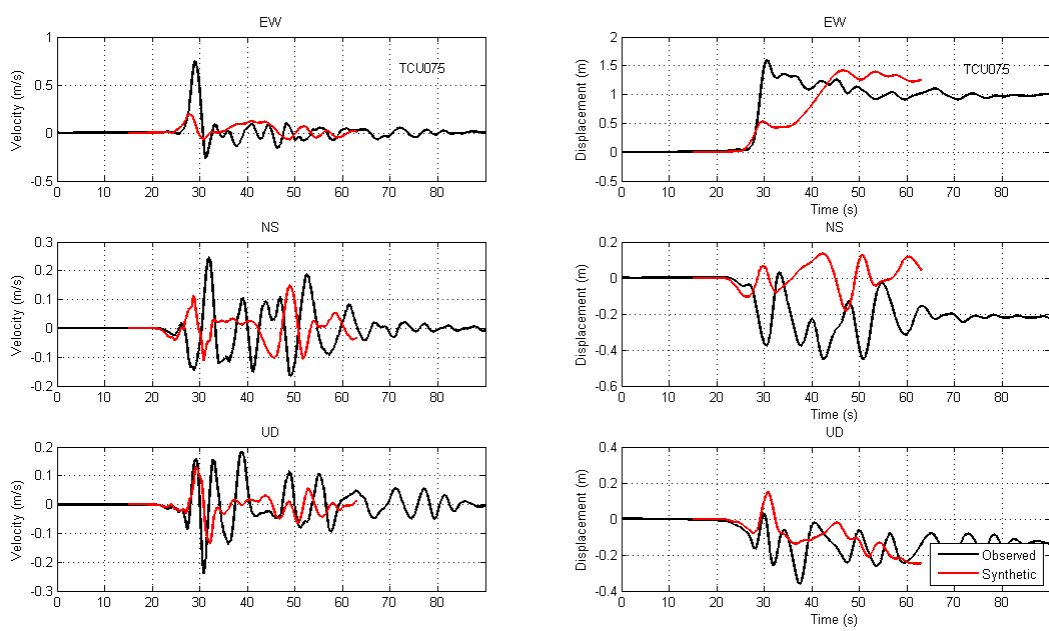


Figure A.18. Station TCU075

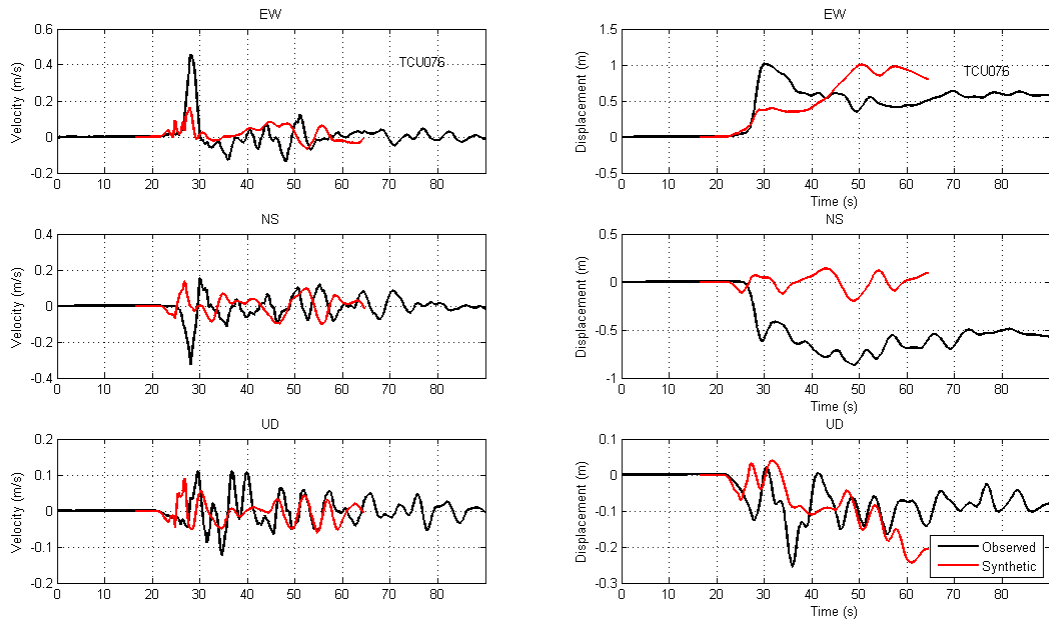


Figure A.19. Station TCU076

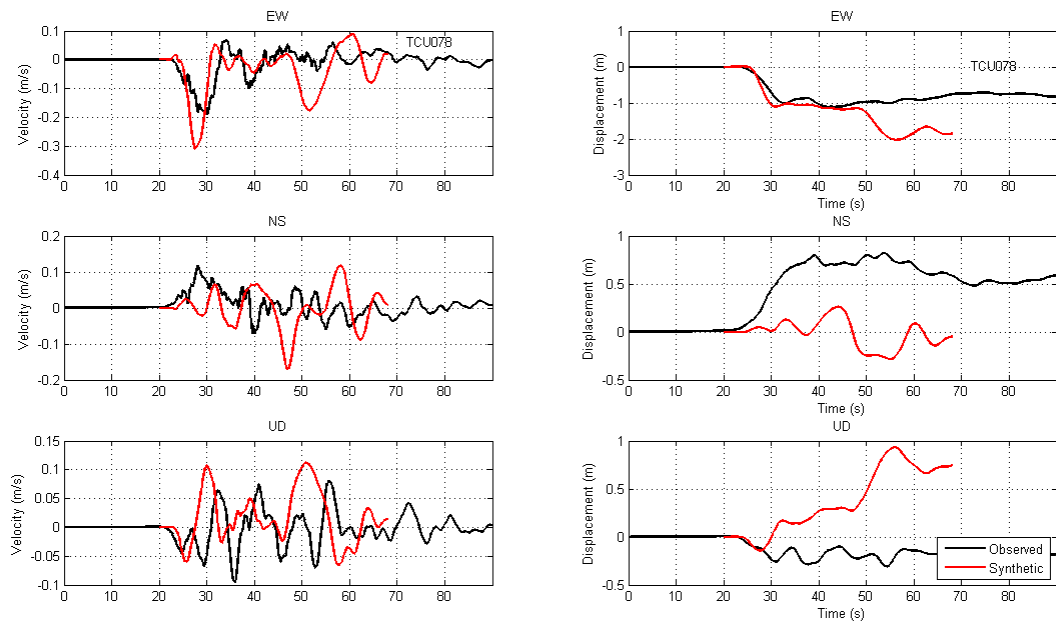


Figure A.20. Station TCU078

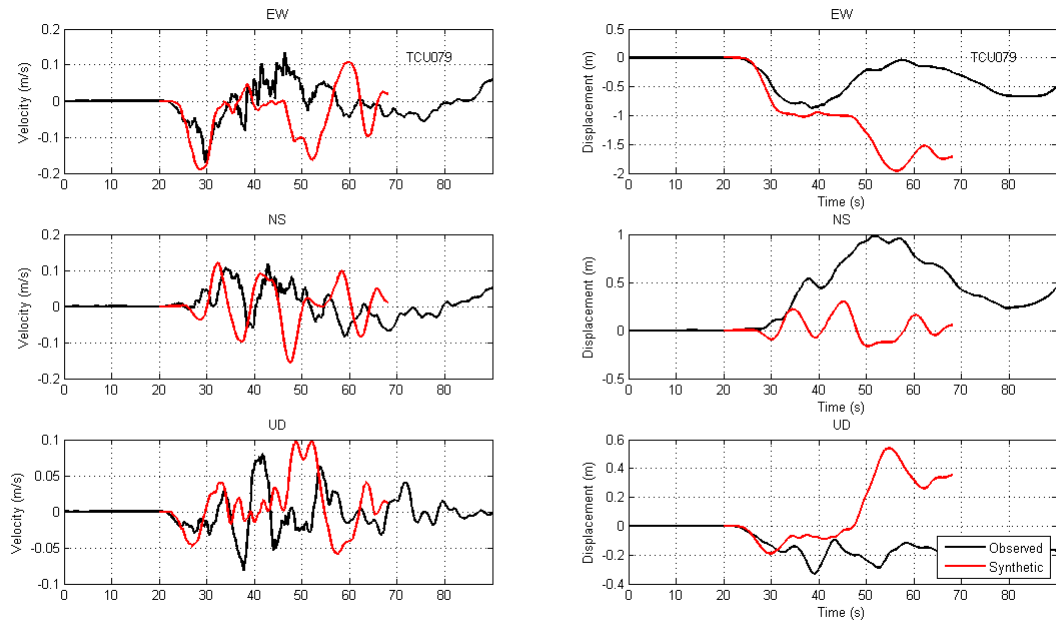


Figure A.21. Station TCU079

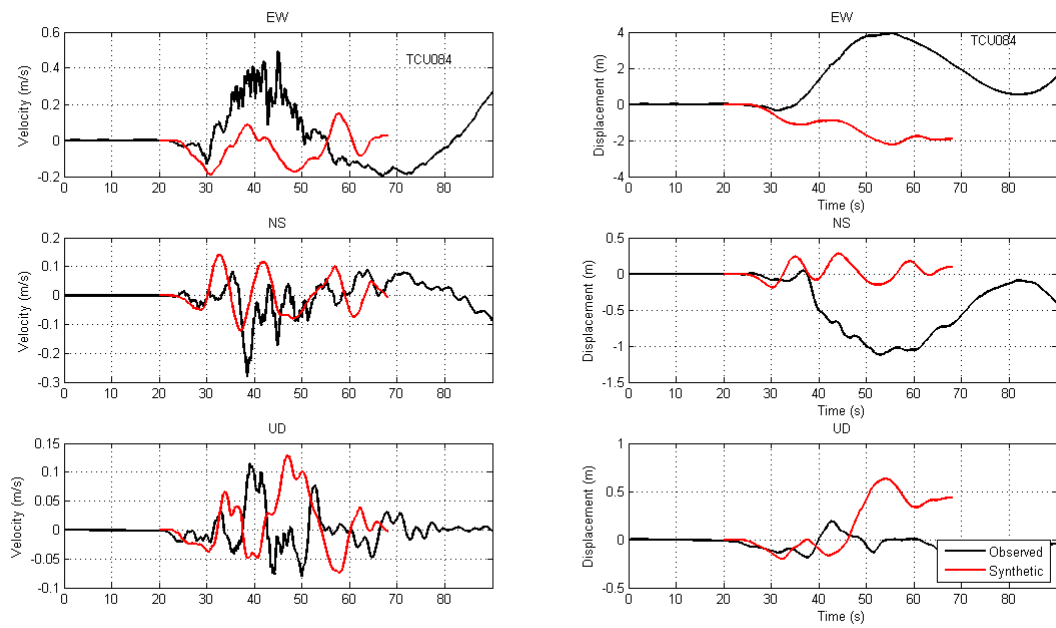


Figure A.22. Station TCU084

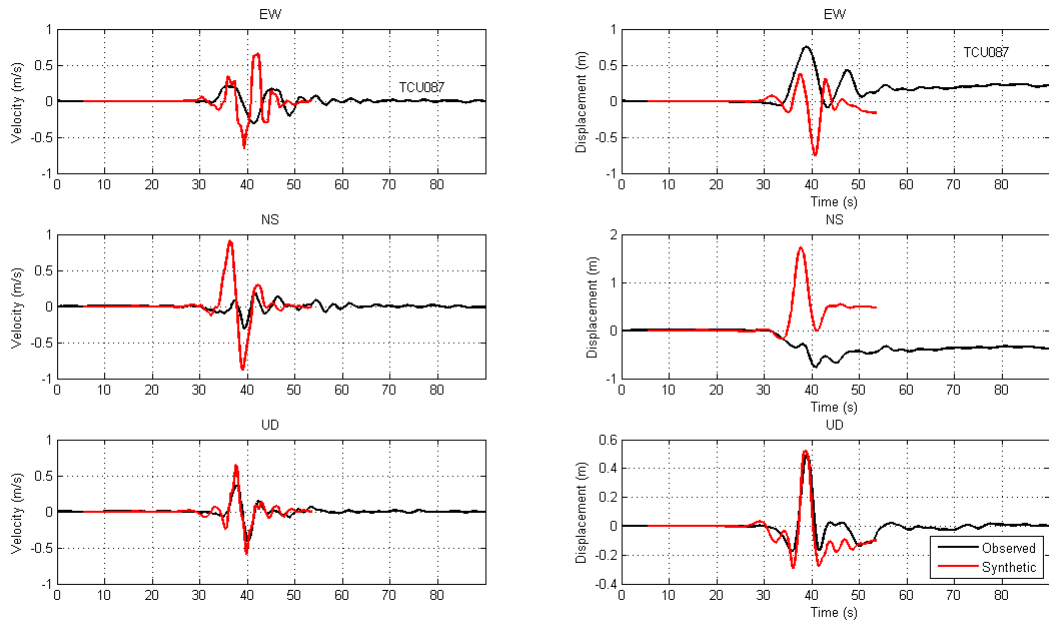


Figure A.23. Station TCU087

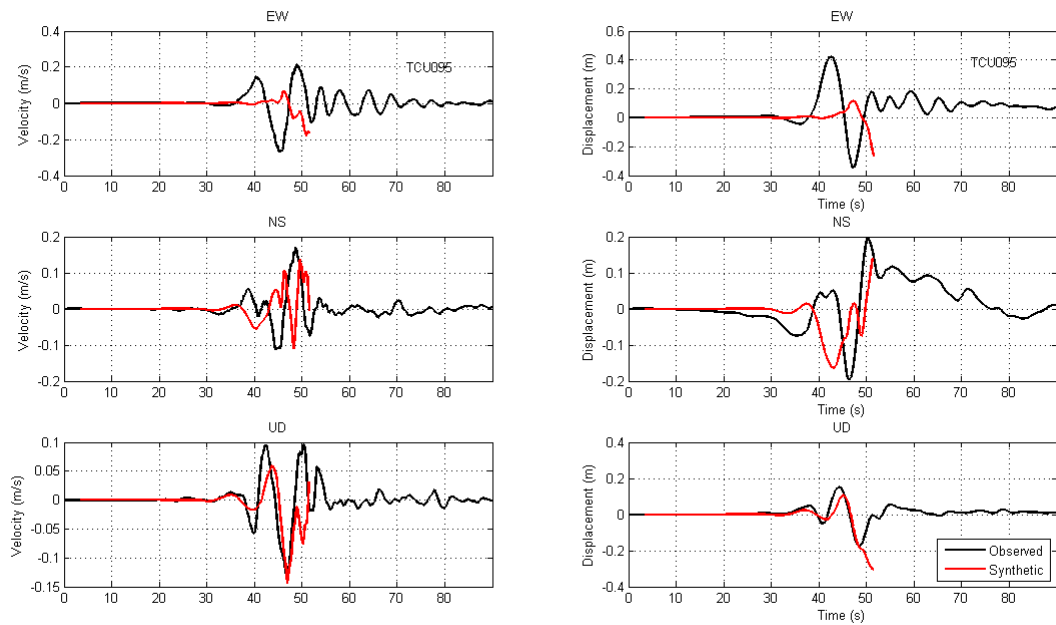


Figure A.24. Station TCU095

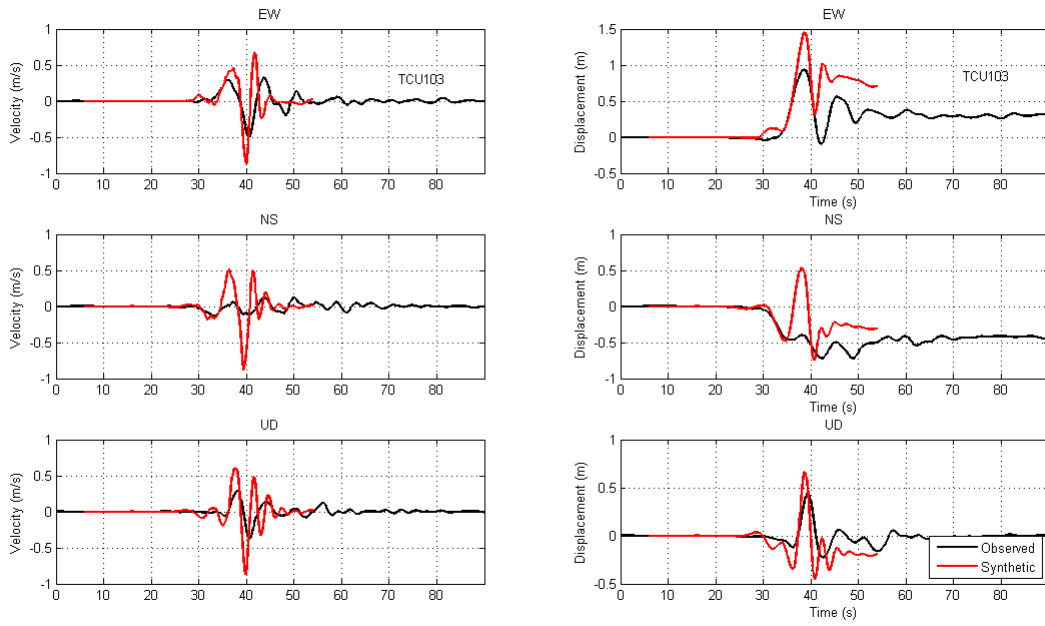


Figure A.25. Station TCU103

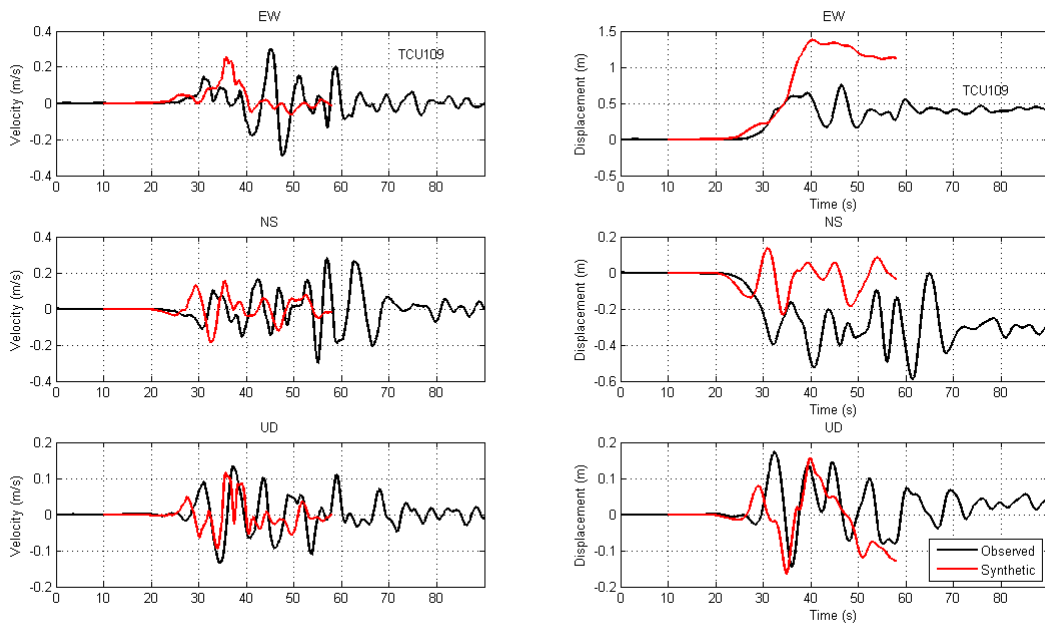


Figure A.26. Station TCU109

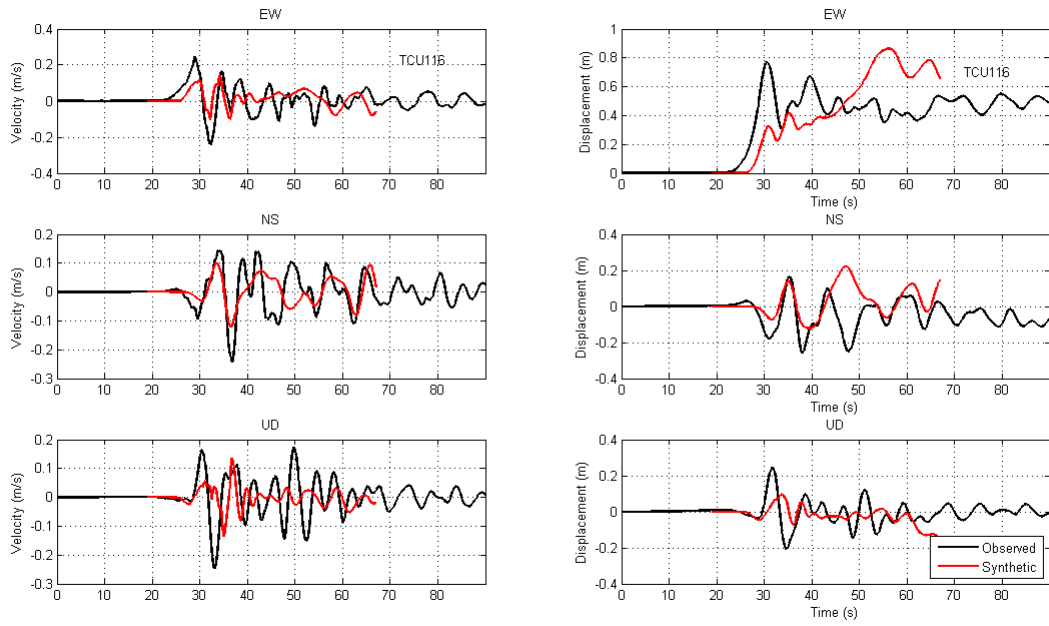


Figure A.27. Station TCU116

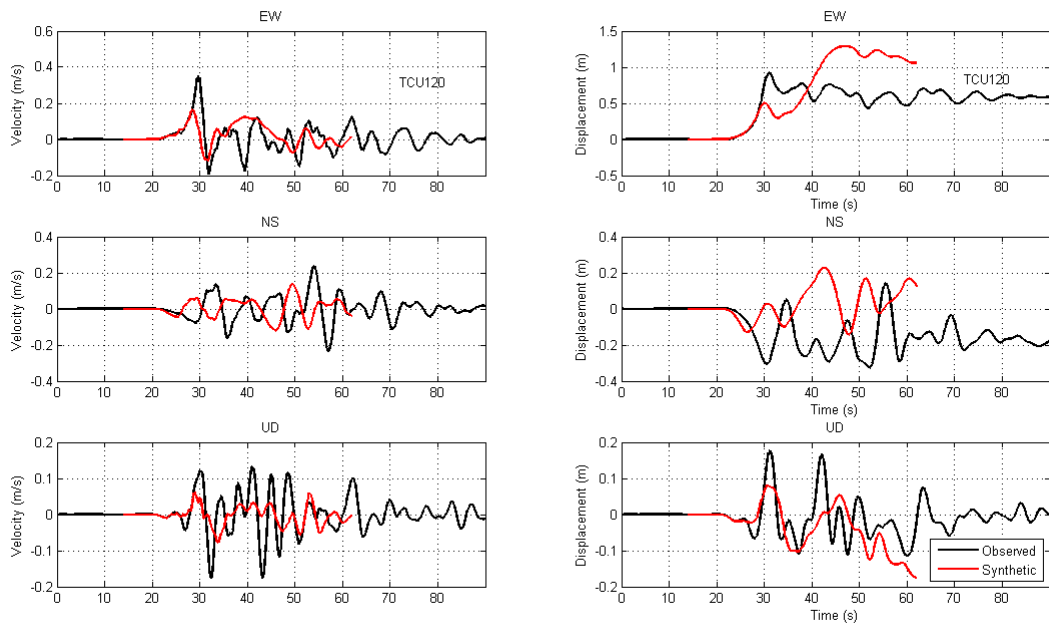


Figure A.28. Station TCU120

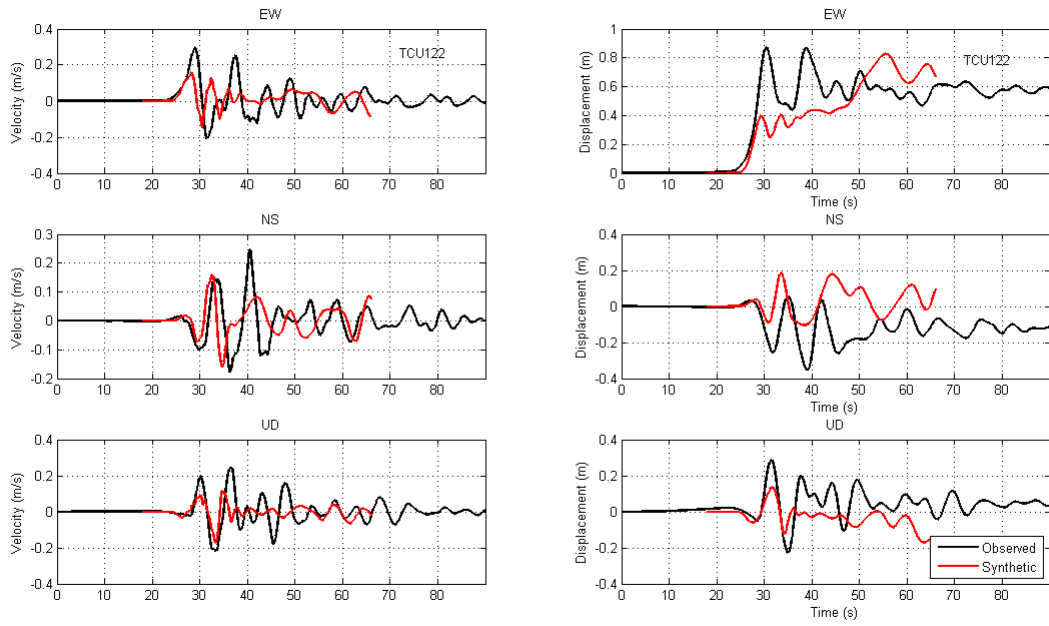


Figure A.29. Station TCU122

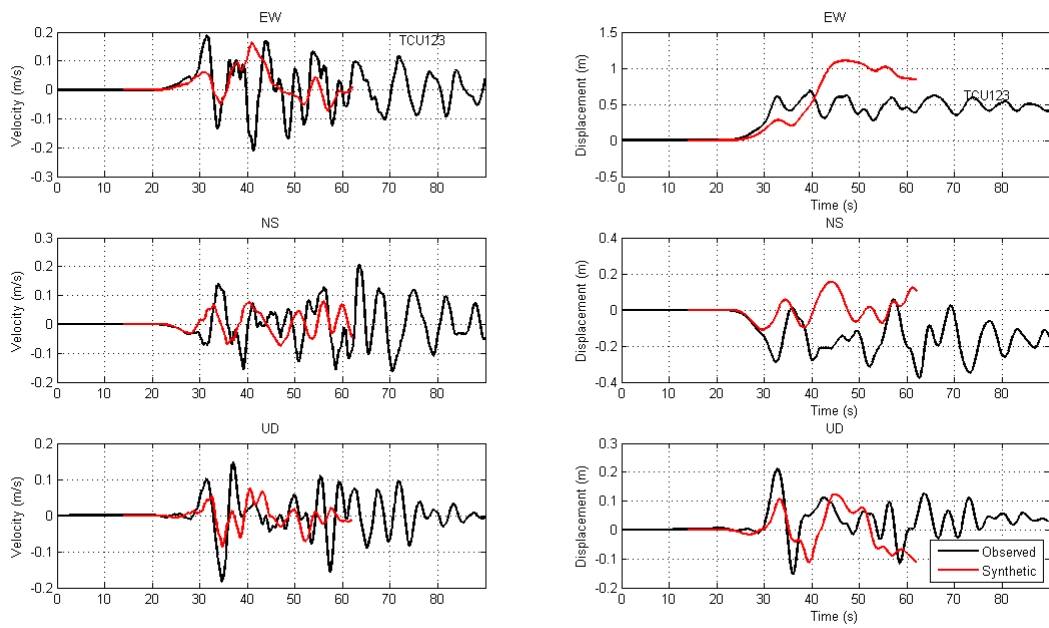


Figure A.30. Station TCU123

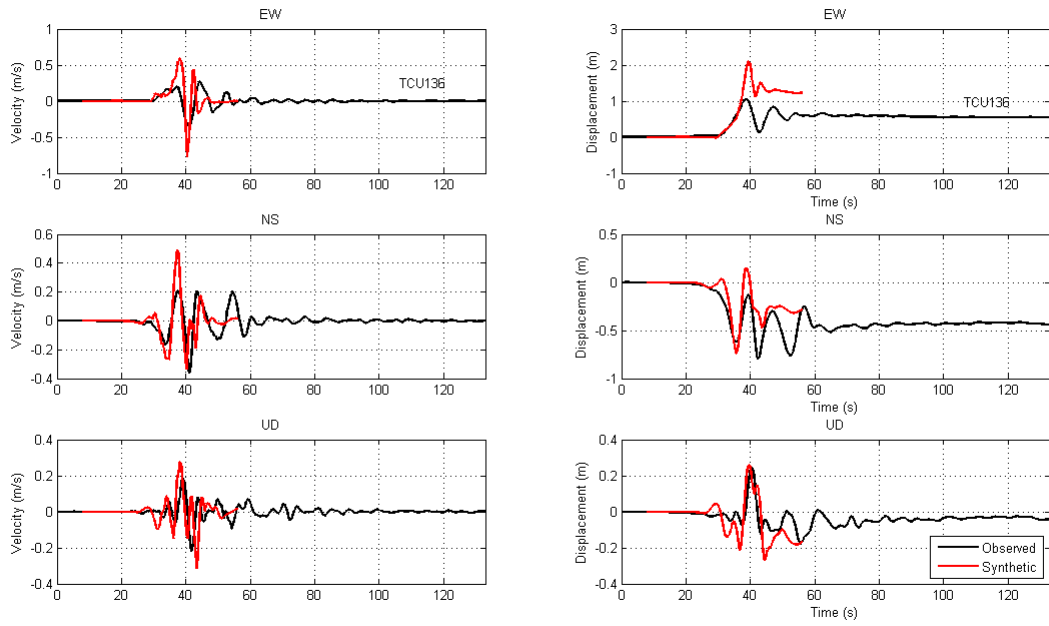


Figure A.31. Station TCU136

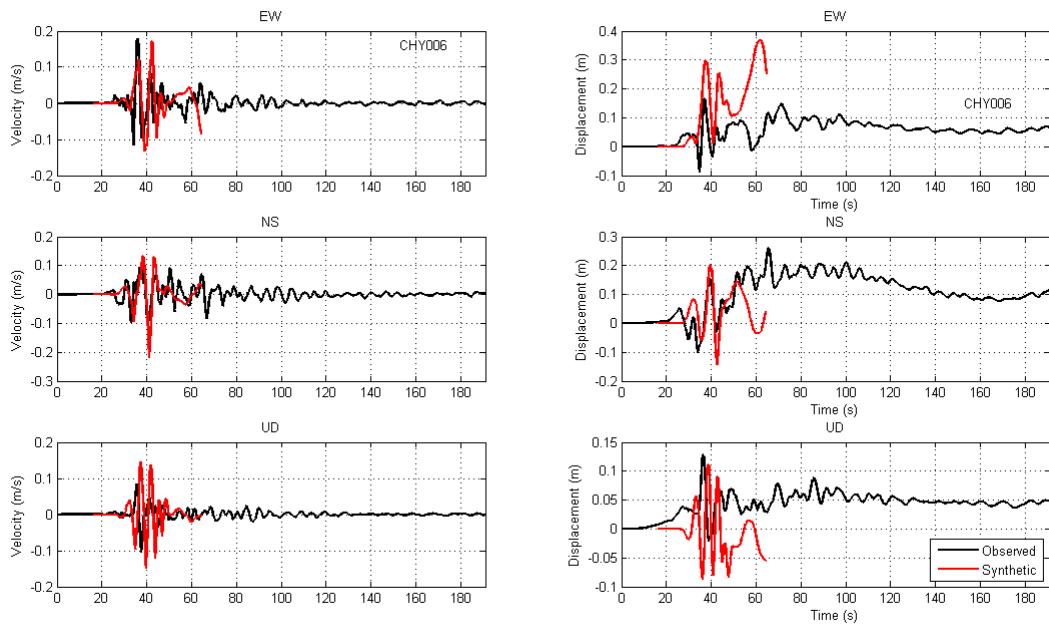


Figure A.32. Station CHY006

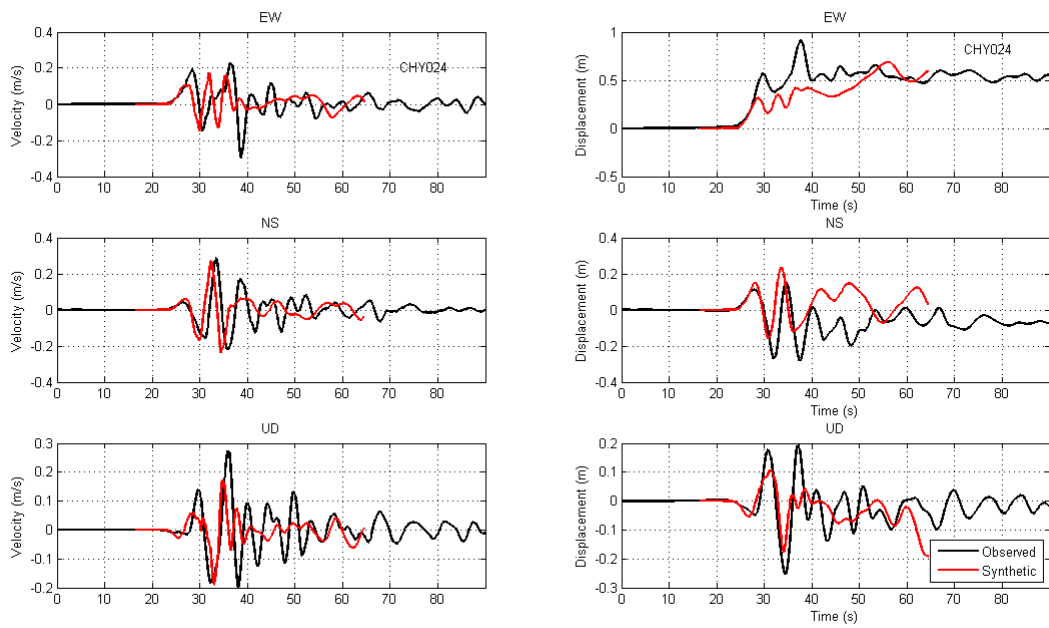


Figure A.33. Station CHY024

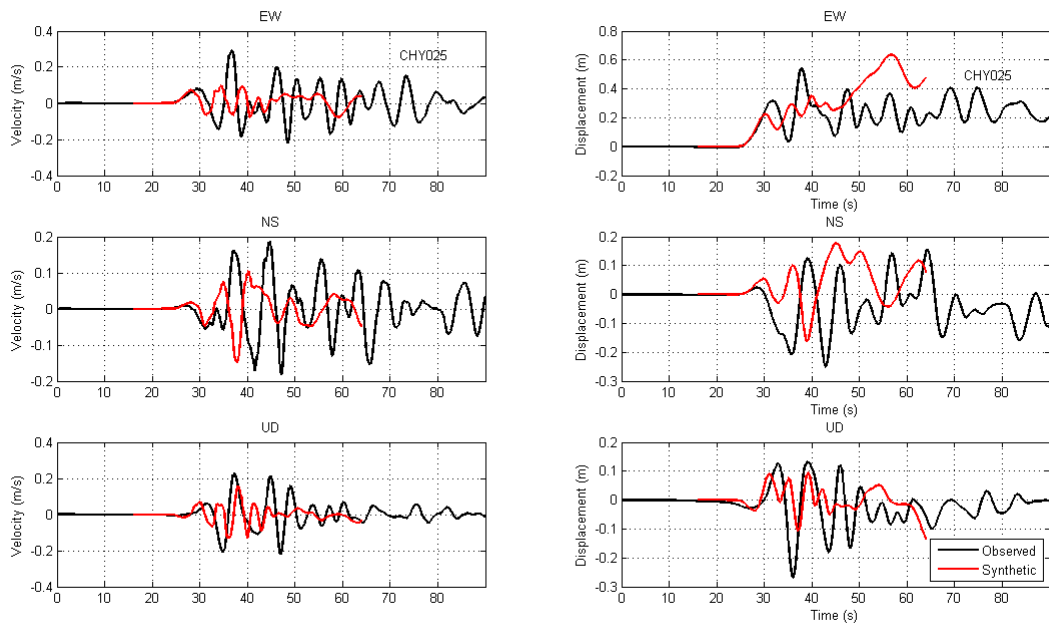


Figure A.34. Station CHY025

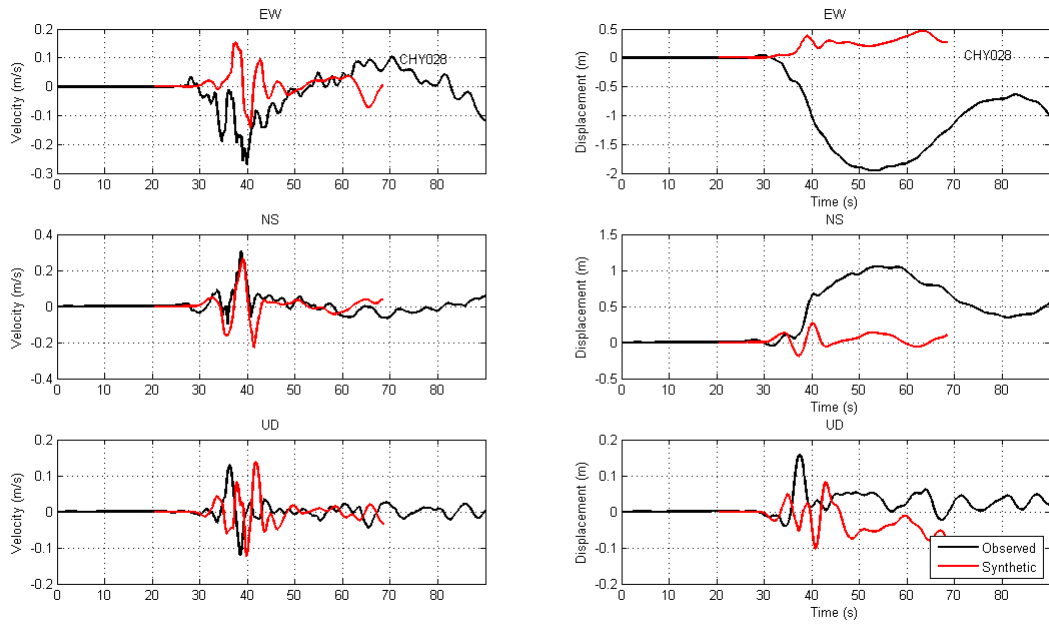


Figure A.35. Station CHY 028

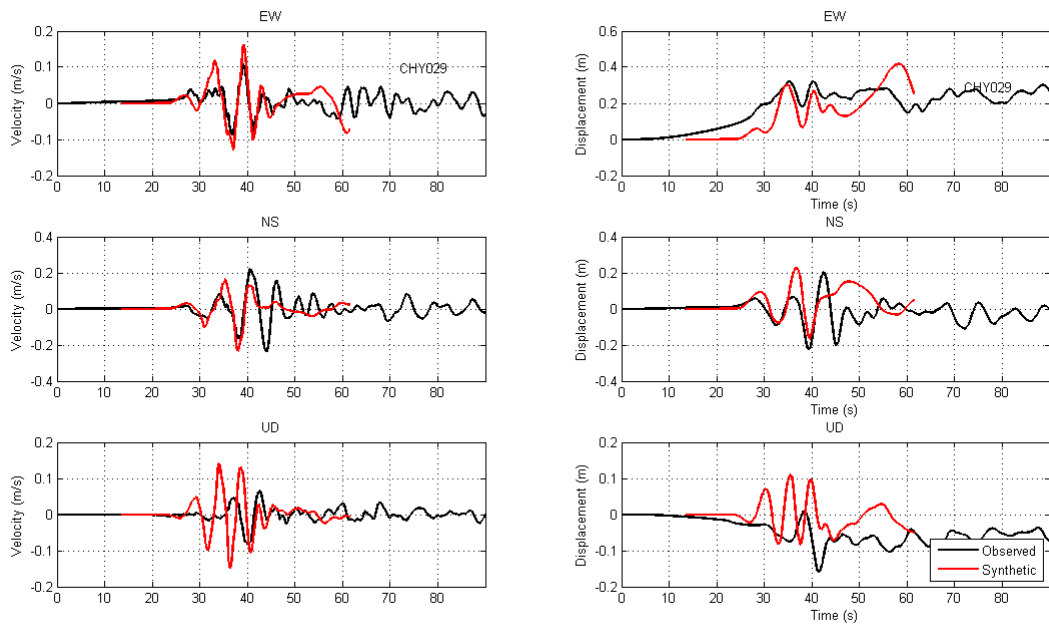


Figure A.36. Station CHY029

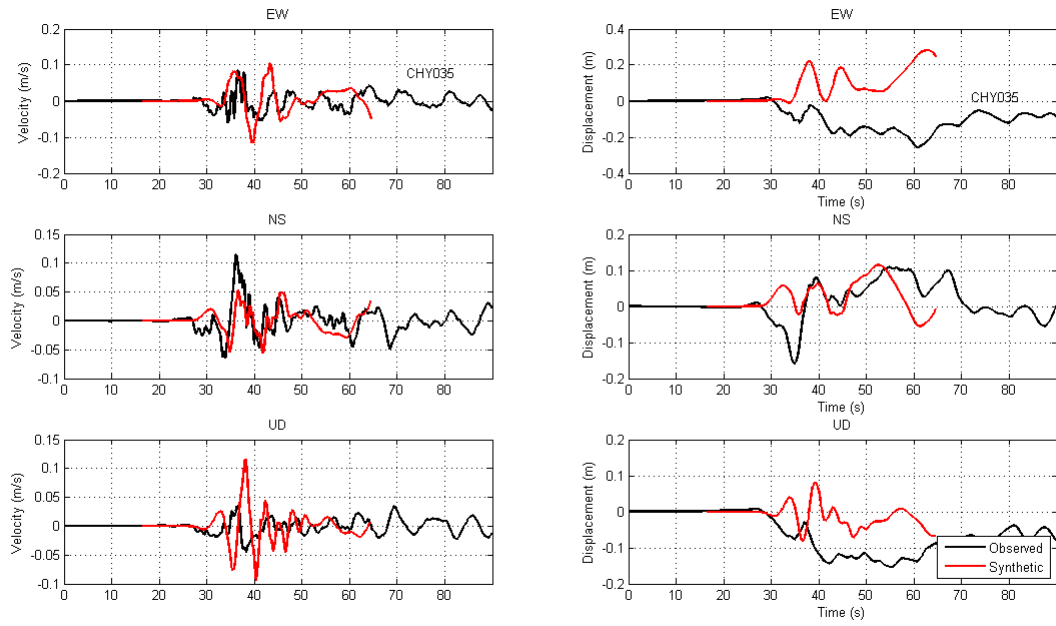


Figure A.37. Station CHY035

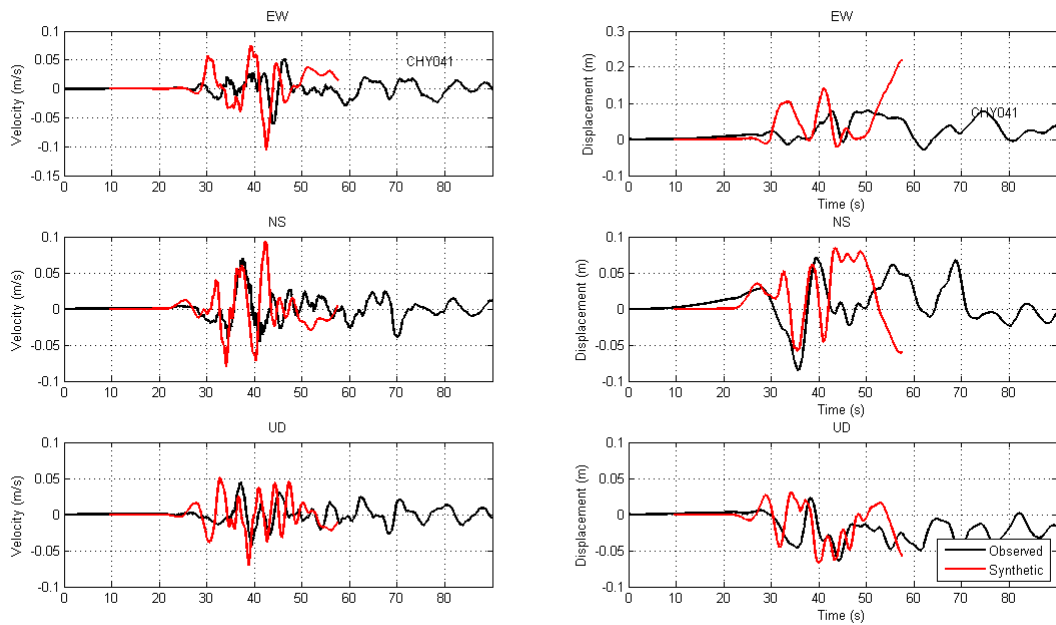


Figure A.38. Station CHY041

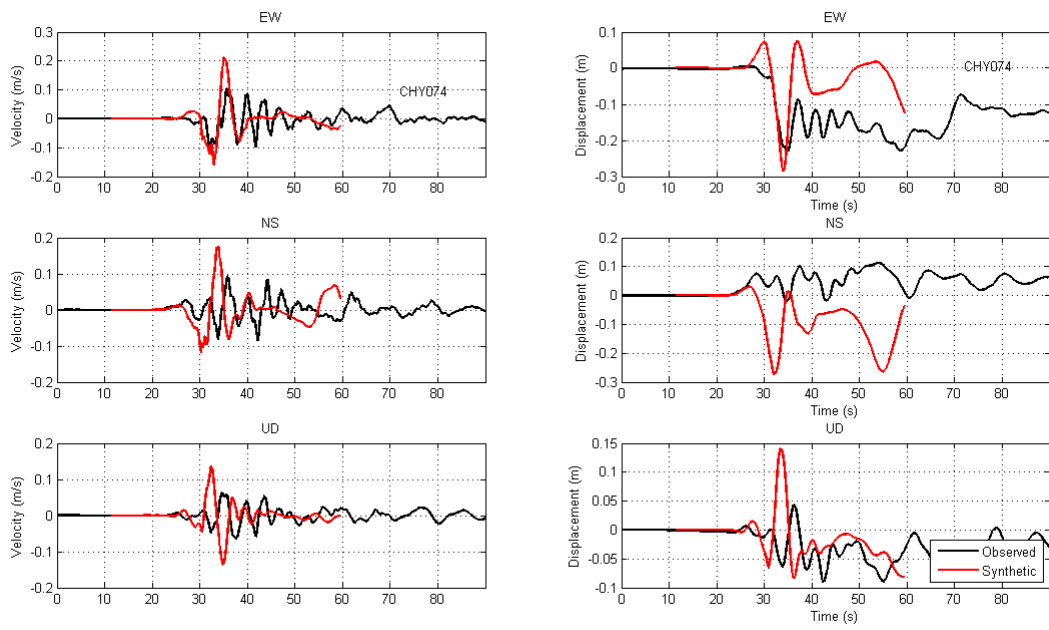


Figure A.39. Station CHY074

Appendix-2

ハザード試算レポート

Report: New Relations and Logic Tree for Probabilistic Fault Displacement Hazard of Strike-Slip Earthquakes in Japan

Introduction

In this report, we present a new framework for Probabilistic Fault Displacement Hazard Analysis geared towards fault hazard studies on strike-slip faults in Japan. In order to develop this framework, we analyzed a new dataset of surface slip provided by JNES. This dataset was evaluated relative to two models for fault rupture hazard, Petersen et al., 2011, who presented a framework for crustal strike-slip earthquakes and Takao et al., 2013, who developed a method for Japan for any crustal earthquake. The latter model uses the form used in Youngs et al (2003) which use beta and gamma distributions to describe the statistical properties of the relationship between along strike position and slip.

Methodology

General form of the PFDHA equation

In general, the equation for the exceedance rate for displacement at a site ($k(d>D)$) on a fault has the following form:

$$k(D \geq d) = \sum_{m_j=m_0}^{m_u} \dot{N}(m_j) \times \left[\sum_{k=1}^N \Pr(D \geq d | r_k, m_j) \times \Pr(sr \neq 0 | m_j) \times \Pr(r_k | m_j) \right]$$

where :

- $\dot{N}(m_j)$ is the mean number of earthquakes of magnitude m_j

- $\Pr(D > d | r_k, m_j)$ is the probability that displacement D exceeds d given that an earthquake of magnitude m_j centered at a distance r_k occurs.
- $\Pr(sr \neq 0 | m_j)$ the probability of surface rupture given magnitude m .
- $\Pr(r_k | m_j)$ is the probability that an earthquake of magnitude m_j occurs with its center of rupture located at r_k .
- m_0 is the minimum magnitude of earthquake engineering significance, and
- m_j is the maximum magnitude for earthquake event considered.

The main differences between the Petersen et al. (2011) papers and Takao et al. (2013) are in the forms of terms 2 and 3. The latter uses the beta and gamma distribution functions whereas Petersen et al. use (log) normal distributions. For the Petersen et al. (2011) we show the functional form of these two terms in the following two sections.

Slip distribution function

Petersen et al. (2011) have derived several (six in all) functions (Figure 1) for slip along a rupture in the case of strike-slip faulting. They express the average slip at a location as a function of magnitude and the site location relative to the ends of the rupture, and carried out a regression using a log-normal distribution).

The displacement for a rupture is not uniform over the entire rupture, but instead tapers towards both ends of the rupture, and is parameterized using the ratio l/L between the total rupture length (L) and the distance from the center of the rupture to the point on the rupture closest to the site (Figure 1). For this function, a log-normal distribution is assumed and Petersen et al (2011) have determined several alternative functional forms, bilinear, quadratic or elliptic. Furthermore, they derived expressions both for displacement as a function of magnitude, and one for normalized displacement, for a total of six possible equations.

The bi-linear relation has the form:

$$\ln(D) = 1.7969m + 8.5206 l/L - 10.2855$$

for $l/L < (l/L)'$ and

$$\ln(D) = 1.7658m - 7.8962$$

for $l/L \geq (l/L)'$, where $(l/L)'$ is the ratio for which the two equations are equal.

The standard deviation, sigma, is 0.9624.

The quadratic and elliptic forms are given as:

$$\ln(D) = 1.7895m + 14.4696 l/L - 20.1723 (l/L)^2 - 10.54512$$

and

$$\ln(D) = 3.3041 \sqrt{1 - 4(l/L - 0.5)^2} + 1.7927m - 11.2192$$

with sigma's of 1.1346 and 1.1348 respectively.

In the normalized equations, we also assume a slip distribution that is tapered at the end but is relative to the average slip (D_{ave}) given by the Wells and Coppersmith (1994) relations for strike-slip earthquakes. Petersen et al. (2011) expressed this term from a regression normalized on the average displacement as:

$$\ln(D) = \ln(D_{ave}) + 8.2525 l/L - 2.3010$$

for $l/L < 0.3008$, with a sigma of 1.2962, otherwise

$$\ln(D) = \ln(D_{ave}) + 0.1816$$

and a sigma of 1.0013 for the bi-linear form,.

The quadratic and elliptic equations are

$$\ln(D) = \ln(D_{ave}) + 14.2824 l/L - 19.8833 (l/L)^2 - 2.6279$$

and

$$\ln(D) = \ln(D_{ave}) + 3.2699\sqrt{1 - 4\left(\frac{l}{L} - 0.5\right)^2} - 3.2749$$

respectively with sigma's of 1.1419 for both cases.

Takao et al's (2013) relations are given in the form of cumulative distribution functions with the form:

$$F(y) = \frac{1}{\Gamma(a)} \int_0^{y/b} e^{-t} t^{a-1} dt \quad \text{where:}$$

$$a = e^{(0.7+0.34\frac{l}{L})}, b = e^{(-1.4+1.82\frac{l}{L})}, y = D/AD$$

for scaling of slip (D) with respect to average displacement (AD), and:

$$F(y) = \frac{\Gamma(a+b)}{\Gamma(a)\Gamma(b)} \int_0^y (1-t)^{b-1} t^{a-1} dt \quad \text{where:}$$

$$a = e^{(0.7-0.87\frac{l}{L})}, b = e^{(-2.3-3.84\frac{l}{L})}, y = D/MD$$

for scaling of slip with maximum displacement (MD).

The mean value for these relations is $a.b$, which implies a linear relationship between $\ln(D/AD)$ and l/L .

In Figure 1 we show the differences between the Petersen and Takao models, and it is clear that there is a significant difference in shape of the curves between the various Petersen curves on the one hand and the Takao curves on the other.

Probability of surface rupture

$\Pr(sr \neq 0|m_j)$ is the probability that surface rupture (sr) occurs for a given magnitude, given) as:

$$\Pr(sr \neq 0 | m_j) = \frac{e^{a+bm}}{1 + e^{a+bm}}$$

with $a = -12.51$ and $b = 2.053$ for a strike-slip earthquake (Petersen et al., 2011), and $a = -32.03$ and $b = 4.90$ for the Japanese data (Takao et al., 2013). Thus, the probability of surface rupture for a thrust earthquake at magnitude 7.0 is only 0.48, compared to 0.86 for a strike slip event (Figure 2). Some authors have divided this function in two, one for the probability of surface rupture for the entire earthquake, and one for the probability of surface rupture reaching the site. The latter is sometimes inherently included in the previous term (slip distribution) and the integration process where we integrate over a range of rupture locations.

Comparison

The Takao et al. (2013) model combines data from Japan for all types of crustal earthquakes, which is in contrast to the Petersen et al. (2011) study. Although this gives a much larger database, this may not be ideal since the surface deformation from a strike-slip earthquake is different in character from a thrust event.

Analysis of the JNES data

In Figure 3 we show the cumulative dataset provided by JNES for this project. We also plotted the mean, median, 5, 15, 85 and 95% fractiles using bins of .05 (l/L). As a comparison, in Figure 4 we present the data used by Petersen et al. (2011). Although both data sets are for crustal strike-slip earthquakes, it is clear that they are systematically different, in that the Japanese data shows a much weaker attenuation towards the end of the fault compared to the Petersen model. Since the Takao et al. study was also based on the Japanese data, this explains why the Takao et al. model shows a simple gently sloping relationship whereas the Petersen functions tend to be flat down to $x/L = 0.3$ and then drop off more steeply. This suggests that there is a systematic difference between the rupture behavior of Japanese

earthquakes and (primarily) US earthquakes. However, if we plot the data for the Kobe earthquake (Figure 5), which is common to both studies, we find the same differences. It should be noted that the JNES set contains much more data than the Petersen one, so the difference may be related to that, but it may be advisable to review the procedures used to obtain both datasets.

Relationship based on JNES data

Given the systematic differences between the JNES and Petersen data, we decided to concentrate on deriving a relationship based solely on the JNES data for Japan and one including both sets. We chose the gamma and beta distributions similar to Takao et al. (2013), but explored both the linear and a quadratic form for the relation between $\ln(D/AD)$ since even the Japanese data suggests a relatively flat curve for $l/L > .3$. We carried out the fitting by first determining the mean of the function and subsequently finding the set of parameters a and b (constrained by the mean $a \times b$ or $a/(a+b)$ respectively) that gives a satisfactory fit to the 5, 15, 85 and 95 percentile curves. The final results are shown in Figure 6 (and compared to the Petersen data in Figure 7), where we present results of the quadratic fit. The parameters are

$$a = \exp\left(0.5 + 2.23 \frac{l}{L} - 4.71 \left(\frac{l}{L}\right)^2\right)$$

$$b = \exp\left(-1.15 + 1.6 \frac{l}{L} - 0.15 \left(\frac{l}{L}\right)^2\right)$$

for the average displacement scaling and

$$a = \exp\left(0.7 - 0.81 \frac{l}{L} - 1.25 \left(\frac{l}{L}\right)^2\right)$$

$$b = \exp\left(2.1 - 3.84 \frac{l}{L} - 1.0 \left(\frac{l}{L}\right)^2\right)$$

for the maximum displacement scaling. The final forms and fractiles are shown in Figure 8 and again we present the comparison with the Petersen data in Figure 9. It is clear that the new JNES relations do not give a satisfactory fit to the Petersen data, which is expected from the previous discussion. For off-fault displacements, the data made available by JNES is limited in scope and we therefore compared the data to the existing relations from Petersen et al. (2011) (Figures 10) and found that they are in broad agreement. We therefore used the distributed model from Petersen et al. for all models.

Logic tree

Given the difference in slip data between the Japanese and US relations, it is desirable to give a larger weight to the relations that are specific to Japan. On the other, given the systematic differences between the strike-slip relations and thrust and normal faulting relations (Petersen et al., 2011; Youngs et al.; 2003, Moss and Ross, 2011), it may be prudent to down weight relations that are based on a mix of mechanisms, such as the Takao relations. When devising a logic tree for the PFDHA in Japan specifically for strike-slip earthquakes we therefore propose the following distribution:

| region | weight | model | weight | scaling | weight |
|-------------|--------|---------------|--------|---------|--------|
| Japanese | 2/3 | JNES (this) | 2/3 | AD | 1/2 |
| | | | | MD | 1/2 |
| | | Takao | 1/3 | AD | 1/2 |
| | | | | MD | 1/2 |
| US (Global) | 1/3 | Petersen (bi) | 1/3 | AD | 1/2 |
| | | | | Mag | 1/2 |
| | | Petersen (qu) | 1/3 | AD | 1/2 |
| | | | | Mag | 1/2 |
| | | Petersen (el) | 1/3 | AD | 1/2 |
| | | | | Mag | 1/2 |

Example for Awaji Island

We have computed a test case of the new logic tree and relations for the displacement field on and around the 1995 Kobe earthquake rupture on Awaji Island (Figure 11). In map view (Figure 12), one can clearly see the on-fault and off-fault displacement hazard. The displacement hazard curves are shown in Figure 13, where it is clear that there is a considerable spread between the JNES (and Takao) and the Petersen models. In general, the JNES and Takao relations give higher hazard than the Petersen ones. This is understandable given the fact that the Petersen relations attenuate rapidly towards the end of the fault whereas the Japanese relations (and data) do not.

References

- Coppersmith, K. J., & Youngs, R. R. (2000). Data needs for probabilistic fault displacement hazard analysis. *Journal of Geodynamics*, 29(3), 329–343.
- Moss, R. E. S., & Ross, Z. E. (2011). Probabilistic Fault Displacement Hazard Analysis for Reverse Faults. *Bulletin of the Seismological Society of America*, 101(4), 1542–1553. doi:10.1785/0120100248
- Petersen, M. D., Dawson, T. E., Chen, R., Cao, T., Wills, C. J., Schwartz, D. P., & Frankel, A. D. (2011). Fault Displacement Hazard for Strike-Slip Faults. *Bulletin of the Seismological Society of America*, 101(2), 805–825. doi:10.1785/0120100035
- Youngs, R. R., Arabasz, W. J., Anderson, R. E., Ramelli, A. R., Ake, J. P., Slemmons, D. B., et al. (2003). A methodology for probabilistic fault displacement hazard analysis (PFDHA). *Earthquake Spectra*, 19, 191.
- Takao, M., Tsuchiyama, J., Annaka, T., & Kurita, T. (2013). Application of Probabilistic Fault Displacement Hazard Analysis in Japan, *Journal of Japan Association for Earthquake Engineering*, 13 (1), 1–20.

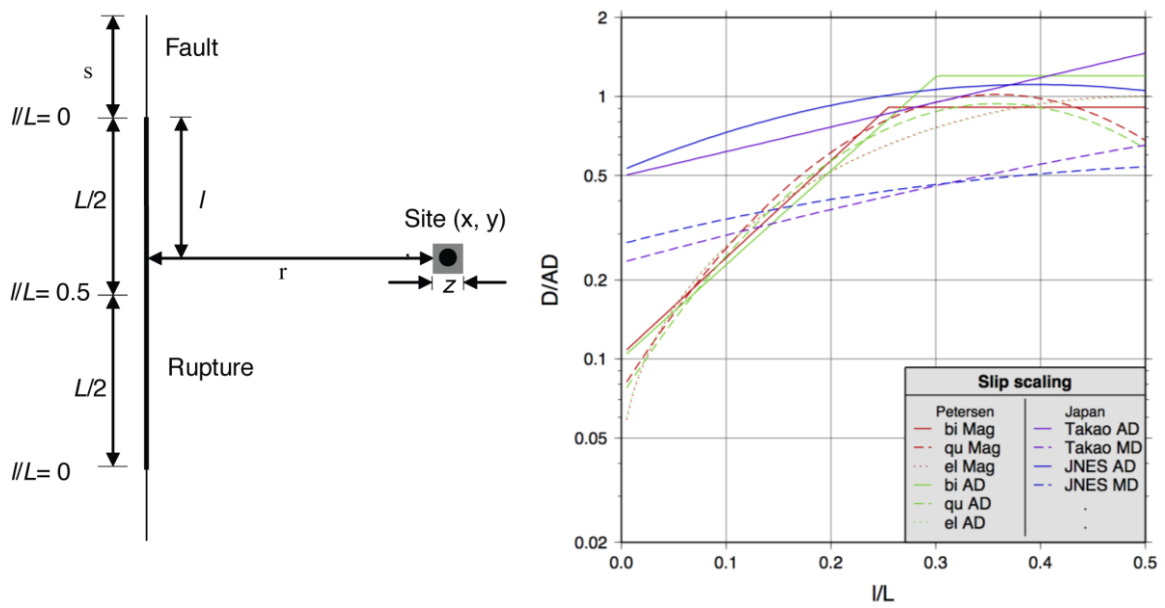


Figure 1 Slip distribution functions for a strike slip earthquake (Petersen et al., 2011) for a magnitude 7 earthquake. Shown on the left is the rupture and site geometry. On the right are the slip distributions.

Probability of Surface Rupture

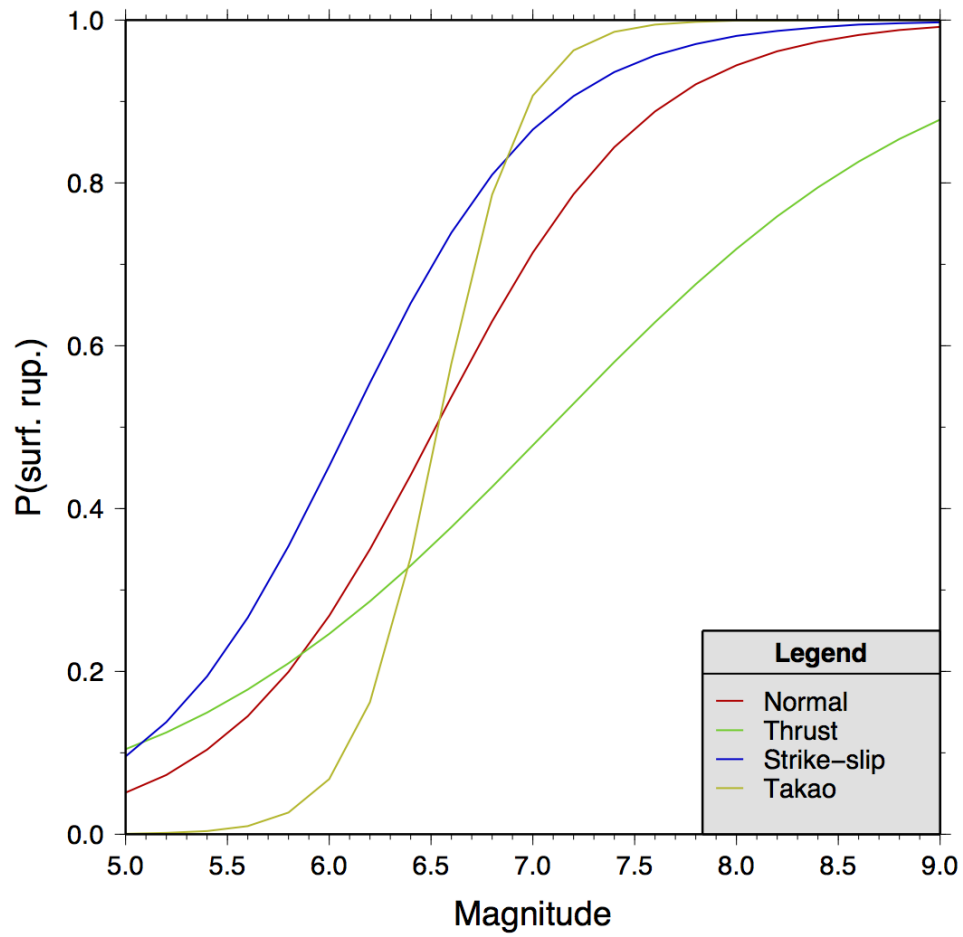


Figure 2 Probability of surface rupture for different types of earthquakes.

JNES-all

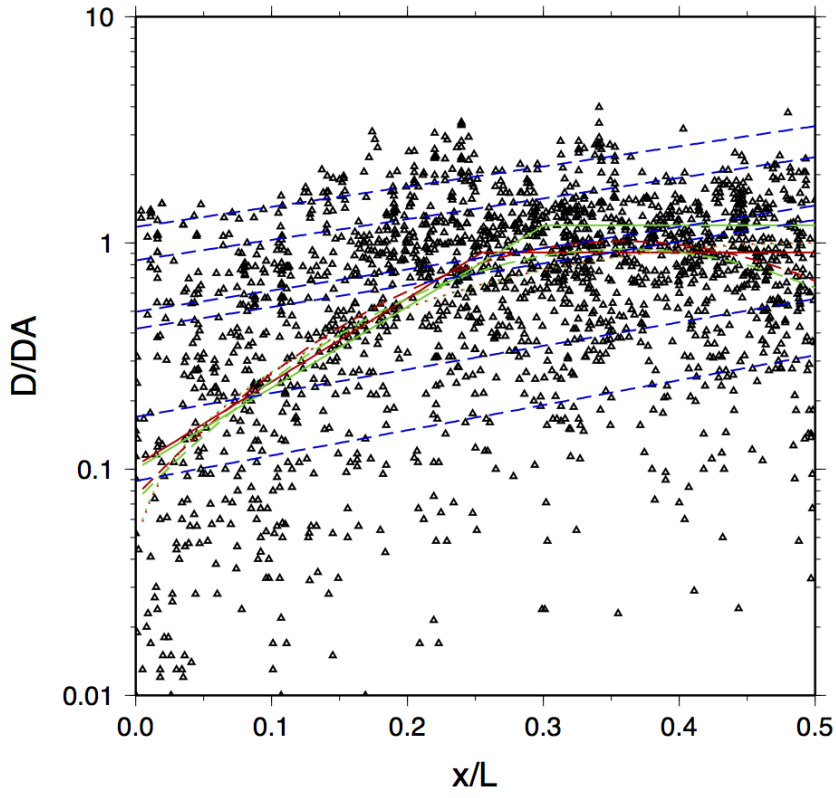


Figure 3. Comparison of all JNES data with the Takao relations and the Petersen relations.

Petersen

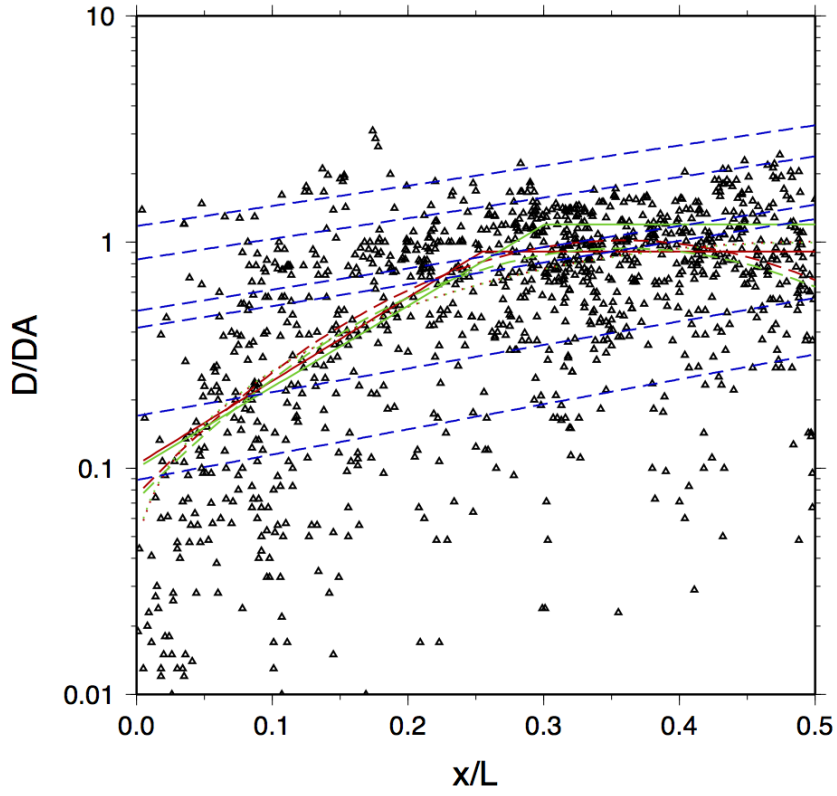


Figure 4. Petersen et al (2011) data shown with the Takao relation and the Petersen curves.

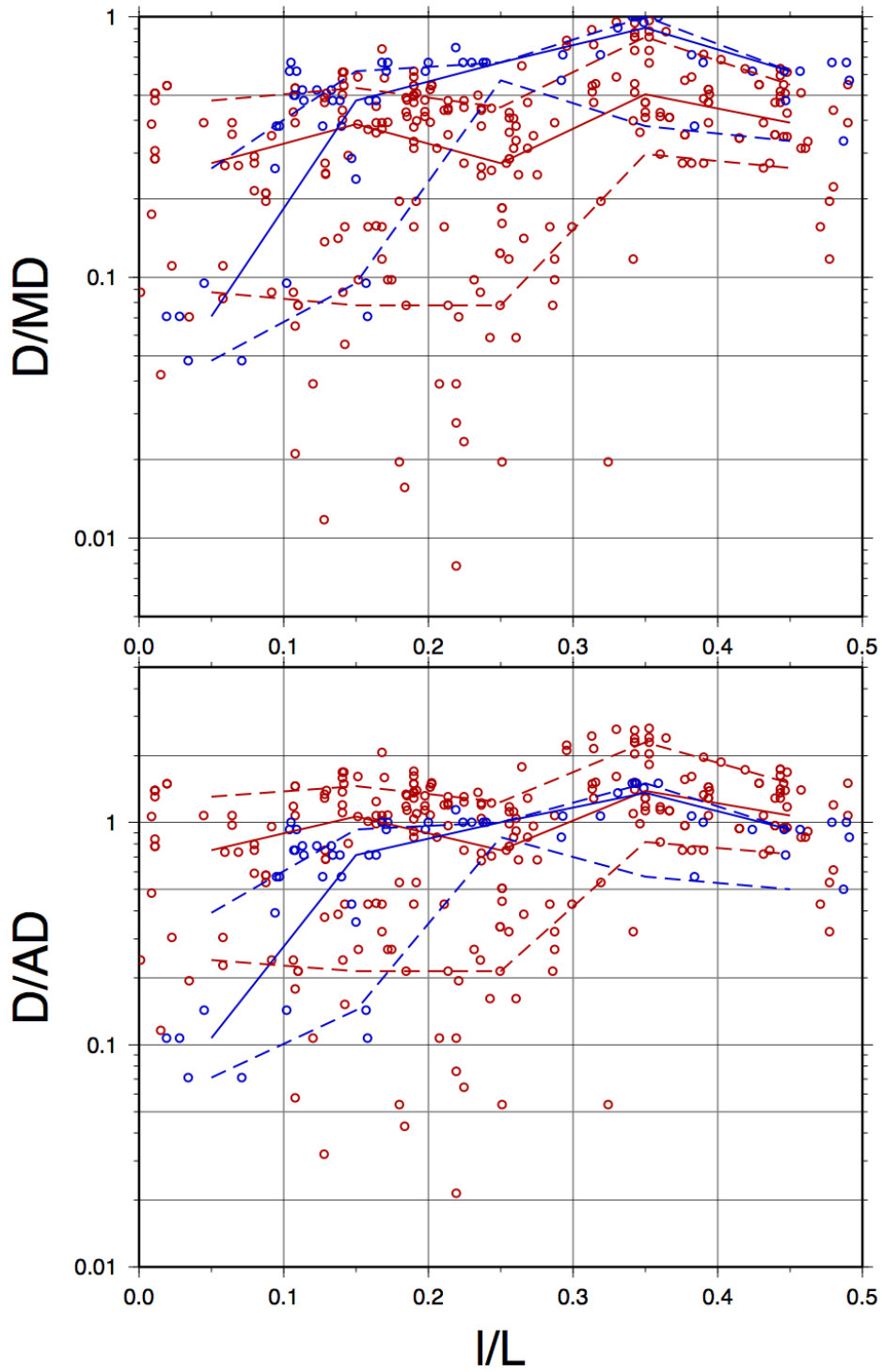


Figure 5. Comparison of the Kobe data from the Petersen catalog (blue circles and fractiles) and the JNES catalog (red circles and fractiles).

JNES

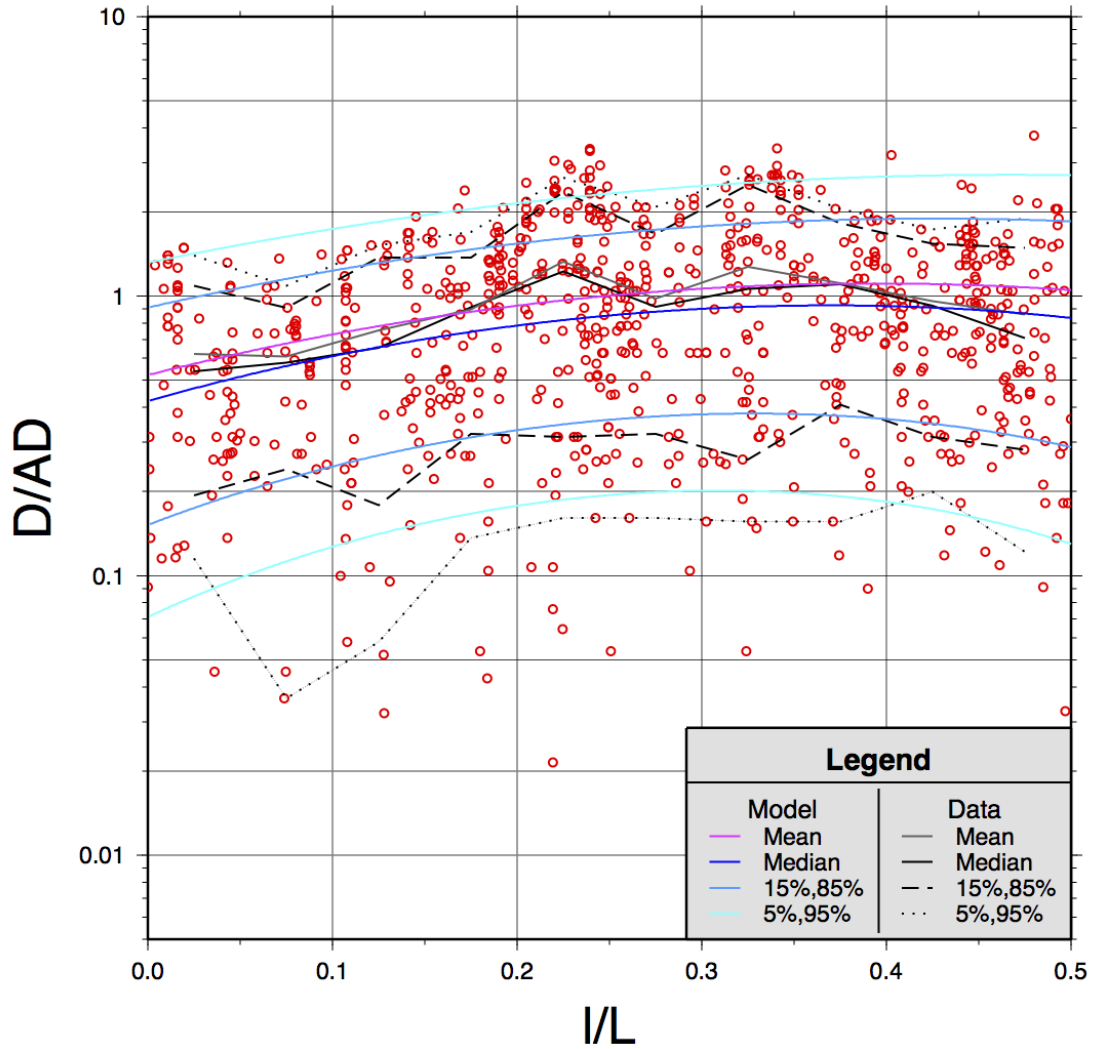


Figure 6. JNES data (red circles) with the fractile and mean estimates

Petersen

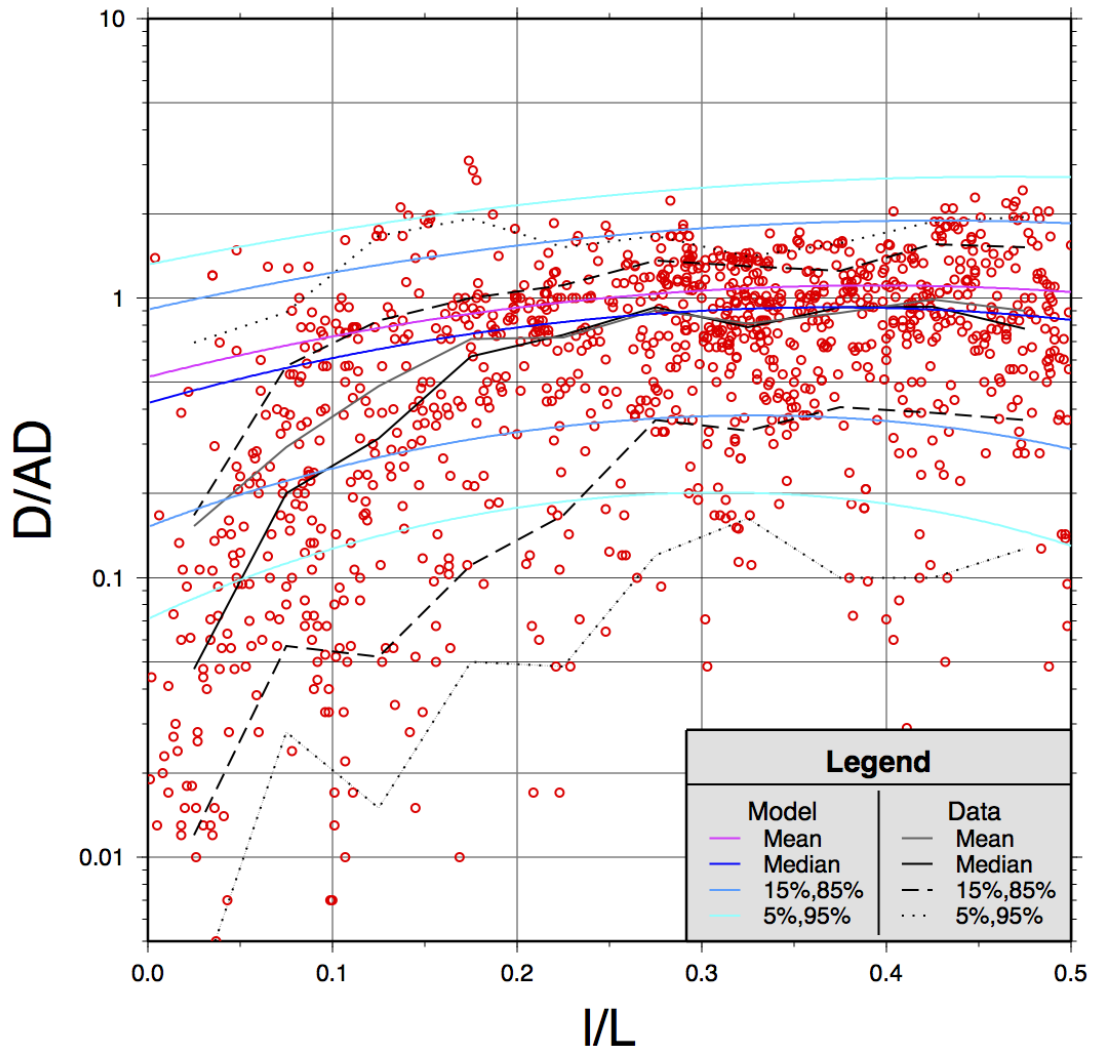


Figure 7. Petersen et al (2011) data for average displacement and data fractiles, overlain by the new JNES model curves.

JNES_MD

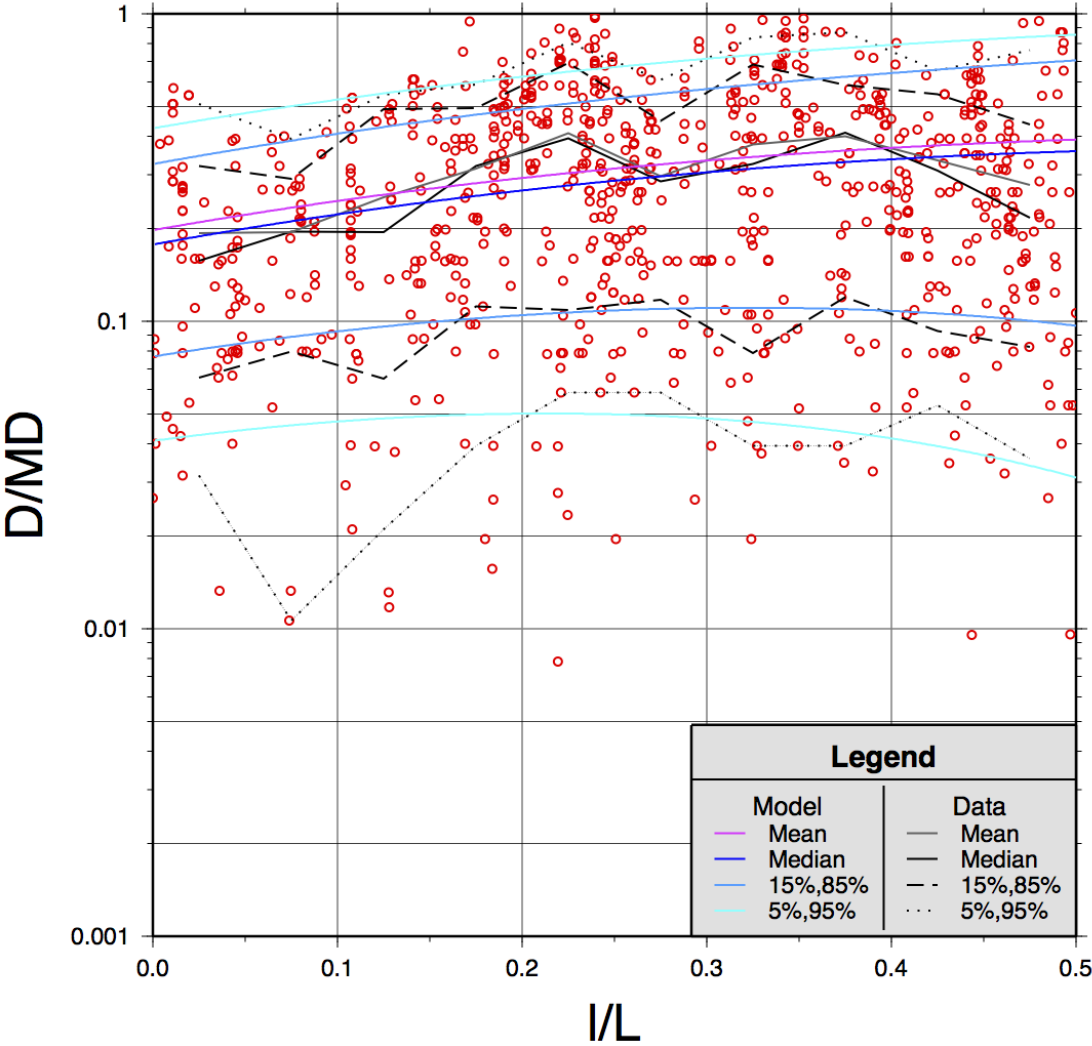


Figure 8. JNES data for maximum displacement scaling with the data fractiles and the new JNES mean, median and fractile curves.

Petersen_MD

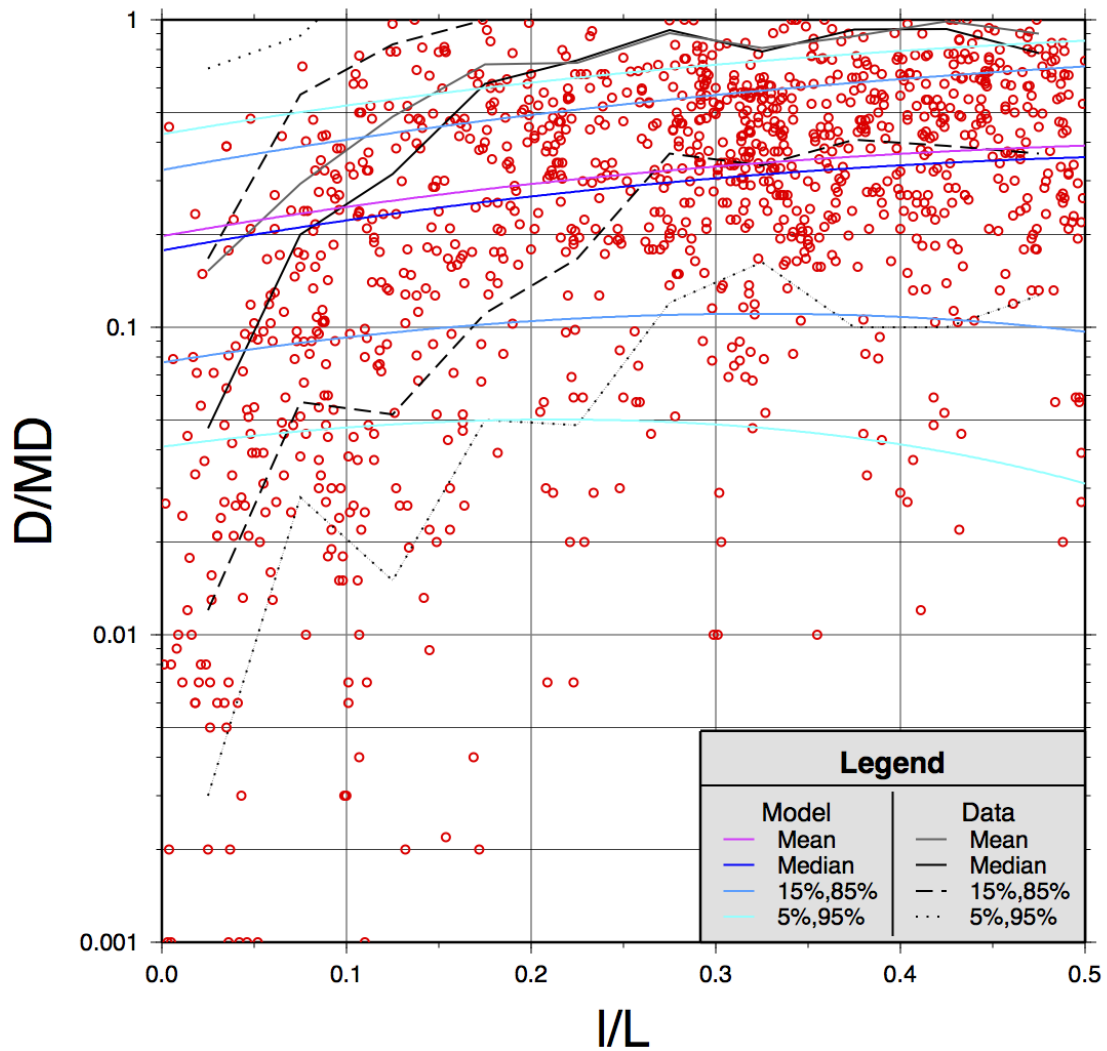


Figure 9. Petersen et al (2011) data and data fractiles, overlain with the new JNES model for D/MD.

Distributed faulting

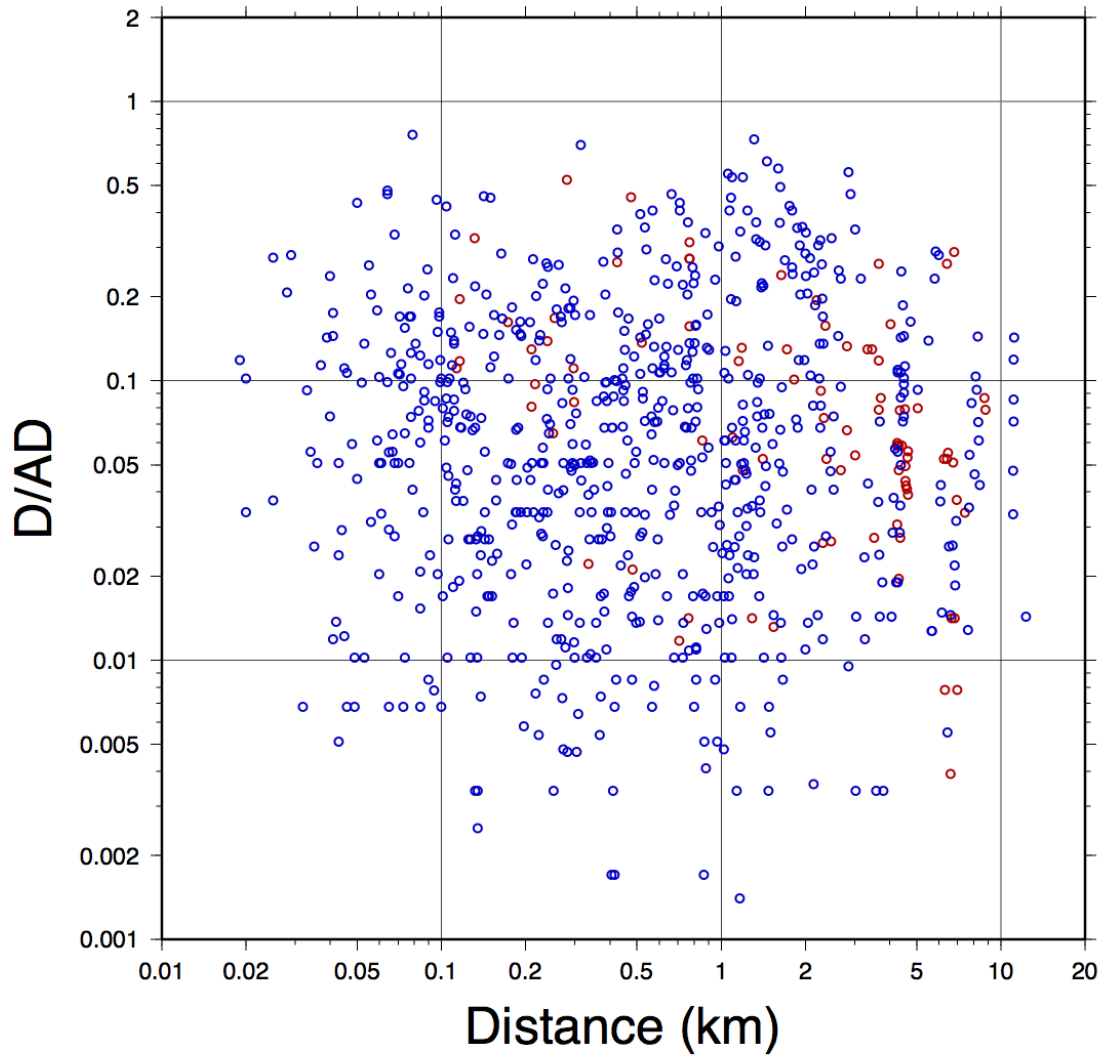


Figure 10. Data on distributed faulting from the Petersen et al. (2011) study and the JNES catalog.

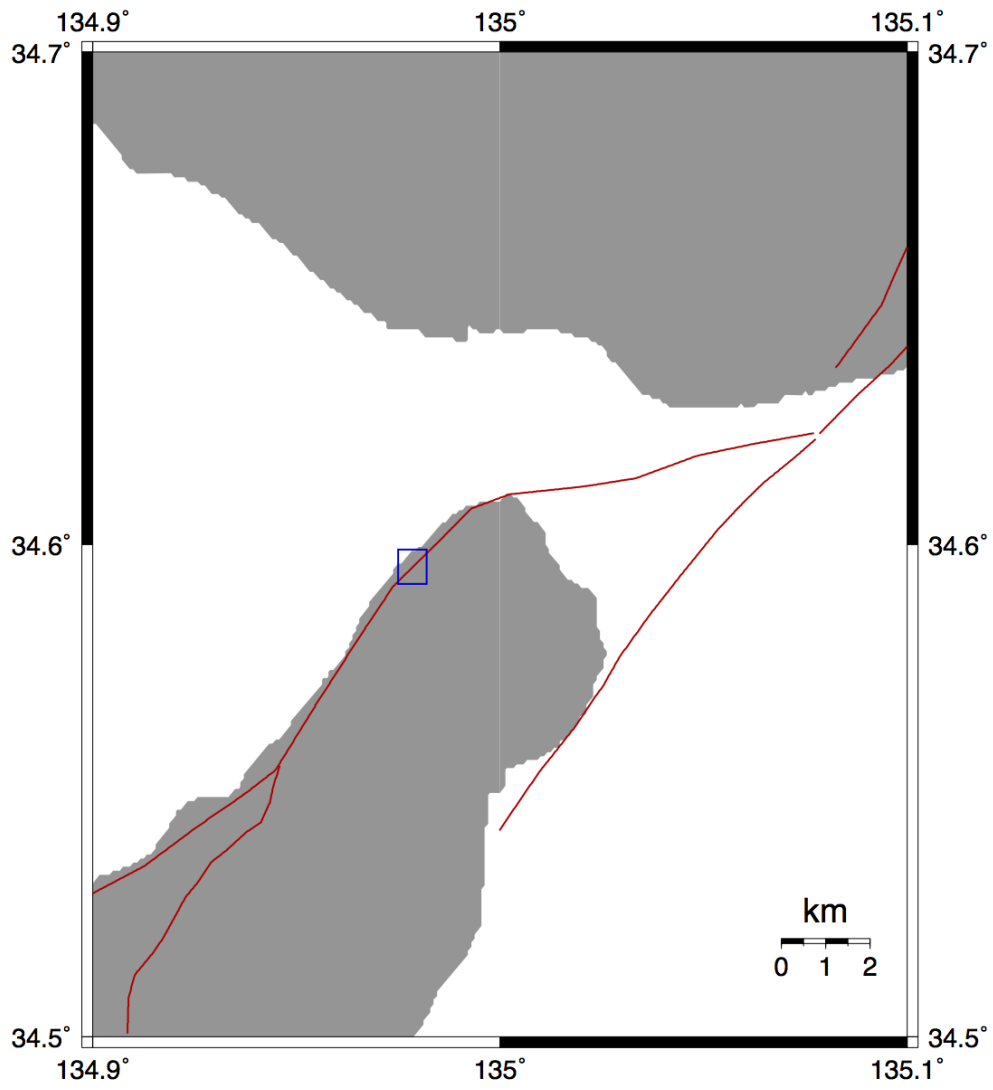


Figure 11. Map of northern Awaji Island with the test area indicated by the blue box.

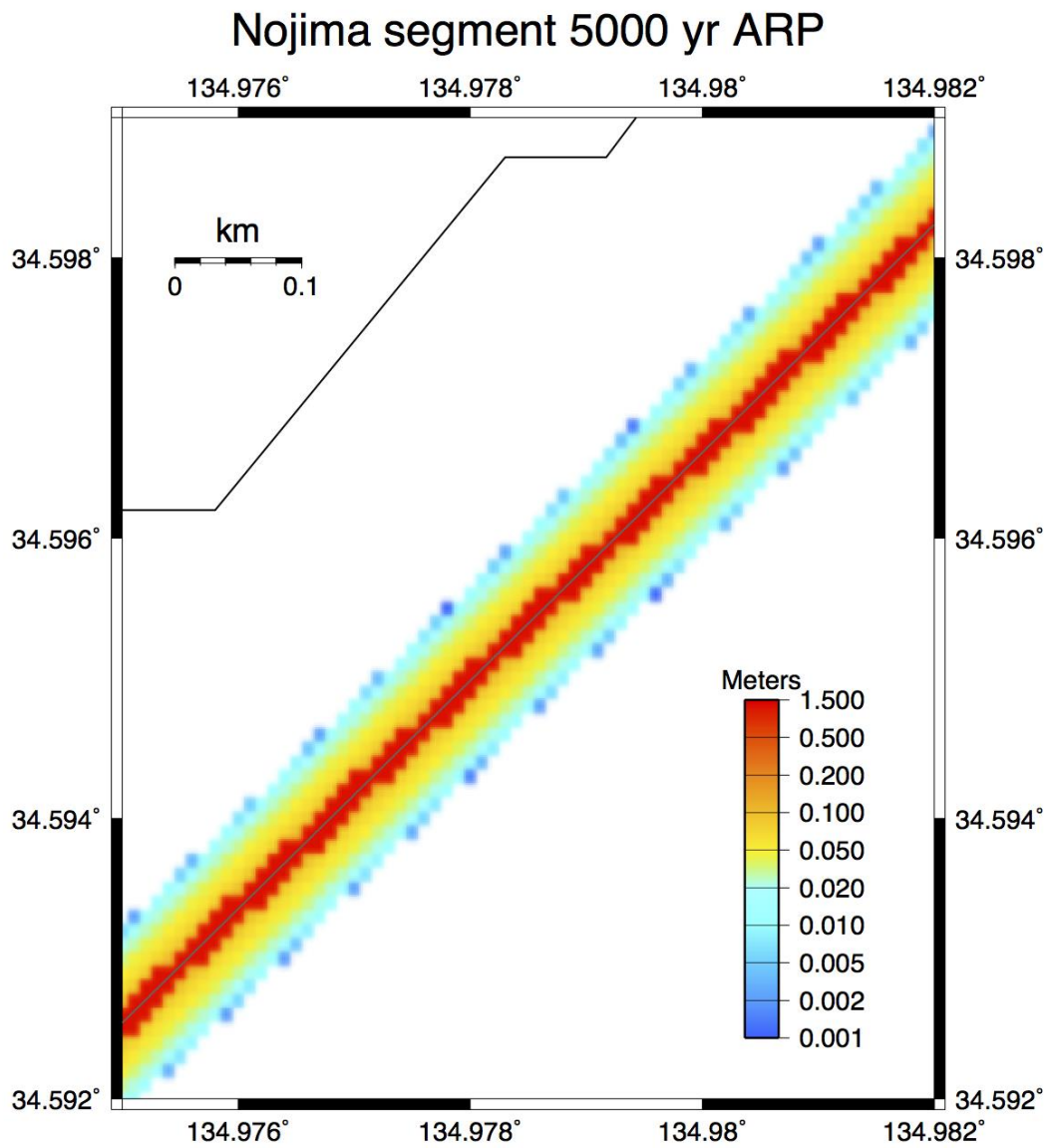


Figure 12. 5000 yr ARP (Average Return Period) displacement hazard map for our test area along the Nojima fault.

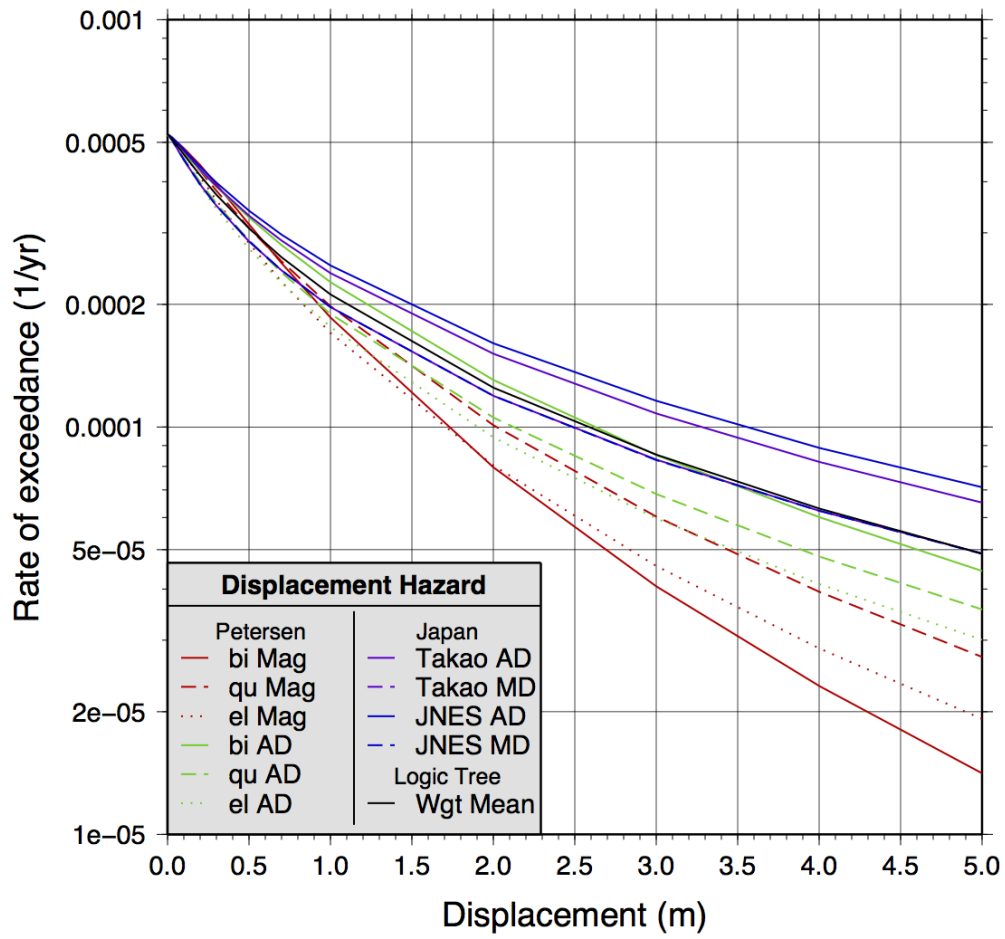


Figure 13. Hazard curves for different rupture models and weighted average, for a location on the fault.